

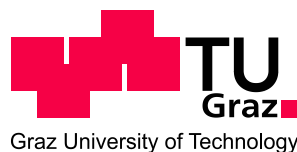
Dipl.-Ing. Stephan Georg Wolfgang Michelitsch, BSc

Electrical *in situ* measurements during electron beam induced platinum deposition

MASTER THESIS

For obtaining the academic degree
Diplom-Ingenieur

Master Programme of
Advanced Materials Science



Graz University of Technology

Supervisor:

Ao.Univ.-Prof. Dipl.-Ing. Dr.techn. Gerald Kothleitner

Co-Supervisor:

Dipl.-Ing. Dr.techn. Harald Plank

Institute for Electron Microscopy

Graz, December 2010

Deutsche Fassung:
Beschluss der Curricula-Kommission für Bachelor-, Master- und Diplomstudien vom 10.11.2008
Genehmigung des Senates am 1.12.2008

EIDESSTÄTTLICHE ERKLÄRUNG

Ich erkläre an Eides statt, dass ich die vorliegende Arbeit selbstständig verfasst, andere als die angegebenen Quellen/Hilfsmittel nicht benutzt, und die den benutzten Quellen wörtlich und inhaltlich entnommene Stellen als solche kenntlich gemacht habe.

Graz, am

.....
(Unterschrift)

Englische Fassung:

STATUTORY DECLARATION

I declare that I have authored this thesis independently, that I have not used other than the declared sources / resources, and that I have explicitly marked all material which has been quoted either literally or by content from the used sources.

.....
date

.....
(signature)

Abstract

Focused electron beam induced deposition from the gas phase is a novel technology for the fabrication of sub-10 nm nanostructures. The method enables the localized and maskless deposition of complex 3D structures with different functionalities such as insulating, conductive, or magnetic. Drawbacks, however, are low deposition rates and chemical impurities (mostly carbon) which can hinder the intended functionality. Hence, to make this method a more straightforward tool it is necessary to find countermeasures for both problems.

The aim of this master thesis was the design, the fabrication, and reliability testing of an active stage allowing for electrical characterization *during* electron beam induced deposition of Platinum in electron / ion dual beam microscopes. With such a tool, temporally resolved insights in the formation of platinum deposits are enabled, allowing for fast investigations of e.g. the influence of process parameters on the final performance.

After the successful hardware implementation, special software algorithms were applied to electrical raw data revealing the temporal behavior during growth. During the successful reliability testing an influence of active measurements could be ruled out making the tool an essential part for future *in situ* studies.

As a first result it was found that platinum deposits show sensor characteristics upon gas exposure. A closer look reveals a reversible variation of conductivity as a result of physisorption of gas molecules.

Key words: electron beam induced deposition, ion beam induced deposition, Platinum deposition, scanning electron microscope, focused ion beam

Kurzfassung

Induzierte Abscheidung aus der Gasphase mittels fokussierter Elektronenstrahlen ist eine neuartige Technologie für die Herstellung von sub-10 nm-Nanostrukturen. Das Verfahren ermöglicht die lokale und maskenlose Abscheidung von komplexen 3D-Strukturen unterschiedlicher Materialien (leitende, isolierende, magnetische, etc.). Nachteile dieser Methode sind geringen Abscheideraten und die chemische Verunreinigungen (meist Kohlenstoff), welche die beabsichtigte Funktionalität beeinflussen oder behindern. Um aus dieser Technologie eine praktikablere Methode für den wissenschaftlichen-technischen Bereich zu machen, ist es notwendig die Nachteile zu kompensieren oder passende Workarounds zu finden.

Ziel dieser Masterarbeit war die Entwicklung, Herstellung und Funktionsüberprüfung einer „aktiven“ Probenhalterung, welche die elektrische Charakterisierung während der elektroneninduzierten Abscheidung von Platin in Elektronen / Ionen / Zweistrahlmikroskopen ermöglicht. Mit einem derartigen instrumentellen Setup wird ein zeitlich aufgelöster Einblick in die Formierung von Platin Schichten möglich, welche eine schnelle Untersuchung, beispielsweise dem Einfluss der Prozessparameter erlaubt.

Nach der erfolgreichen Hardware-Implementierung wurden Software-Algorithmen entwickelt und getestet, um die elektrischen Rohdaten zu verarbeiten und für weitere Analysen passend aufzubereiten. Während umfangreicher Verlässlichkeitsuntersuchungen dieses „aktiven“ Setups konnte die Tauglichkeit verifiziert, sowie im Speziellen der Einfluss der elektrischen Messungen auf die Abscheidung ausgeschlossen werden. Dadurch wird dieses System zu einem wesentlichen Bestandteil für zukünftige *in situ* Studien im Bereich der elektronen / ionengestützten Abscheidung von elektrisch leitfähigen Schichten.

Ein erstes Resultat durch dieses System war die Beobachtung sensorischer Eigenschaften elektroneninduzierter Platinabscheidungen aufgrund von Gas-Wechselwirkungen. Genauere Untersuchungen zeigten eine reversible Veränderung der Leitfähigkeit infolge der Physisorption von Gasmolekülen erkannt.

Schlüsselwörter: elektronenstrahlinduzierte Abscheidung, ionenstrahlinduzierte Abscheidung, Platin Abscheidung, Rasterelektronenmikroskop, fokussierte Ionenstrahlen

Acknowledgments

My master thesis would not be accomplished without the following people, whom I would like to thank in the following lines:

Prof. Dipl.-Ing. Dr. Ferdinand Hofer, for allowing me to carry out the framework of the master thesis and giving me the chance to work in the field of electron microscopy.

Prof. Dipl.-Ing. Dr. Gerald Kothleitner, for supervising me with his valuable knowledge and advices.

Dipl.-Ing. Dr. Harald Plank, in particular, who supervised the scientific content of the entire thesis and always helped me with his bright ideas; motivated and guided me step by step through the whole master thesis.

Dipl.-Ing. Dr. Andreas Hohenau (group Jo Krenn, KFU), for fabricating excellent four-point structures.

Dr. Meltem Sezen for scientific support and fruitful discussions during my masters study.

My family, for supporting me through my entire life and being there whenever help was needed.

And finally, I would like to mention the entire FELMI-ZFE team, which helped me whenever needed and gave me the feeling of being a part of them. Especially Christian Gspan, Thomas Haber, Klemens Jantscher, Herbert Reingruber, Margit Wallner and Armin Zankel.

Table of Contents

Abstract	i
Kurzfassung	ii
Acknowledgments.....	iii
Table of Contents	iv
List of symbols and abbreviations	vi
Introduction	1
Motivation	2
Outline	3
1 Fundamentals	4
1.1 SEM and Focused Ion Beam	4
1.1.1 SEM electron optics	6
1.1.2 Signal detection and imaging of electrons	12
1.1.3 Ion Beam Optics	15
1.1.4 Signal detection and imaging of ions	17
1.2 Deposition	20
1.2.1 The Precursor	22
1.2.2 Precursor Adsorption and Diffusion	24
1.2.3 Deposition basics and growth characteristics.....	26
1.2.4 Advanced patterning (EBID max smooth).....	27
2 Chapter 1: Characterization of EBID Max Smooth Growth Characteristics	28
2.1 Experimental	28
2.1.1 Substrate	28
2.1.2 Deposition	28
2.1.3 Analysis via FIB/SEM	30
2.1.4 Data acquisition.....	33
2.2 Results and discussion.....	34
2.2.1 Influence of the patterning position	34
2.2.2 Investigation of the temporal height evolution via AFM.....	38
2.2.3 Dependence on the geometric footprint	40
2.2.4 Dependency on refresh times	41
2.3 Conclusion.....	43
3 Technical preparations	45
3.1 Four point resistor measurement	45
3.2 Four point structure	46
3.2.1 Layout design and Resistor deposition method.....	47
3.2.2 First prototype (glass sample)	48
3.2.3 Second prototype (two point structure)	50
3.2.4 Final specimen.....	51
3.3 Current source	53
3.3.1 Fundamental considerations	53
3.4 Electrical circuit design	54
3.5 Specimen holder	56

3.6	Pre testing	57
3.7	Data acquisition	59
3.7.1	LabVIEW program code	59
3.7.2	Timing problem	60
3.7.3	Filter and data	61
4	Chapter 2: Feasibility studies and first results	64
4.1	Measuring methods	64
4.2	Data convolution	67
4.3	First <i>in situ</i> measurements	67
4.3.1	Applying a voltage	68
4.3.2	The first resistor (R1_U0)	68
4.3.3	Electrical charging (chopper, resistor R1_U2)	70
4.3.4	High time resolution	73
4.4	First real four point measurement (P8_R3_R3_U1)	74
4.5	Dependence on the current flux during deposition	77
4.6	Influence of water vapor on the electrical performance	78
4.7	Resistance variation due to ambient exposure (chamber venting)	82
4.8	Influence of electrical <i>in situ</i> characterization on the resistor measurements during gas exposure	85
4.9	Electrostatic discharge	87
5	Summary	88
6	Outlook	90
7	References	91

List of symbols and abbreviations

°C	Degree Celsius
µm	Micrometer
ADC	Analog Digital Converter
AE	Auger Electron
AFM	Atomic Force Microscopy
BSE	Backscattered Electron
EBID	Electron Beam Induced Deposition
EDX	Energy Dispersive X-Ray Spectroscopy
eV	Electron Volt
ESD	Electrostatic Discharge
ETD	Everhart Thornley Detector
FELMI	Institute of Electron Microscopy and Fine Structure Research
FIB	Focused Ion Beam
Ga	Gallium
GIS	Gas Injection System
HOPG	Highly Oriented Pyrolytic Graphite
IBID	Ion Beam Induced Deposition
keV	Kilo Electron Volts
KFU	Karl Franzens University
LMIS	Liquid Metal Ion Source
nA	Nanoampere
nm	Nanometer
ns	Nanosecond
PA	Parallel Arrangement
pA	Picoampere
Pt	Platinum
SA	Single Arrangement
SE	Secondary Electron
SEM	Scanning Electron Microscopy
Si	Silicon
TEM	Transmission Electron Microscopy
TLD	Through The Lens Detector

Introduction

A Dual Beam Instrument combines a Scanning Electron and a Focused Ion Beam Microscope. With such a system, it is possible to visualize a material surface, sputter material locally (ion milling) and deposit materials from gaseous precursors on the specimen surface by the aid of electrons and / or ions. Commonly used precursor gases result in platinum, tungsten, gold, copper, cobalt, iron, carbon layers and others. So far, deposition was preferably performed with ion beams called Ion Beam Induced Deposition (IBID) but also with electron as initiating dissociation particles named Electron Beam Induced Deposition (EBID). In this master thesis, only EBID processes was used due to the advantage over IBID that no ions during the deposition process are implanted within the sample and therefore the material damage is much lower and the deposition can be done with a higher lateral resolution. The disadvantage is that the EBID has a lower growth rate, so the deposition is much slower and the deposits show impurities (mostly carbon) which influence the intended functionality (e.g. conductivity for platinum deposits).

In this study, mainly, the feasibility for highly efficient deposition strategies will be discussed and the functionality of conductivity for platinum deposits will be characterized.

Motivation

The gas deposition in dual beam instruments could be applied for a wider range of nanotechnology applications, despite that it is until now primarily used for the formation of the protective layers e.g. during sample preparation for Transmission Electron Microscopy (TEM). Promisingly, with a further development in this field, more nanofabrication applications will be possible; such as, nano-conductors for repairing or prototyping, improved TEM-lamella preparation, fast nano-fabrications and possible sensor elements. The deposition process can be briefly described in a way that through a gas nozzle, a gas species of interest is flowed to the specimen surface where the gas is adhered and subsequently cracked through the energy input so that not only the metal, but also the remaining parts of the precursor gas build up the deposition. Yet, this process is not fully investigated and understood. To make EBID a real competitor to the other particle induced deposition techniques, the growth rate has to be increased while chemical impurities in the deposits must be strongly decreased to provide the intended functionality (e.g. conductivity for platinum deposits). This optimization is useful for diverse materials, where platinum is highly preferred for its simple handling, electrical conductivity and low cost. Out of the range of the other materials used as a deposition precursor, gold is more expensive, complicated to handle while in precursor state and could have a crystalline deposition behavior, whereas aluminum will oxidize or tungsten is dissociated from highly reactive fluorine (WF_6) components which can harm the surface. For this, it must be understood how the parameters influence the chemistry. To analyze more about the chemistry, an investigation must be carried out, where TEM is used for acquiring high-resolution images and quantitative analysis and Atomic Force Microscopy for the determination of the precise dimensions. But also through the electrical resistivity an interpretation of the chemistry could be done. Regarding this, it would be possible to get *in situ* measured data during deposition, providing information about the resistivity with a minimum analyzing effort which allows for the trial of many parameter-combinations. This resistivity information including other analysis methods will allow for a better understanding of the deposition process and hence a better optimization.

Therefore, this work focuses on two intentions: *i*) the feasibility of previously developed high efficiency deposition strategies (EBID max smooth) and *ii*) as a first step to characterize the functionality of conductivity for platinum deposits an electrical stage to access directly the performance of conductive pads in dependence on the deposition strategies.

Outline

- The first part (chapter 1) describes the basics for the reader, where the used microscopes with their working-mechanisms (chapter 1.1) and deposition fundamentals (chapter 1.2) are given.
- In the next part (chapter 2) the investigation techniques which were needed to estimate the variations of the used pattern parameters in relation to different dimensions are described.
- The chapter “Technical preparations” (chapter 3) describes the construction of the setup which allowed the *in situ* measurements. The theoretical information on the four point resistor measurement is given in chapter 3.1. Next subchapter (chapter 3.2) provides information about the specimens used in this work. The construction of the hardware is described in the chapters 3.3 to 3.6; and finally the software in chapter 3.7.
- The first results and validation of the *in situ* measurements will be given in chapter 4.3 and chapter 4.4. In chapter 4.6 and chapter 4.7, the characteristics of a possible sensor are presented and the independency of measurement tool during deposition is described in chapter 4.5 and chapter 4.8.

1 Fundamentals

1.1 SEM and Focused Ion Beam

The Scanning Electron Microscope (SEM) is a microscope that uses a focused electron beam which scans over the sample to generate an image from the surface of a specimen. It allows a high magnification range from mm up to about 5 nm. A list of different microscopes and their magnification range is shown in Figure 1-1 while Figure 1-2 represents the principle parts of a Scanning Electron Microscope.

On the other hand, the Focused Ion Beam (FIB) instrument uses a focused ion beam which scans over the sample to generate an image or to do ion milling which is applied for material removal. In a typical Dual Beam Instrument both FIB and SEM systems are combined together as one microscope. For the FIB work in the present master thesis, a Nova 200 Nanolab Dual Beam System from FEI was used which is shown in Figure 1-3.

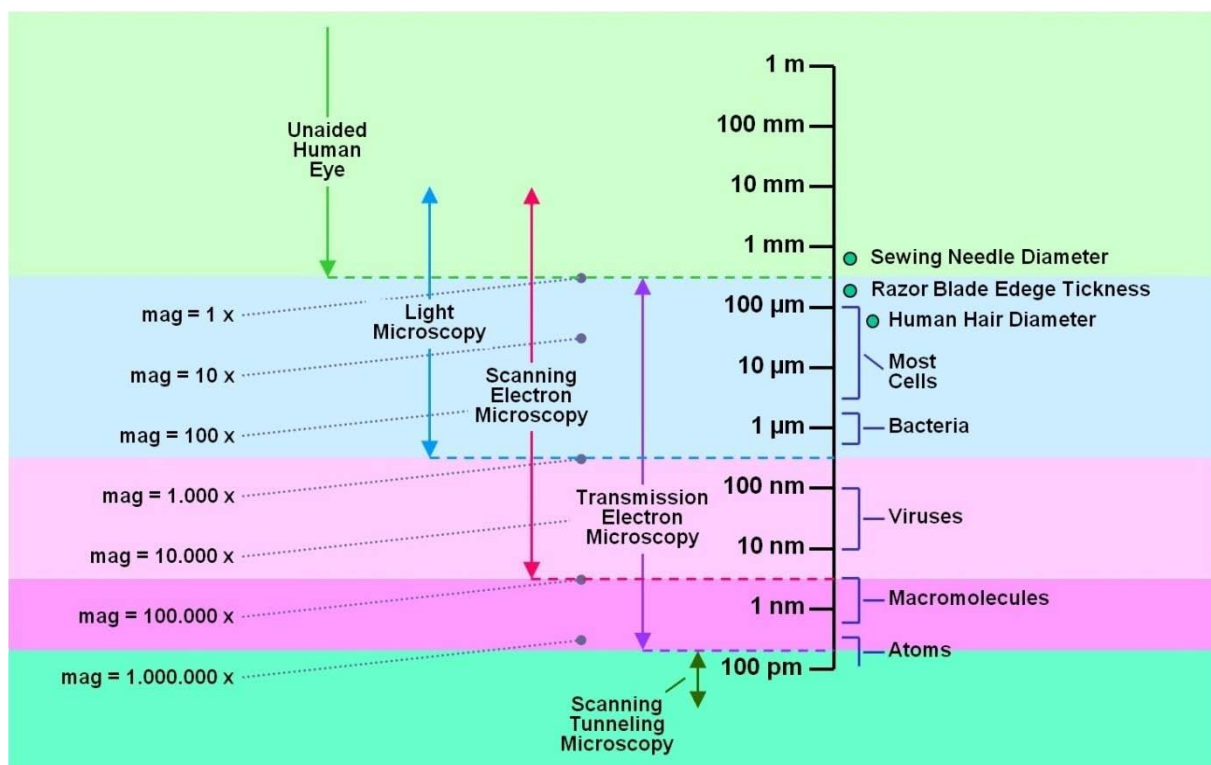


Figure 1-1: Different microscopy ranges. [9]

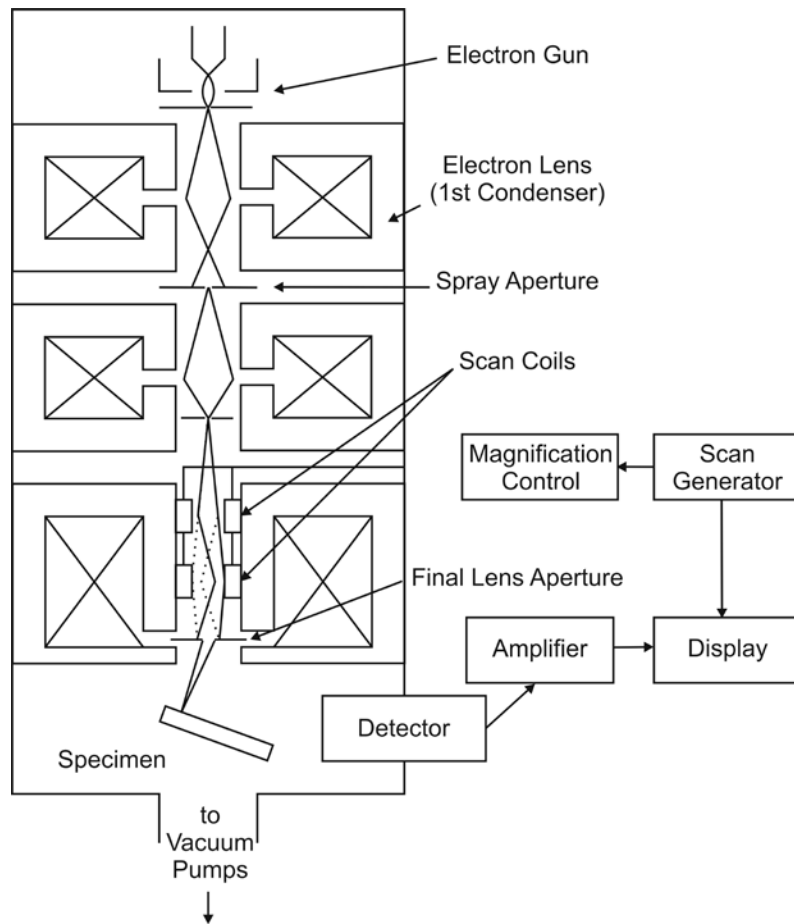


Figure 1-2: Schematic drawing of the basic parts of a Scanning Electron Microscope, such as electron source, coils for focusing and scanning, two apertures, the specimen and the detector. [6]

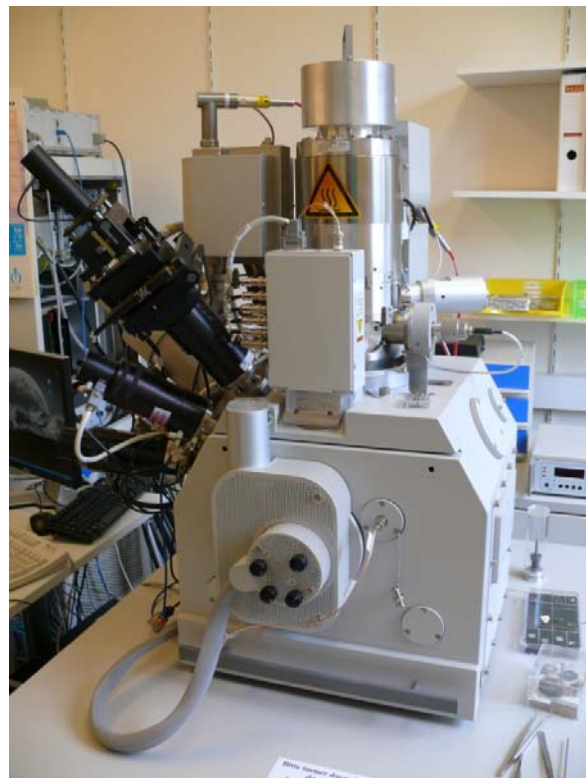


Figure 1-3: The used SEM / FIB Dual Beam Microscope (FEI Nova 200 Nanolab).

The following parts are going to focus on the fundamentals of electron optics, while further parts will concern the main concepts of ion beams.

1.1.1 SEM electron optics

The purpose of electron source and optics in an SEM is to produce a small electron probe at the specimen by demagnifying the electron beam to the smallest size. Primarily in an SEM, the electrons are produced by an electron gun with different sources. There are mainly three types of electron gun in general use which are: [6]

- Tungsten hairpin
- Lanthanum Hexaboride Electrode (= LaB_6 electrode)
- Field Emission Electrode (Cold, Thermal or Schottky)

The oldest and best known electrode is the tungsten hairpin which is shown in Figure 1-4. The tungsten wire, which is heated with an electric current to 2700 K, is about 0.1 mm thick. One drawback of tungsten is its short lifetime and the coarse tip size. However for x-ray measurements it is the best choice because of its stability against high current. It is in addition having low costs compared to the other sources. [6]

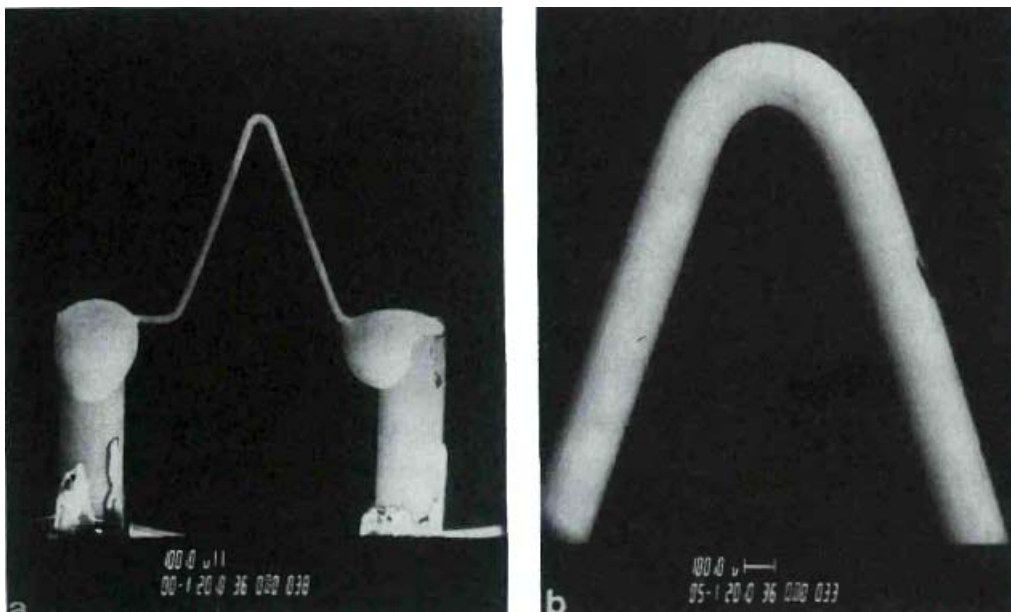


Figure 1-4: SEM image of a tungsten hairpin filament. [6]

The most common high brightness electrode is the Lanthanum Hexaboride Electrode (= LaB_6 Electrode) which is shown in Figure 1-5 and Figure 1-6. It is a block of Lanthanum Hexaboride electrode, heated to form thermionic emission. Its lifetime is higher than the tungsten hairpin electrode as well the source size and the energy spray are better. [6]

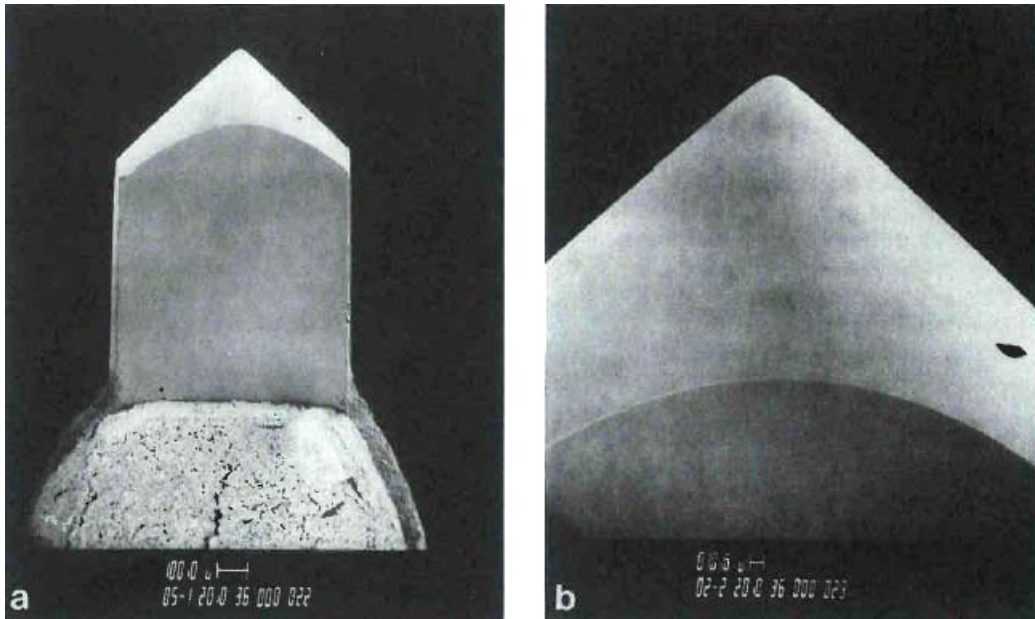


Figure 1-5: SEM image of a Lanthanum Hexaboride filament. [6]

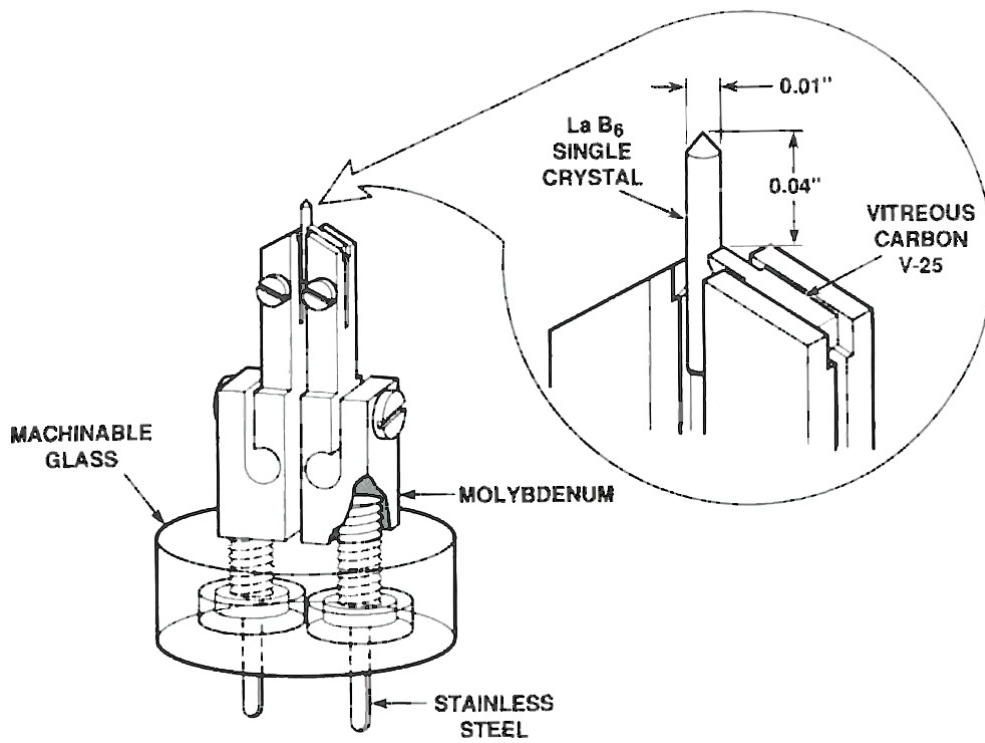


Figure 1-6: Mechanical sketch of a Lanthanum Hexaboride Electrode. [6]

The Field Emission Electrode is also a tungsten electrode but the working mechanism is different. It is a cold electrode, that means that it is not heated. The electrode is an extreme small tip (see Figure 1-7). With a high electrostatic field the electrons can pass the potential barrier by tunneling. This is possible because of the extreme high field which is produced by the geometric form and the high voltage electric field. [6]

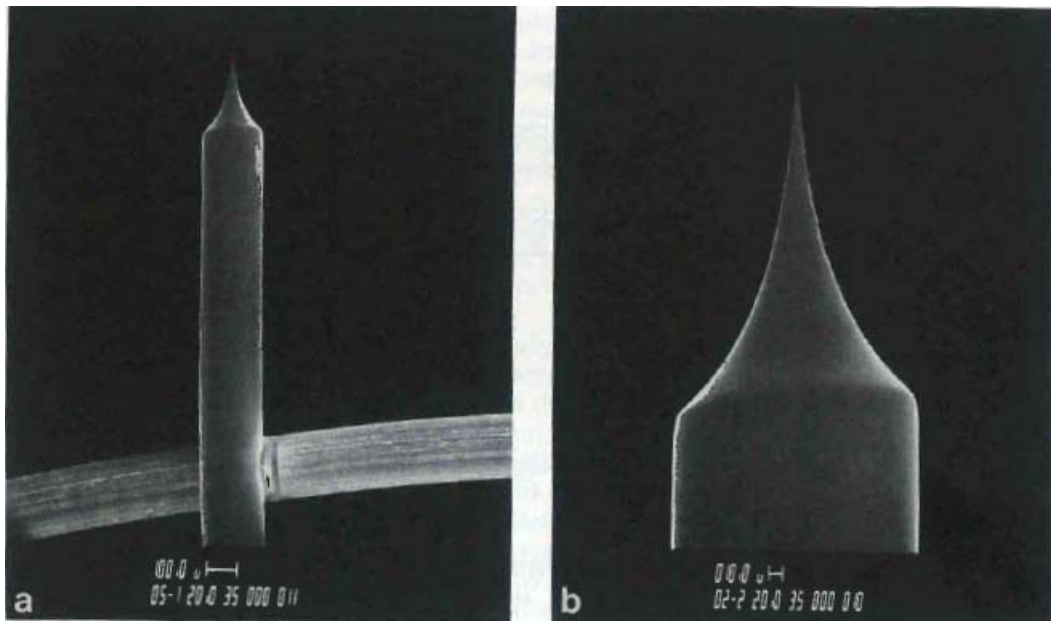


Figure 1-7: Mechanical sketch of a field emission electrode. [6]

A summary with the technical data is shown in Table 1-1. [6]

Table 1-1: Comparison of three electron sources. [6]

Source	Brightness	Lifetime	Source size	Energy spread ΔE	Beam current Stability
Tungsten hairpin	10^5 A/cm ² sr	40–100 h	30–100 μ m	1–3 eV	1%
LaB ₆	10^6	200–1000	5–50 μ m	1–2	1%
Field Emission					
Cold	10^8	>1000	<5 nm	0.3	5%
Thermal	10^8	>1000	<5 nm	1	5%
Schottky	10^8	>1000	15–30 nm	0.3–1.0	2%

The electrode is in a Wehnelt cylinder which focuses the electrons with a negative voltage. Electrons which leave the electrode are repelled by the negative potential. This is shown in Figure 1-8. [6]

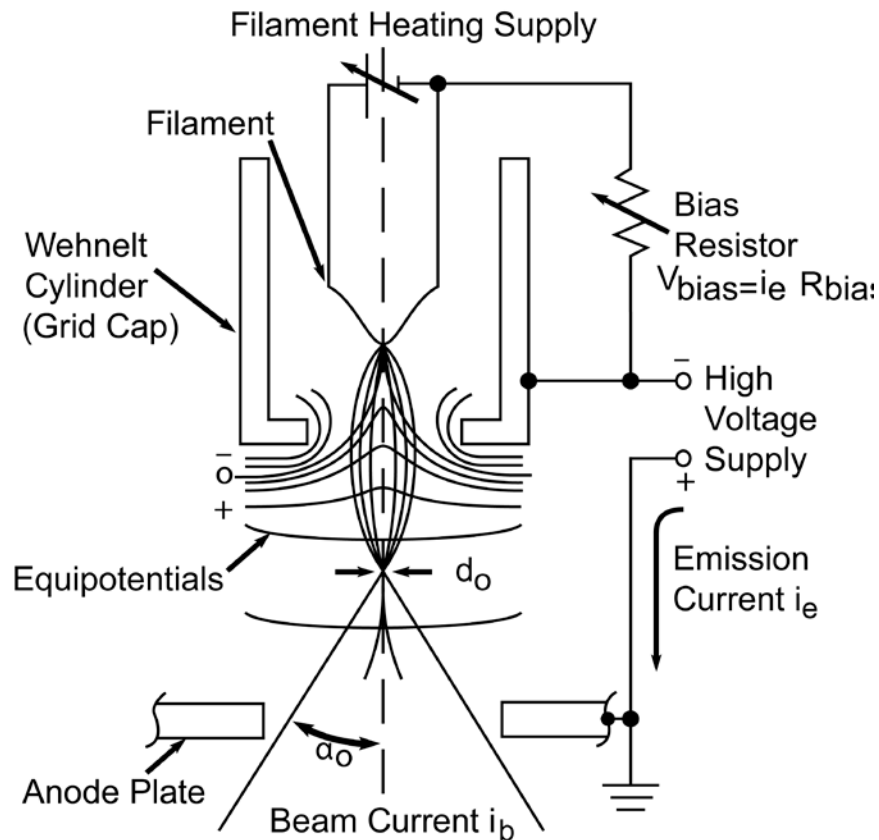


Figure 1-8: Schematic diagram of the Wehneltcylinder and surrounding elements. [6]

The electrons which are emitted through the electron gun are focused through electromagnetic lenses, as described below:

- One to two condenser lenses demagnify the electron beam to a small spot (see Figure 1-2). With these coils, the spot size – determining beam current and influencing the achievable lateral resolution - can be adjusted.
- Objective lenses are used for finalizing the electron beam and for the scanning movement with the scanning coils (see Figure 1-2).

Electron lenses have different aberrations which results in a finer resolution. The most important of those are: [6]

- spherical aberration
- chromatic aberration
- aperture diffraction
- astigmatism

Spherical aberration

An electromagnetic lens bends electron trajectories different on the outside of the lens than in the center of the optical axis. So the electrons from the outside cross the image plane not on the same position as the center electrons. Eventually, the electron spot has a permanent blur and cannot be focused to a point. This is sketched in Figure 1-9.

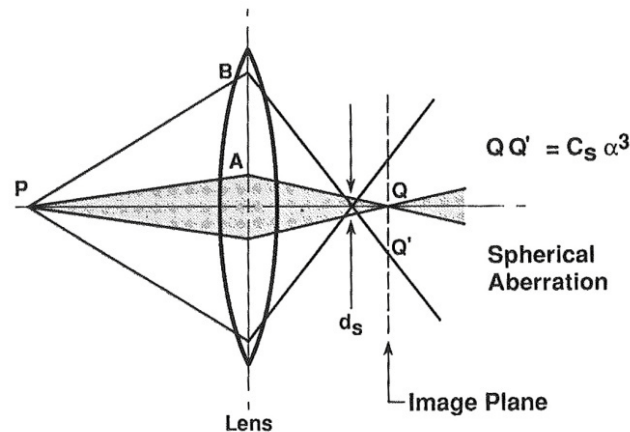


Figure 1-9: Demonstration of the spherical aberration. [6]

Chromatic aberration

This aberration occurs if the electron beam has a different wavelength and so a different energy. If the energy is smaller the beam will bend more and the beam crosses before the image plane. Again - as in spherical aberration - the electron spot has a permanent blur and cannot be focused to a point. This aberration is shown in Figure 1-10

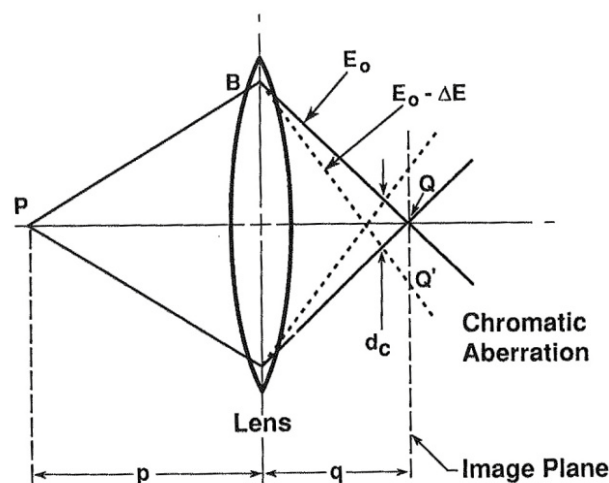


Figure 1-10: Demonstration of the chromatic aberration. [6]

Aperture diffraction

If the aperture is very small, which is only in special microscopes and not standard, the beam will diffract instead of building up a single point at the Gaussian image plane. This results in a lesser resolution and is illustrated in Figure 1-11.

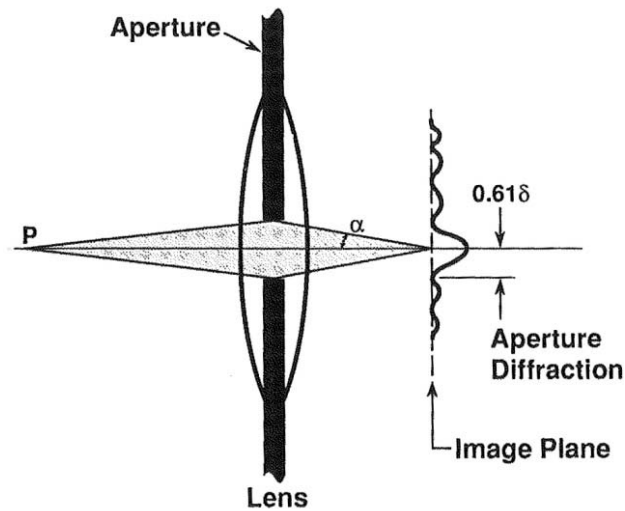


Figure 1-11: Demonstration of the aperture diffraction. [6]

Astigmatism

Electromagnetic lenses do not have perfect rotation symmetries due to the fact of mechanical errors, magnetic inhomogeneities of the polepieces and, asymmetry in the windings. This failure can be corrected with additional lenses (see Figure 1-2). The impact of this aberration is shown in Figure 1-12.

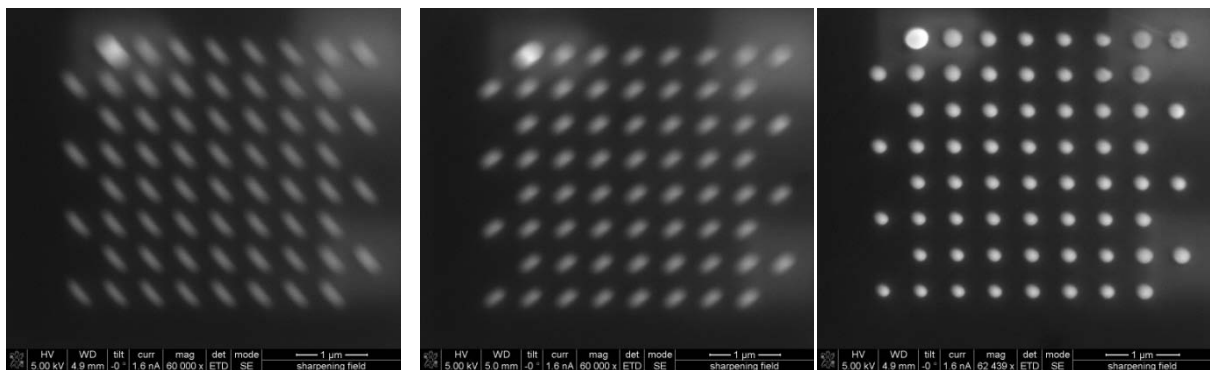


Figure 1-12: The first two images (left and middle) show under- and overfocused images respectively. It is visible that the images are diagonal distorted. In the last image (right) the astigmatism is corrected, resulting in a higher resolution.

1.1.2 Signal detection and imaging of electrons

When the primary electron beam interacts with the target material in an SEM, they interact within a teardrop shaped interaction volume of the material. The type of interaction can be in the form of elastic or inelastic scattering. This simulation, which is done with the software CASINO [3], is shown in Figure 1-14.

Elastic scattering represents high angle deflection of the electrons by the host atoms of the materials where the energy is conserve. In inelastic scattering, the incident electrons collide with the host electrons of the specimen, resulting in low angle deflection but loss of initial energy. This is sketch in Figure 1-13.

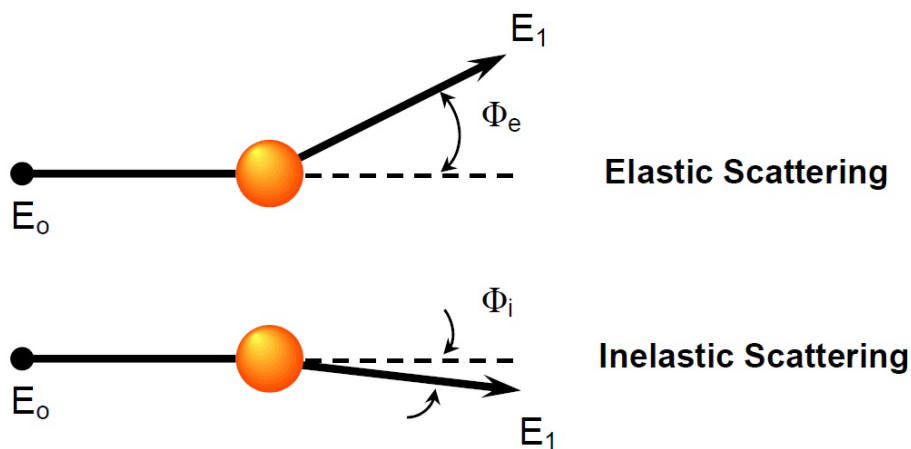


Figure 1-13: Comparison between elastic and inelastic scattering.

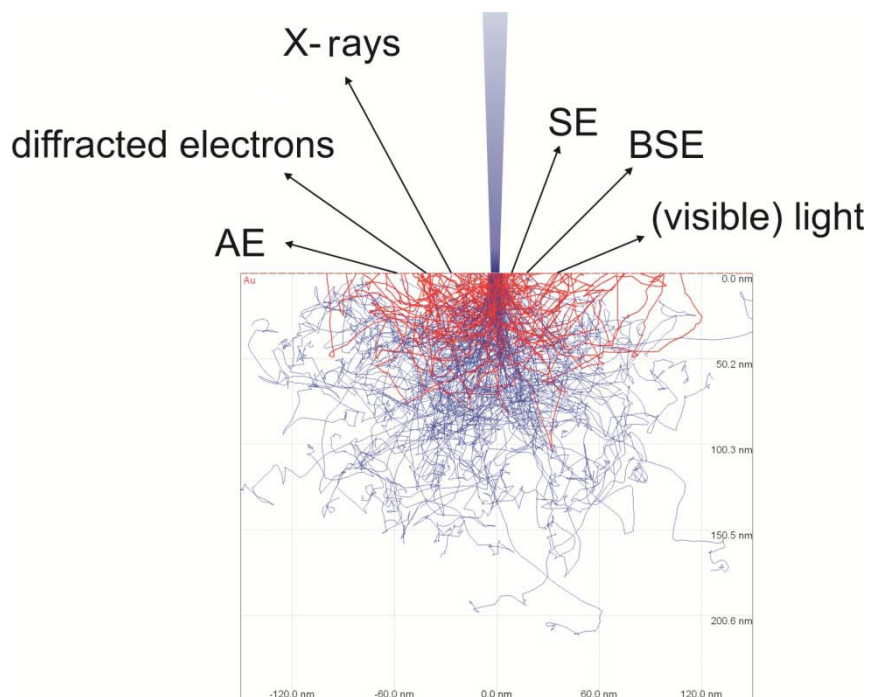


Figure 1-14: Interaction of the electron beam with the surface of a gold specimen. The red trajectories show the interaction volume for escaping electrons, while the blue ones stand for those which are trapped. [14]

The most used interaction signals are Secondary Electrons (SE), Backscattered Electrons (BSE) and x-rays, in addition to Auger Electrons (AE) and visible light. An energy distribution of the integration signals is shown in Figure 1-15.

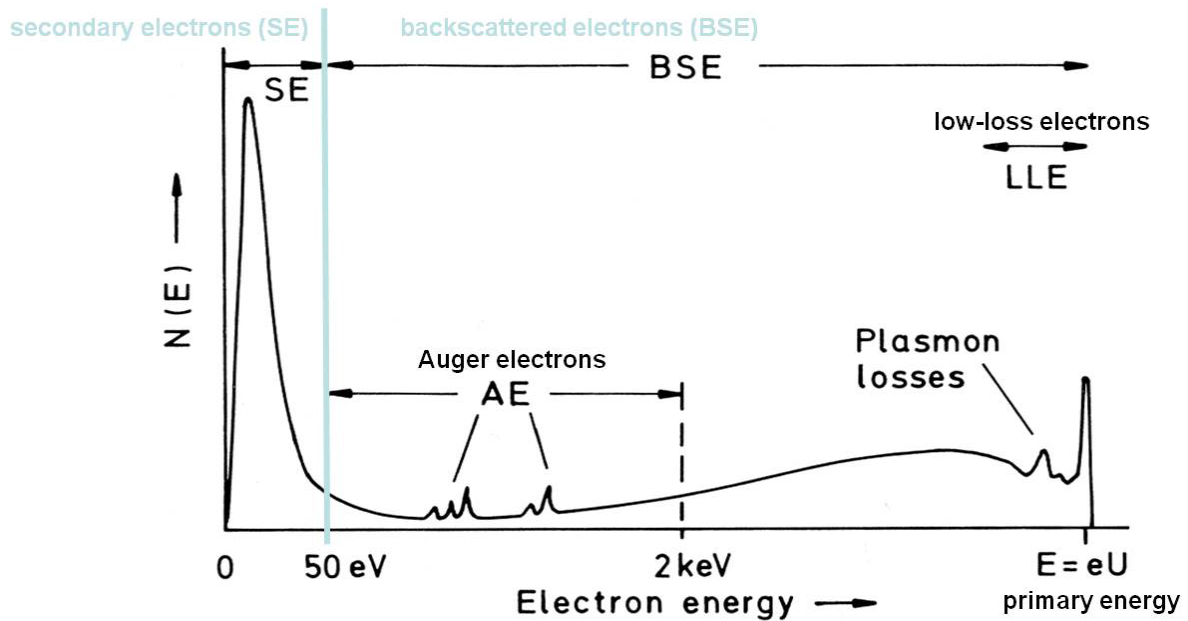


Figure 1-15: Energy distribution of electrons which are produced by the primary beam. [12]

Secondary electrons are generated by inelastic scattering. The primary electron beam collides with the valence electrons of the specimen material and knocks an electron out. This electron that escapes from the specimen has a low energy below 50 eV, as shown in Figure 1-15. If a SE is generated in a deeper layer of the material, it will not get out because of the low energy. The average free way length is though the low energy very short, through this, only the SE from the surface can leave the specimen surface and reach the detector.

Backscattered electrons are high energy signals which are created by elastic scattering. They get scattered by an atom nucleus so they change the direction without an energy loss whereas they can also have an energy loss in relation to the primary electron energy. This occurs when the electron beam interacts inelastically. One is the SE like described above, the other is the incoming beam minus the energy increase from the SE. Logical the BSE can do this again always losing more and more energy. This is the reason why the Energy range varies from SE up to primary beam (see Figure 1-15). The penetration depth is high and material information comes from the deep regions of the material. But if the material has a heavy atomic mass in the case of same electron beam parameters, the electron beam will be scattered more which gives a smaller interaction volume (better resolution) and also the energy loss is higher, so that the energy of the BSE will be lower than that in a low weight elements.

X-rays are generated by the Bremsstrahlung and are used for making an Energy-Dispersive X-ray spectroscopy (EDX) to determine analytical information.

The signals generated then are collected by a detector. The typical detection system for SEs is by means of an Everhart-Thornley Detector (ETD) which is shown in Figure 1-16. The electrons (both SE and BSE) are collected by a positive voltage while SE are strongly drawn to the detector whereas BSE do not, since they have higher energies. The electrons hit a scintillator and are subsequently amplified by a photomultiplier to generate a signal. If the positive voltage is switched to a negative voltage (-50V) the SE are not drawn to the detector and primary the BSE are measured. So one can switch between SE and BSE. Another detector is the through-the-lens detector (TLD) which is placed inside the electron column. By using the electromagnetic field of the electron column it is possible to collect primary the electrons which are in a smaller area than the ETD. This results in a better lateral resolution.

SE in combination with the ETD gives a good surface image with best spatial resolution and good 3D-look. The reason is that only electrons from the surface can reach the detector and from there they were collected by the positive electric field which influences the low energy electrons strong. The 3D-look occurs because of the position of the detector. Electrons which face the detector more, seems brighter.

BSE usually gives a material contrast of which heavy materials appear bright and low weight materials dark. Here the spatial resolution is worse than that of the SE because the escape area is bigger and the 3D-look is not pronounced.

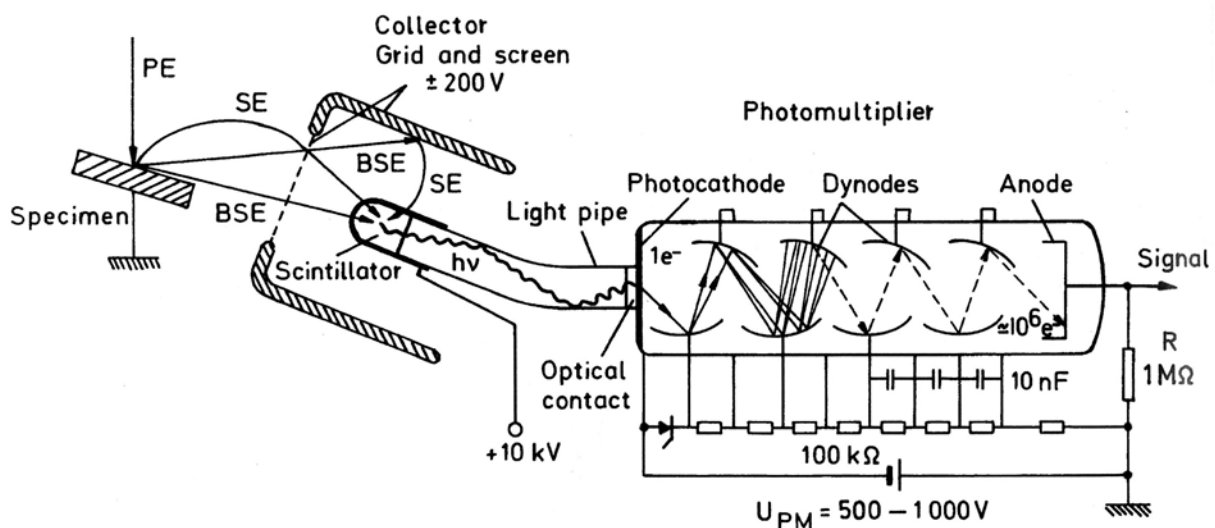


Figure 1-16: An Everhart-Thornley detector. [6]

1.1.3 Ion Beam Optics

An electron microscope can be designed as using ion beam instead of electron beam, in the form of a Focused Ion Beam microscope. FIB uses a focused beam of metal ions generated by the liquid metal ion source (LMIS) which has a higher energy as electrons [16] (Figure 1-17). The principle function of such a source is that a tungsten tip is heated by an electric current to heat a reservoir with metal. Usually in FIB systems, gallium is commonly preferred as the ion source. The gallium source gets fluid at a temperature of 29.8°C. With the help of a tungsten needle and the extractor electrodes a spot of about 5 nm in diameter is achieved and that direct from the ion source without focusing. Because of the fact that the ion material is a liquid metal it is called Liquid Metal Ion Source (LMIS). [16]

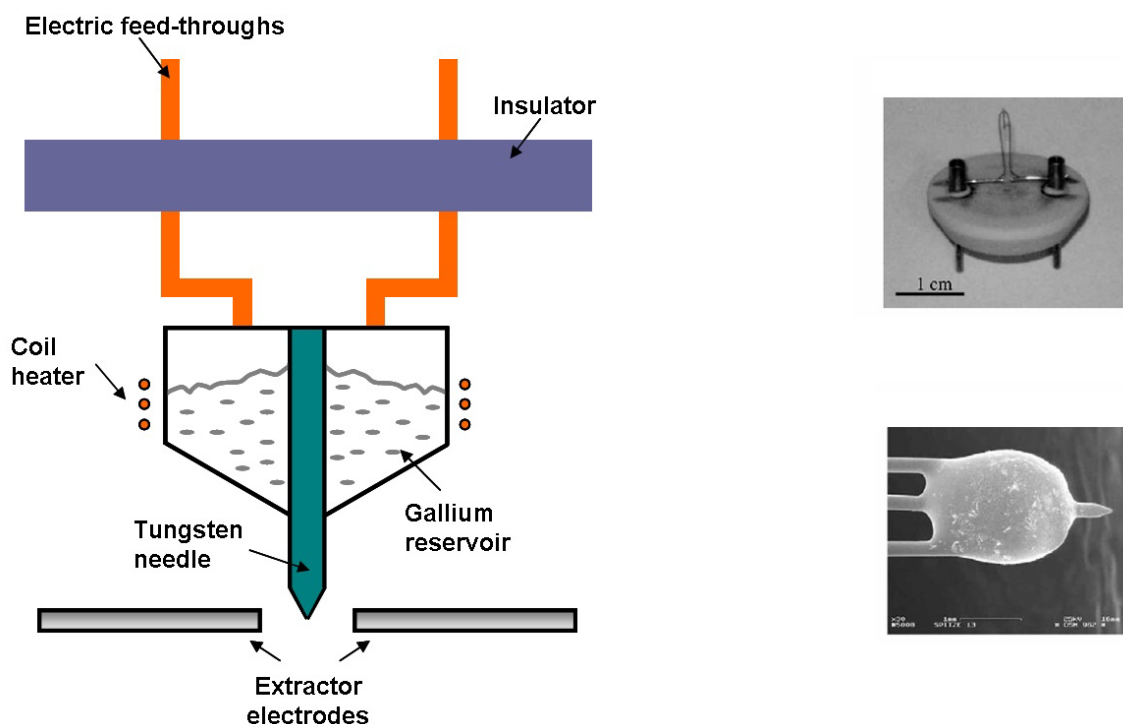


Figure 1-17: The left image shows a principle sketch of a Liquid Metal Ion Source. In the right top LMIS socket with needle is presented and the right bottom shows the filament filled with liquid metal droplet. [1]

Similar to a SEM, the FIB also uses optics to form a focused beam at the specimen surface. A typical FIB column is sketched in Figure 1-18. The main difference between electron and ion optics is that the FIB is equipped with electrostatic lenses instead of magnetic lenses. The ion source produces a beam which is focused and perpetuated with the condenser lenses. After that, an aperture cuts off the outer parts and the ion beam goes through a mass filter where - with an electrostatic and a magnetic field - the lower and higher masses of ions get filtered. This is needed because the LMIS produces also isotopes and the beam might be contaminated

with other materials. This followed by the beam blaker, for blanking the beam and finally the deflectors for scanning and astigmatism. The final beam is then focused in the objective lens. Depending on the application, emitted particles can be collected by appropriate detectors that are located in the specimen chamber. Conventional SEM detectors can be used to detect electrons, whereas the ions sputtered from the material can be collected by many detector systems, such as charge electron multipliers [6].

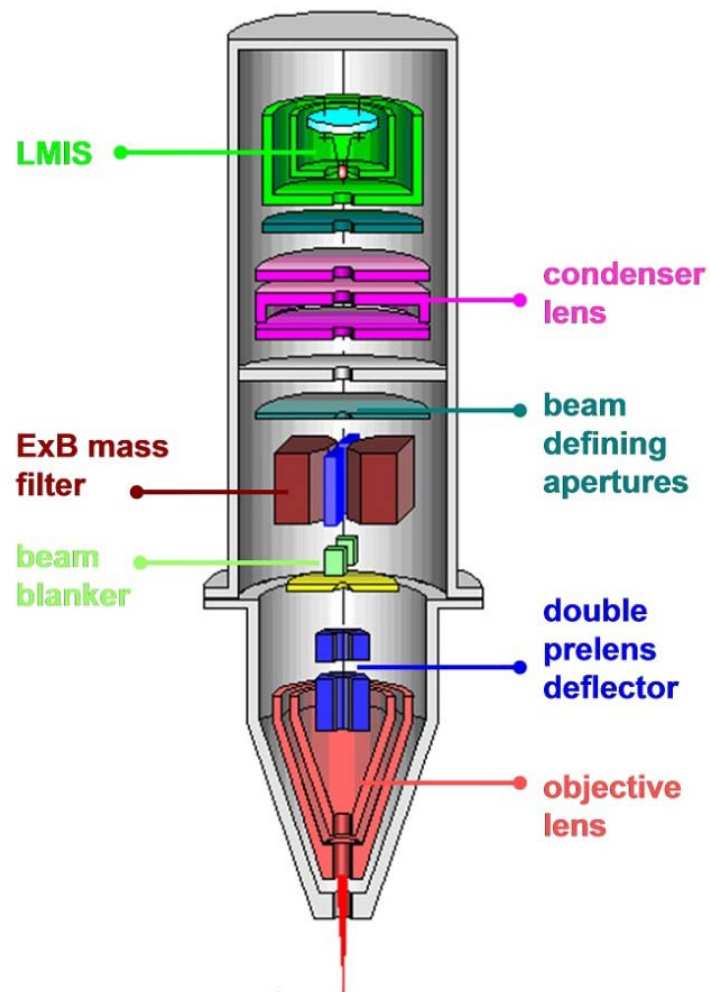


Figure 1-18: Sketch of the principle construction of a FIB. [16]

1.1.4 Signal detection and imaging of ions

The resultant interaction effects between ions and the specimen is much different than that of electrons, due to their massive character. Because ions are heavier than electrons, they cannot easily penetrate within the atoms of the target material and they finally gain a high momentum. The transfer of energy from the ion to the specimen can be in the form of : [16]

- ion reflection and backscattering
- electron emission
- electromagnetic radiation
- atomic sputtering and ion emission
- specimen damage
- specimen heating

The pathways of the interaction between the ions and the specimen are shown in Figure 1-19

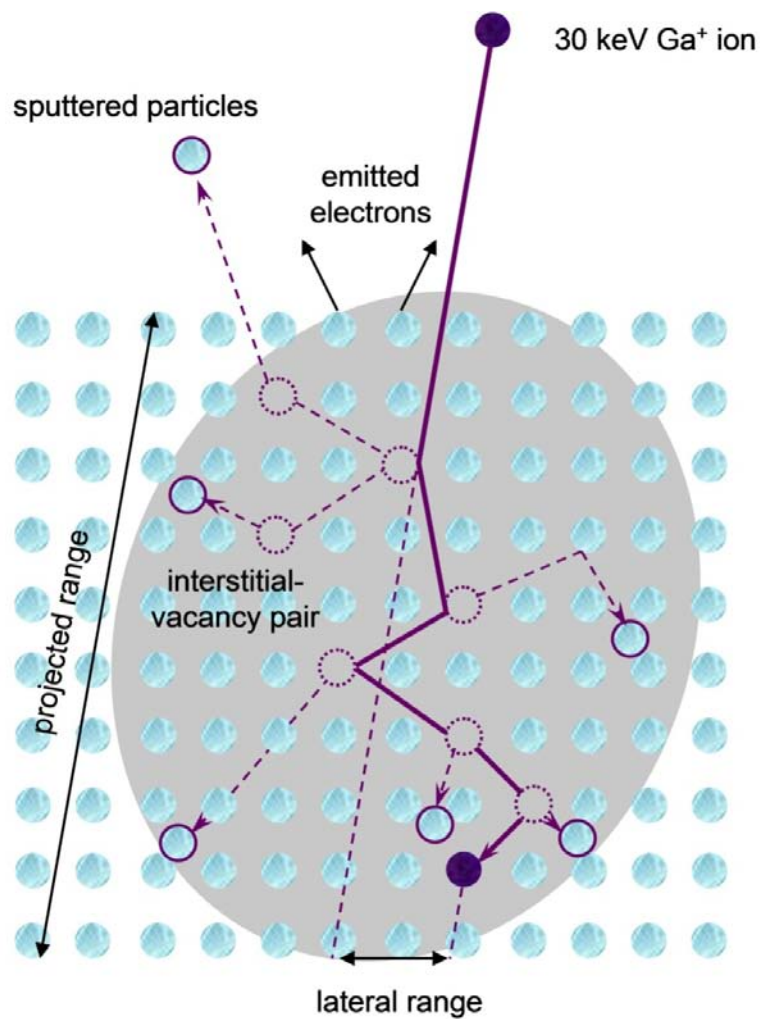


Figure 1-19: Collision cascade of a gallium ion in a crystal lattice [16]

However, the specimen damage due to ion beam-specimen interaction cannot be excluded. Depending on the ion energy, the ion dose and the nature of the target material, the interaction might be resulting in sputtering, amorphization, swelling of the material, redeposition and ion implantation. The operation therefore has to always consider the aftereffects of ion beam applications.

The main advantage of the FIB is that one can make not only imaging, but also many nanostructuring applications [20]. Of a large spectrum of ion beam applications, the most commonly used is the ion milling, in particular for the preparation of TEM lamellas [6]. With the removal of the material, which is defined in patterns, the material surface can be processed. In Figure 1-20 FIB-milled Styria armorial bearing is shown. Furthermore, ion milling combined with the electron beam could also be used to analyze a material in three dimensions, by means of slice and view process [17]. This could then be reconstructed by a computer program for creating a 3D model. An example for such an application is shown in Figure 1-21.

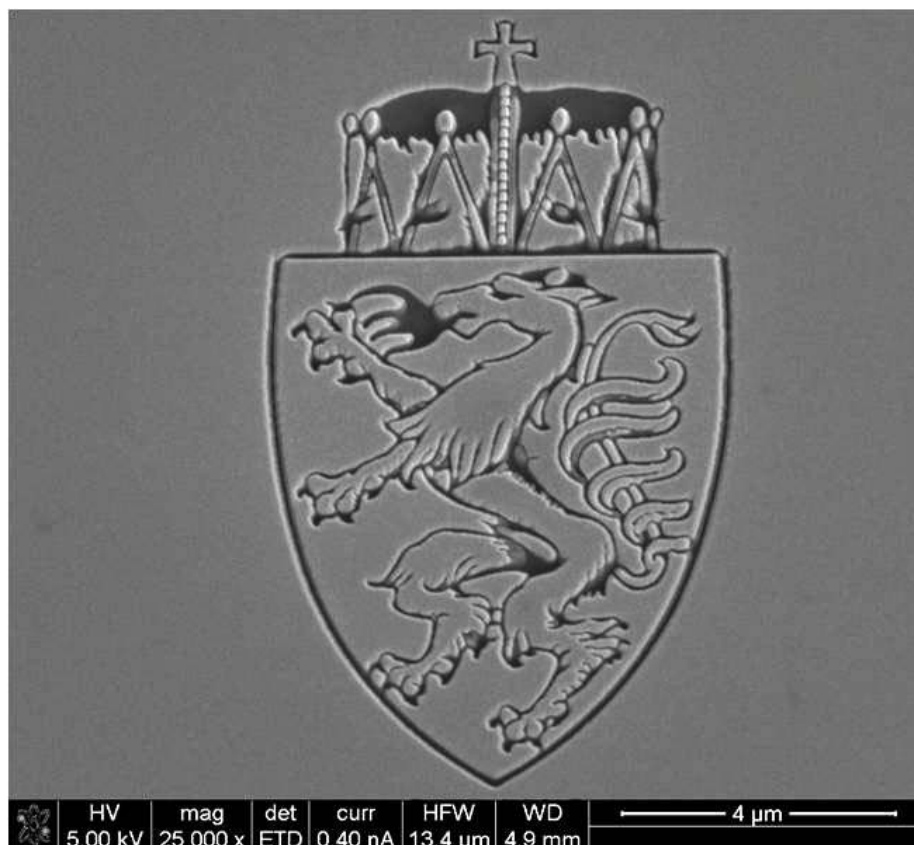


Figure 1-20: Demonstration of FIB based ion milling. The golden surface was milled with a depth of 100nm and 30 nm of defined width for the lines of the feature. [12]

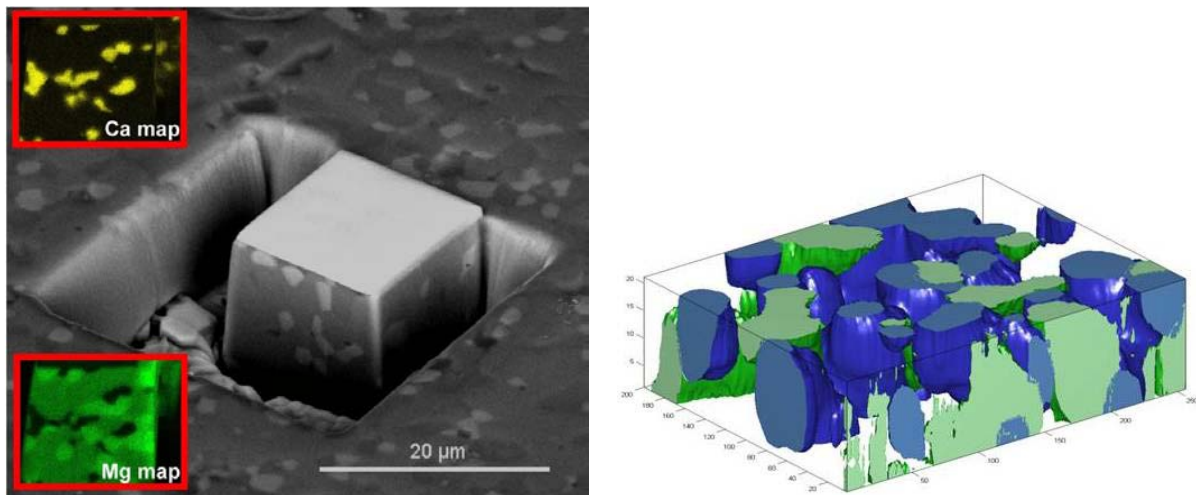


Figure 1-21: The images show the 3D microstructural characterization of a ceramic sample. The image on the left side shows the slice and view process. On the right side, the reconstructed image is shown, demonstrating blue regions for is calcium and green for magnesium. [12]

With the use of gas injection systems (GIS) in dual beam instruments, is it possible to do material deposition on the sample surface [6]. Particularly GIS are used for nanofabrication purposes, which will also be extensively mentioned in this master thesis. This is possible by exposing a special precursor gas with a gas nozzle to create deposition by means of electron or ion beams. All these dual-beam applications especially allow for the preparation of TEM lamellae where a cross-section can be lifted out from a destined point by the help of a micromanipulator, transferred to a TEM grid, and finally thinned below 100 nm using ions [21]. Such a TEM preparation is shown in Figure 1-22.

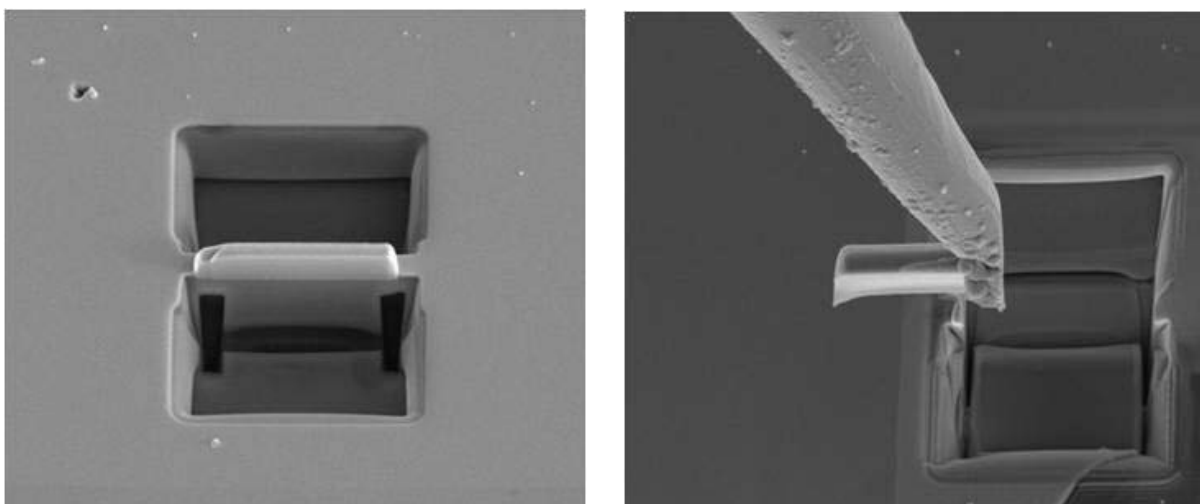


Figure 1-22: FIB based TEM specimen preparation. The left image shows the pre-milled cross-section is the right image shows the section which is to be mounted on a TEM grid using the micromanipulator. [12]

1.2 Deposition

The gas injection systems (GIS) in a dual-beam FIB allow for doing deposition using a special precursor gas. By means of Ion Beam Induced Deposition (IBID), even a very small scale on the material surface can be coated using ion beams to deposit the precursor material within the defined pattern. In Figure 1-23 the fundamentals of such a deposition is shown. From a gas nozzle the precursor gas flows through the specimen surface where it is adsorbed and then diffused on the surface until it is desorbed after a residence time.

If the diffused gas is hit by the ion beam, it will crack and the material will bound to other platinum atoms forming small platinum crystals whereas the volatile products are pumped away from the chamber. Moreover, the ions from the ion beam will be implanted. With a 30 keV gallium ion beam this implementation would be 5 – 40 nm, in dependent of the material [16]. This could be a problem for example if a TEM lamella is to be prepared, and therefore a protective coating is deposited on the top of the cross-section. But if this coating, which should protect the specimen material, changes the material through ion implementation and local heating (interaction see chapter 1.1.4), it can lead to undesired aftereffects. Such ion interactions only for ion milling are shown in Figure 1-24. With an electron beam this is not likely to happen, as well as the spatial resolution of the deposition is much better. However, such an Electron Beam Induced Deposition (EBID) is not as fast as the IBID, and therefore an optimization for the electron beam growth rate is needed. The growth rate difference between IBID and EBID is demonstrated in Figure 1-25. Such an optimization is possible by changing instrumental parameters, such as dwell time, voltage, beam current, pitch and defocus. These parameters can also change the chemistry of the deposition according to the alterations in the metal-carbon ratio.

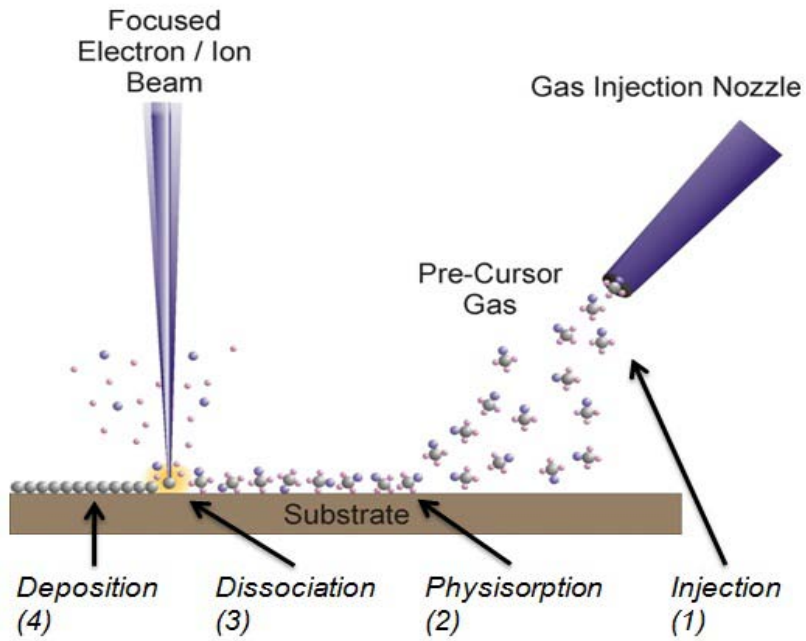


Figure 1-23: The basic application flow of a deposition. [12] modified

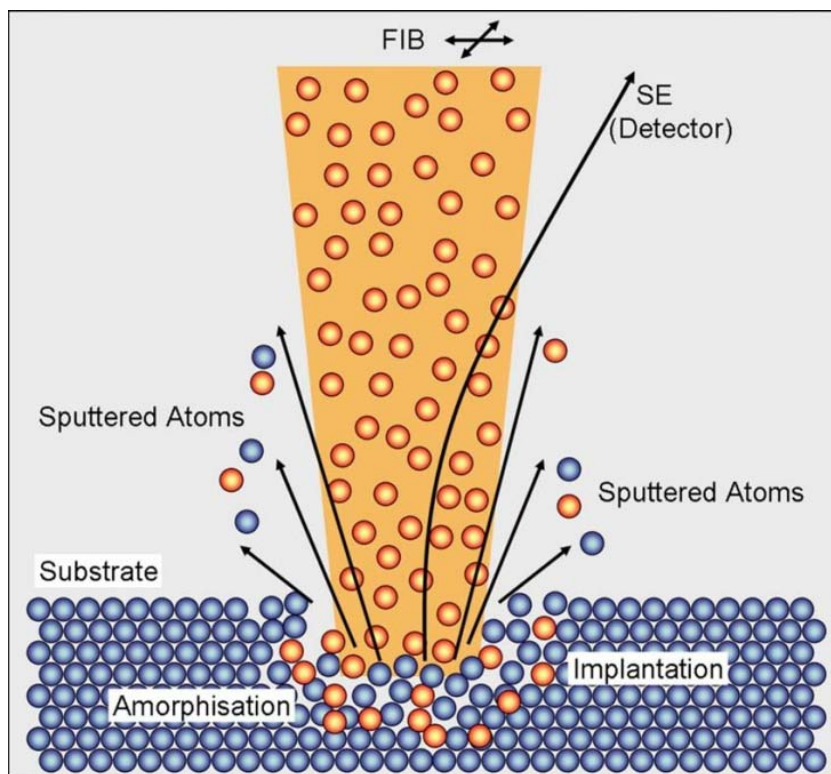


Figure 1-24: Principles of ion milling using a FIB. Ion atmospheres the surface and sputter atoms out, while the ions implant within the material. This is not only valid for milling but also for deposition. [18]

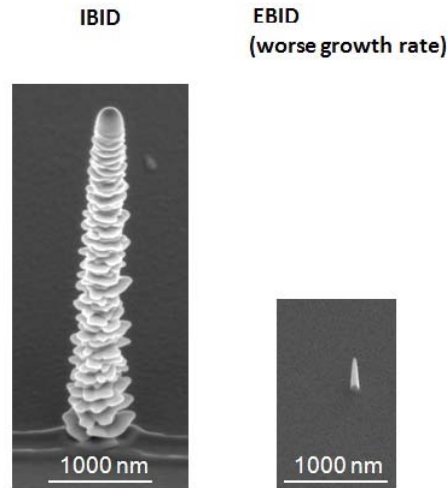


Figure 1-25: Left image shows an IBID needle, while the right image presents the worse growth rate of EBID.. The structures on both images are fabricated with same instrumental parameters, but using ion beam and electron beam respectively. [12]

1.2.1 The Precursor

A precursor material is needed to be used in the gas injection systems. This could be a solid, a liquid or a gaseous precursor. In this master thesis, only gaseous precursor of Trimethyl-Methyl-Cyclopentadien-Platinum [12] is used. The gaseous precursor has the advantage that no pre- and after treatment like manual covering with new precursor or removing is needed. Nevertheless, many other precursors with different elements are also available with the most common ones are platinum, tungsten, gold, copper, cobalt, iron and carbon [2]. Technical data and chemical structure is shown in and Figure 1-28. The electrons which interact with this precursor crack the bonding and so the metal could form small crystals of 1.7 nm in diameter embedded in a carbon matrix resulting in ca. 15 at.% metal content (see Figure 1-27) while the volatile products are pumped away from the chamber. Figure 1-26 shows the cracking of a precursor. Not only the primary electrons, but also secondary or backscattered electrons may crack the bonding since they have sufficient energies. This leads to an unintentional deposition in the near area of the electron beam which is called spray effect. A big problem occurs when the cracking is not that perfect. It is possible that more electrons which could crack the precursor gas are available, as precursor gas or the other way around. For example, the precursor gets not completely cracked or the dissociated organic fragments are build in the deposition. However, this rate is adjustable with the deposition parameters (to see the effect of such improvement see chapter 1.2.4). A hypothesis suggests that the gas does not crack like the principle shown in Figure 1-26, but with an intermediate step. [12]

Table 1-2: Technical data from Trimethyl-Methyl-Cyclopentadien-Platinum. [24]

Color and Form:	off-white powdr.
Molecular Weight:	319.32
Melting Point:	30-31°C
Boiling Point:	(subl. 23°C/0.053mm)
Vapor Pressure:	no data
Specific Gravity:	1,88
Odor:	metallic odor
Solubility in Water:	insoluble

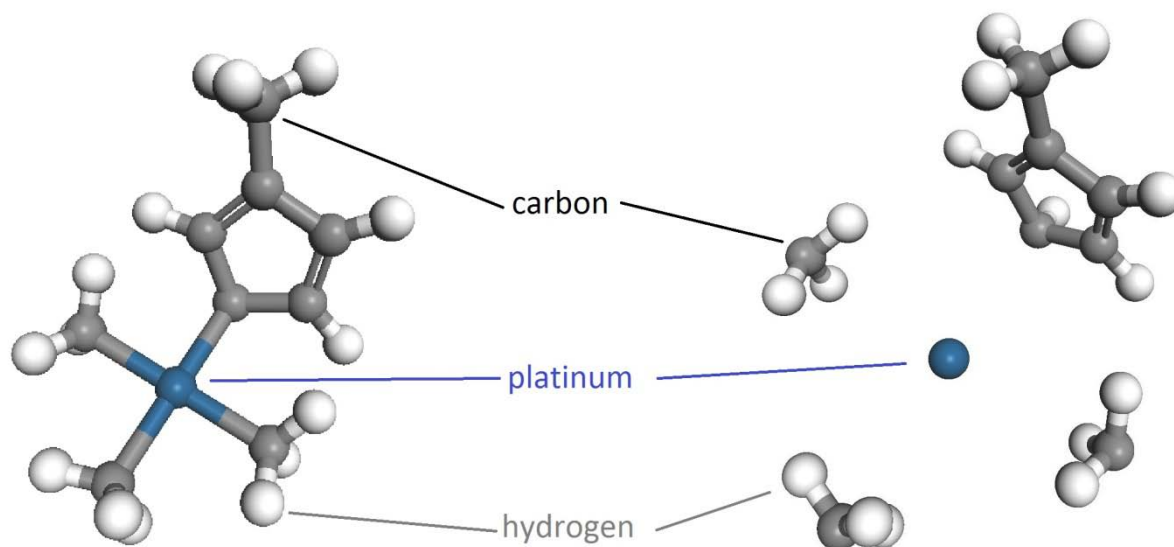


Figure 1-26: On the left side a precursor gas is shown. The blue atom with 4 bonding is the metal atom. The gray atoms are carbon and the white are hydrogen. The right picture shows the cracked precursor gas. The metal bonds to the surface, the hydrocarbon will be pumped away. [12]

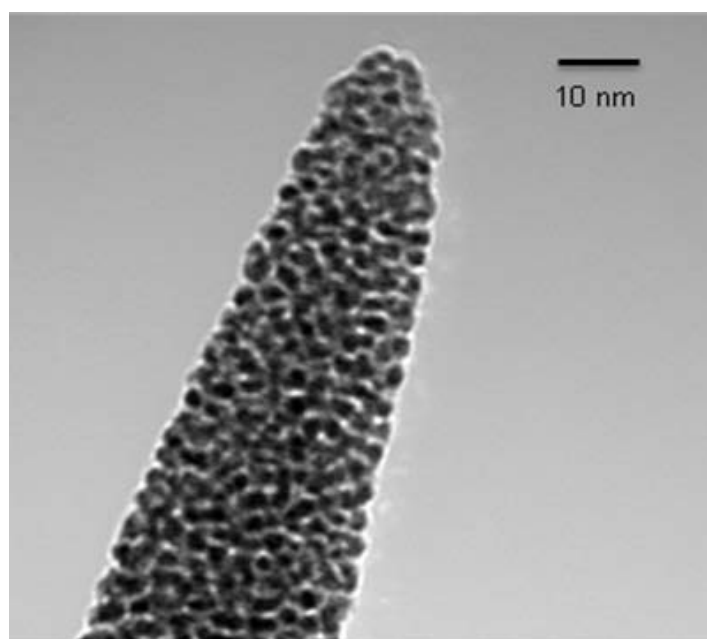


Figure 1-27: TEM image of a needle deposited with EBID. One can see the small crystals of platinum in the carbon matrix. [11]

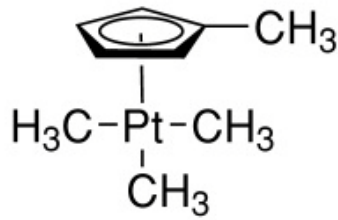


Figure 1-28: Chemical formula of Trimethyl-Methyl-Cyclopentadien-Platinum. [23]

1.2.2 Precursor Adsorption and Diffusion

As mentioned in chapter 1.2, the injected precursor gas hits the specimen surface and then adheres to the surface. Now the precursor gas will move on the surface by diffusion (this is sketched in Figure 1-29) and leave the surface after a residence time. In addition, the flux of the incoming gas from the gas nozzle covers the surface, where the gas could adhere on the specimen. These are two mechanisms which are combined in a flat deposition, whereas in a higher deposition rate the diffusion is hindered through the high increase and only the incoming gas flux will adhere to the surface and yield to the growth rate. This is shown in Figure 1-30 and Figure 1-31.

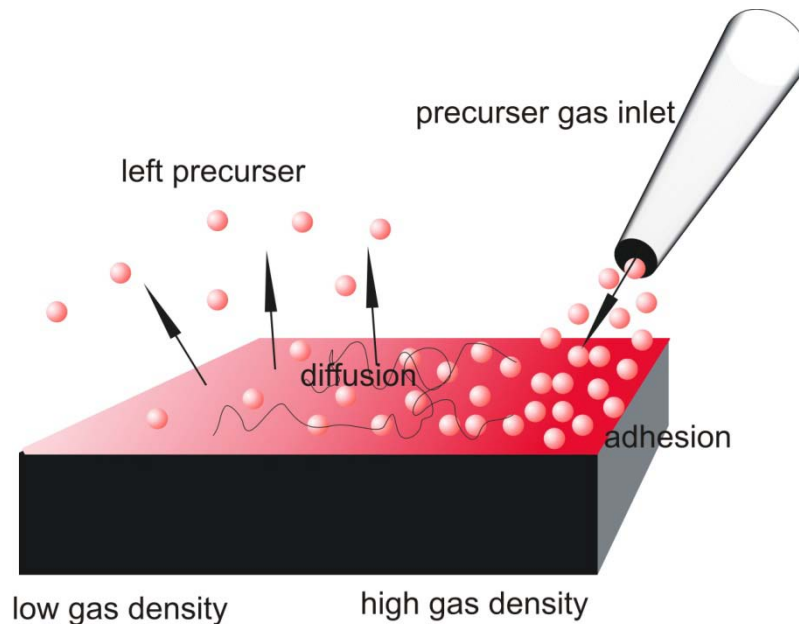


Figure 1-29: Schematic demonstration of the diffusion of the injected precursor gas on the surface of a specimen. The image shows only a virtual cutout, as it has to be expanded to a rotational symmetry around the injection nozzle.

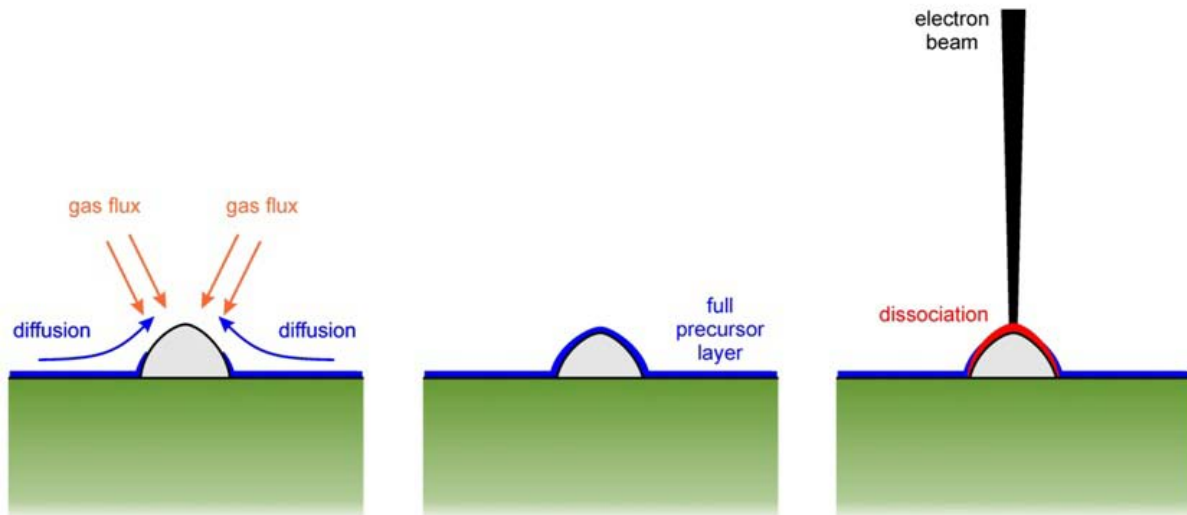


Figure 1-30: Three images showing how a covering with precursor gas functions with a small increase. By diffusion the surface including the small increase the specimen gets completely covered. This is shown in the middle image. In the last image the electron beam interact with the precursor gas and dissociate it so that a metal layer is deposited. [12]

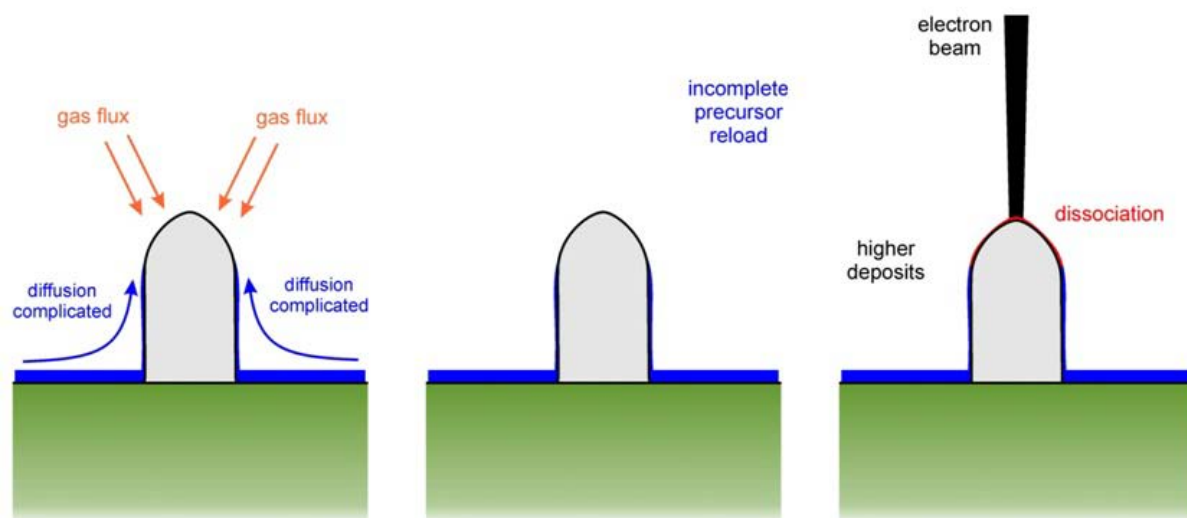


Figure 1-31: Three images showing how a covering with precursor gas functions with a high increase. By diffusion the surface, including the high increase, the specimen gets incompletely covered. This is shown in the middle image. In the last image the electron beam interact with the less precursor gas and dissociate it so that a thin metal layer is deposited. [12]

Furthermore one can calculate a distribution of impinging of the precursor gas on the specimen surface to get information of how large this gas distribution will be and how much gas is needed to cover the specimen, which is demonstrated in Figure 1-32. This depends on the angle α , the height H and the distance d . In this simulation the parameters for the tube inclination was 60° and for the inner tube diameter 0.5mm. [19]

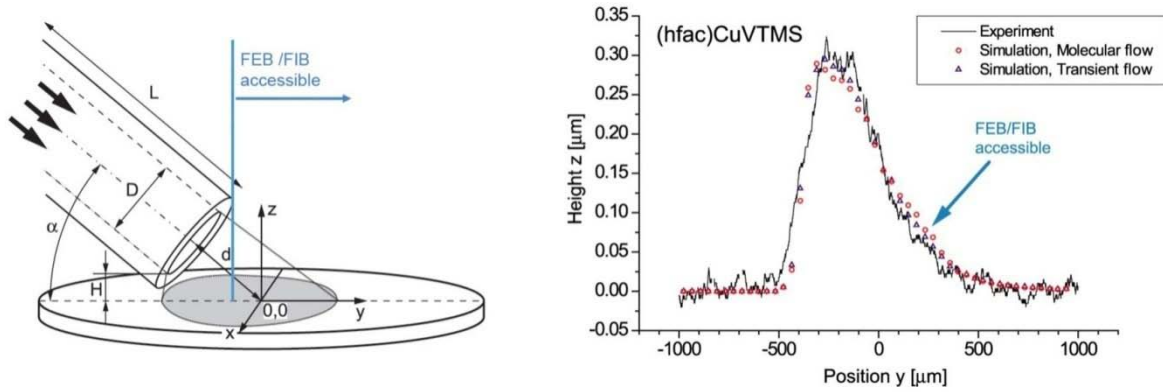


Figure 1-32: On the left image the geometric dimension from the gas needle and the surface is shown. In the right image the flux distribution is shown. They are formed with two simulation models and once done experimentally by measuring with a stagnation tube. [19]

1.2.3 Deposition basics and growth characteristics

A deposition area is the area in which the electron beam moves. Beam moving is not continuous but a discrete movement called pulsed deposition. The beam holds on one position and after a certain defined dwell time, which corresponds to the beam exposure time per pixel, it moves to next position. Such a typical scanning array for a serpentine patterning strategy is shown in Figure 1-33. The scanning time for one full frame is called the loop time. The refresh time is the loop time plus an eventual pause time. If the pause time is zero, the refresh time will be equal to the loop time. The pause time is the time when the beam is blanked. After the refresh time, the patterning will start from the beginning with scanning point one. Such a repetition is called a pass or a layer. How often this will be repeated depends on the intended height of the deposition which defines further the total exposure time in terms of the overall time; and the total exposure time per point is defined as the sum of deposition pulses for each single point.

1	2	3	4	5
6	7	8	9	10
11	12	13	14	15
16	17	18	19	20
21	22	23	24	25

Figure 1-33: This image shows the moving of the electron beam. The beam scans from field 1 to 25.

As the deposition starts with each layer, more and more material will be deposited. However, all of the layers will not have the same growth in height. The reason for this is the precursor

coverage difference which depends on the deposition. If the gas is first to start and the deposition starts later, the surface is completely covered due to saturation. In this case it will result in a high growth rate. Since the precursor is depleted after a beam pulse it has to be replenished, depending on the refresh time and also on morphological peculiarities as shown in Figure 1-31. If the replenishment is not completed before the subsequent pulse starts, the growth rate decays.

1.2.4 Advanced patterning (EBID max smooth)

By changing the deposition parameters it is possible to change both the growth rate as well as the platinum-carbon ratio. A maximized volume growth rate is of great advantage when a high throughput is needed such as TEM lamella preparation where ion assisted deposition is not of advantage (high thermal stress, ion implantation, sputtering effects).

The pattern “EBID max smooth” is an in-house development to push the deposition efficiency towards its intrinsic limit by tuning the individual process parameters. It has a growth time which is much higher (about 2.5 times) than the standard adjustments. Figure 2-2 shows the Volume Growth rate from standard EBID and standard IBID deposition in relation to the EBID max smooth.

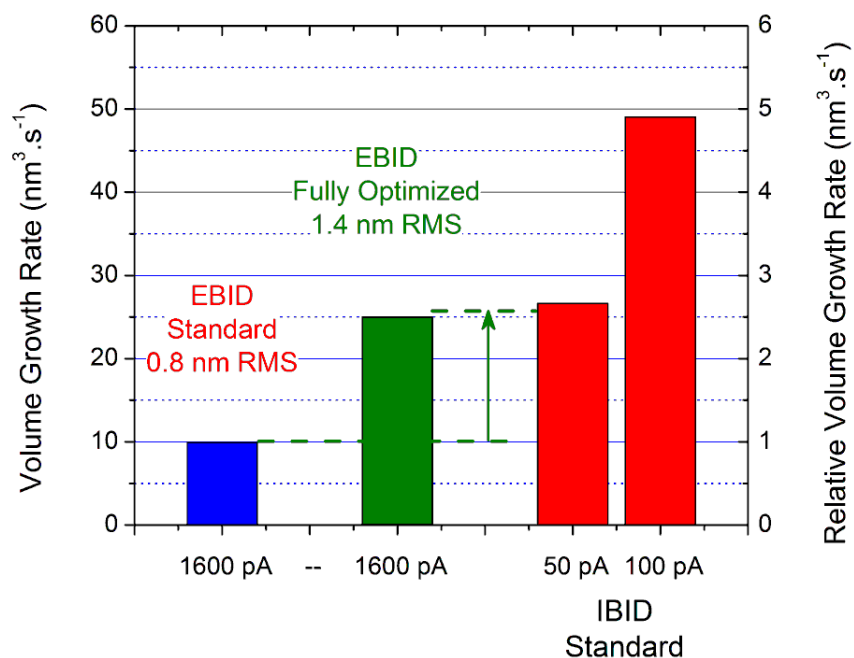


Figure 1-34: This diagram shows the efficiency of the EBID max smooth. One can see that the Volume Growth rate is in the range of a IBIB standard deposition.[12]

2 Chapter 1: Characterization of EBID Max Smooth Growth Characteristics

This part of the thesis will focus on some aspects of the in-house developed “EBID max smooth” pattern in a Nova 200 Dual Beam system as already introduced in chapter 1.2.4. The experiments were carried out to validate the high performance of such a deposition by showing the dependence of the deposition growth, on size, geometric form and the total growth time of the deposition. Primarily, deposition behavior was investigated for different loop times, depending on the pattern size. After this, the influence of the geometric form was examined, and that was followed by checking the deposition behavior for the same size but for different passes, which defines the height of the deposited material. Consequently, the results were evaluated for discussion with the aim to confirm a high efficiency for EBID max smooth and the independency on many patterning parameters making this pattern an universal pattern.

2.1 Experimental

2.1.1 Substrate

The sample chosen for this experimental work was highly oriented pyrolytic graphite (HOPG) with a size of approx. 1×1 cm, which was used as the substrate for deposition experiments. The surface of the sample was cleaved with an adhesive tape, bounding on the surface and then being removed. This method generates a new, clean surface by cleaving the crystal along the cleavage planes by sticking the old surface onto the adhesive tape. This procedure was repeated for five times. Owing to the separable layers graphite material has, this method was easy to apply. One other advantage of HOPG was forming considerably low surface contamination when subjected to electrons in the SEM.

2.1.2 Deposition

Prior to deposition experiments, one problem occurred when the cleaved surface had no features for focusing and optimizing the electron beam, which is needed for the best quality of the deposition process. On the specimen surface, the regions with features are often helpful

for sharpening the beam, and further patterning is usually carried out near to this sharpening fields. The patterns arranged for the experimental series are shown in a schema in Figure 2-1. The drift-compensation-field is used for stabilizing the charge related drift. The related deposition times were chosen between 10 and 15 minutes to ensure an charge equilibrium of the specimen for a beam energy and a beam current of 5 keV and 1600 pA, respectively. If the field is not implemented, the drift in the first deposition field is high because of the long waiting times before the deposition starts, the specimen is not charged by the electrons and will drift until a charge balance is reached.

With the control-field it is possible to normalize the measured data. The control-field always has identical data if the working conditions of FIB are precisely the same. If not, one can calculate the value for the normalization. There are several reasons for the variation in the deposition rate. It highly depends on the exact distance between the GIS needle and the specimen (compare 1.2.2), the surface contamination of the specimen, the state of the precursor crucible (operating time) and on the adjustments of the electron beam. The remaining fields are depositions 1 to 12. For a statistical work, a set of three fields were build with the identical data , in order to get an overview of how random the growth rate will be when same conditions are used.

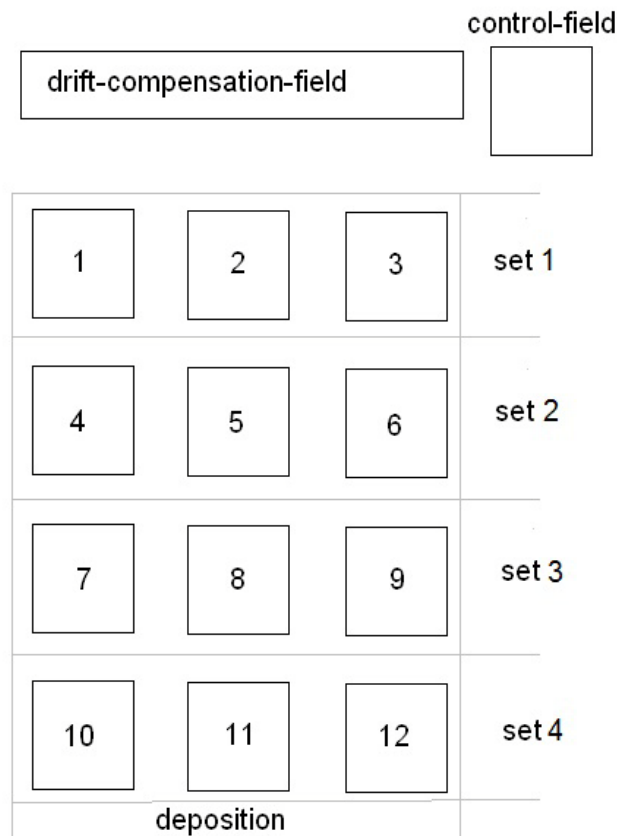


Figure 2-1: Schema of a pattern design.

Table 2-1: List of pattern which were made for the analysis.

Name	control field		deposition 1-3			deposition 4-6		
	passes []	loop time [ms]	passes []	loop time [ms]	size [um]	passes []	loop time [ms]	size [um]
M S Pattern 1_1			25000	5.3	2.5x2.5	25000	15.2	4.3x4.3
M S Pattern 2_2	25000	15.3	25000	34.8	6.6x6.6	25000	39.7	7x7
M S Pattern 4_1	25000	15.3	25000		3.3x3.3	25000		1x10
M S Pattern 5_1			7000	5.3	2.5x2.5	25000	5.3	2.5x2.5
M S Pattern 6_1			7000	25	5.6x5.6	25000	25	5.6x5.6
M S Pattern 7_1			7000	51.8	8x8	25000	51.8	8x8
M S Pattern 8_1	25000	15.3	25000	50.4	8x8	25000	34.8	6.6x6.6
M S Pattern 9_1	25000	15.3	25000	5.3	2.5x2.5	25000	20.3	5x5
M S Pattern 10_1	25000	15.3	25000	20.3	5x5	25000	20.3	5x5
M S Pattern 11_1	25000	15.3	25000	20.3	5x5	25000	20.3	5x5
M S Pattern 12_1	25000	15.3	25000	3 depositions with 5, 8, 11,14, 17, 20, 25, 35, 50 ms				
M S Pattern 12_2	25000	15.3	25000	3 depositions with 5, 8, 11,14, 17, 20, 25, 35, 50 ms				
M S Pattern 12_3	25000	15.3	25000	3 depositions with 5, 8, 11,14, 17, 20, 25, 35, 50 ms				
M S Pattern 13_1	not used							
M S Pattern 14_1	25000	15.3	25000	20.3	5x5	25000	20.3	5x5
M S Pattern 15_1	25000	15.3	25000	25 depositions with 20 ms; size 5x5 μs				
M S Pattern 16_1	25000	15.3	25000	25 depositions with 20 ms; size 5x5 μs				

Name	deposition 7-9			deposition 10-12			drift-compensation-	inverse
	passes []	loop time [ms]	size [um]	passes []	loop time [ms]	size [um]		
M S Pattern 1_1	25000	25	5.6x5.6				yes	
M S Pattern 2_2	25000	51.8	8x8				yes	
M S Pattern 4_1	25000		10x1				yes	
M S Pattern 5_1	40000	5.3	2.5x2.5				yes	
M S Pattern 6_1	40000	25	5.6x5.6				yes	
M S Pattern 7_1	40000	51.8	8x8				yes	
M S Pattern 8_1	25000	20.3	5x5	25000	5.3	2.5x2.5	yes	
M S Pattern 9_1	25000	34.8	6.6x6.6	25000	50.4	8x8	yes	yes
M S Pattern 10_1	25000	20.3	5x5				yes	
M S Pattern 11_1	25000	20.3	5x5				yes	
M S Pattern 12_1							yes	
M S Pattern 12_2							yes	
M S Pattern 12_3							yes	yes
M S Pattern 13_1							yes	
M S Pattern 14_1							yes	yes
M S Pattern 15_1							yes	
M S Pattern 16_1							yes	yes

2.1.3 Analysis via FIB/SEM

The pattern of the deposition series was applied using the parameters shown in Table 2-2. Before starting the deposition process, the gas of the injection needle was well heated and the gas outlet was opened for approximately 15 minutes in advance, so that the gas had enough time to cover the sample in a stable environment and that the whole system comes into a thermodynamical equilibrium between precursor adsorption and desorption. After that time, the patterning was started and after a time of one to five hours the pattern was finished and

automatically terminated. To avoid unwanted additional deposition due to residual precursor on the sample surface a waiting time of min. 15 minutes was introduced before the electron was used for inspection. This time is needed to be safe that the most Pt-precursor is desorbed from the surface. These are small round deposition or a contamination on the whole electron scan area. These waiting times were adhered in the whole experiment. In Figure 2-2 the sharpening-field and the first patterns are shown.

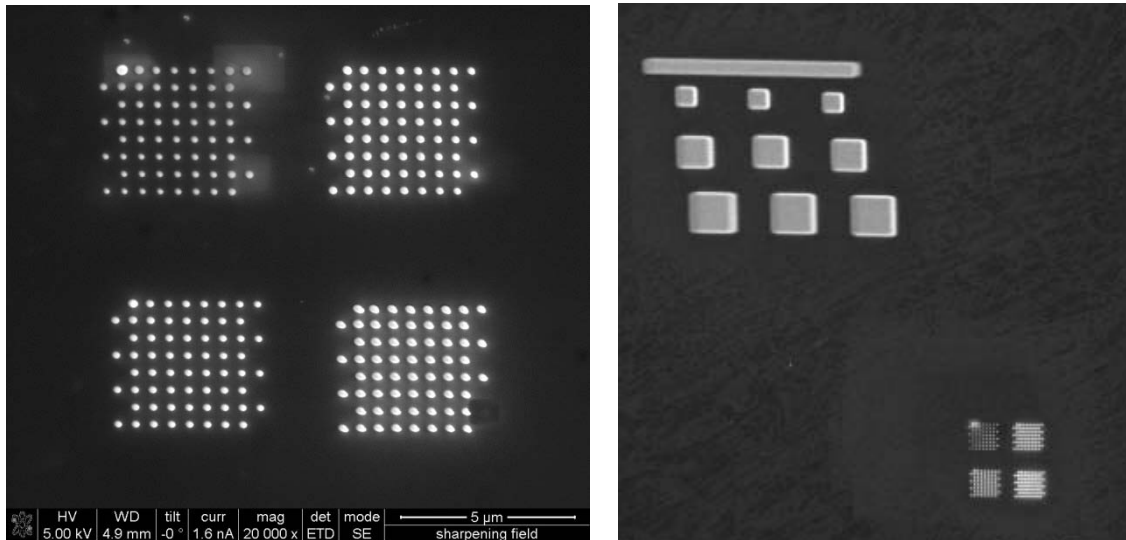


Figure 2-2: The left image shows the sharpening field and the right picture shows the sharpening-field in the bottom-right corner. In the center is the uncut “M S Pattern 1_1” directly after the deposition, with the beam adjustments from the deposition.

Table 2-2: Primary SEM adjustments, which were used in this experiment.

category	parameter	value	note
general	application file	EBID max smooth	in house investigated application file
	voltage	5 kV	
Electron deposition	current	1,6 nA	voltage and current for a high growth rate
	voltage	5 kV	
Electron beam imaging	current	0,4 nA	low voltage for a small spot (lateral resolution) and good surface detail
	Tilt	52°	low current for a high lateral resolution with a reasonable signal to noise ratio
	Detector	in lens	to see the surface from the ion cut, so that it is possible to measure it
			Mode 2 with in-lens-Detector to get best resolution

Ion-beam-milling was used for the analysis of the height of the deposited structures. The stage was tilted to 52° so that the ion beam would stand perpendicular to the sample surface while the electron beam allowed characterizing the cross section. This tilt is sketched in Figure 2-3. To obtain a fast and precise ion milling with less heat damage and a sharp edge, the milling was split in coarse and fine milling steps. The adjustments for these are shown in

Table 2-3 under “Ion-milling”. While positioning the pattern for the coarse-milling step, no ion image was acquired in order not to harm the deposited structures. With the fine-milling, one single image using the shortest scan time was made to find the exact position of the coarse-milling. Figure 2-4 shows the deposited structures before and after the ion-milling.

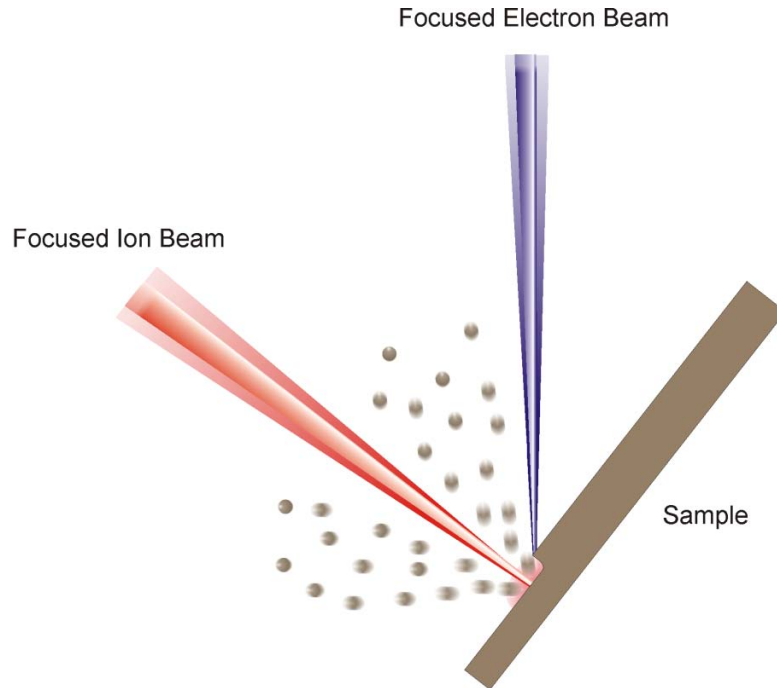


Figure 2-3: The 52° tilted sample with ion beam perpendicular on it.

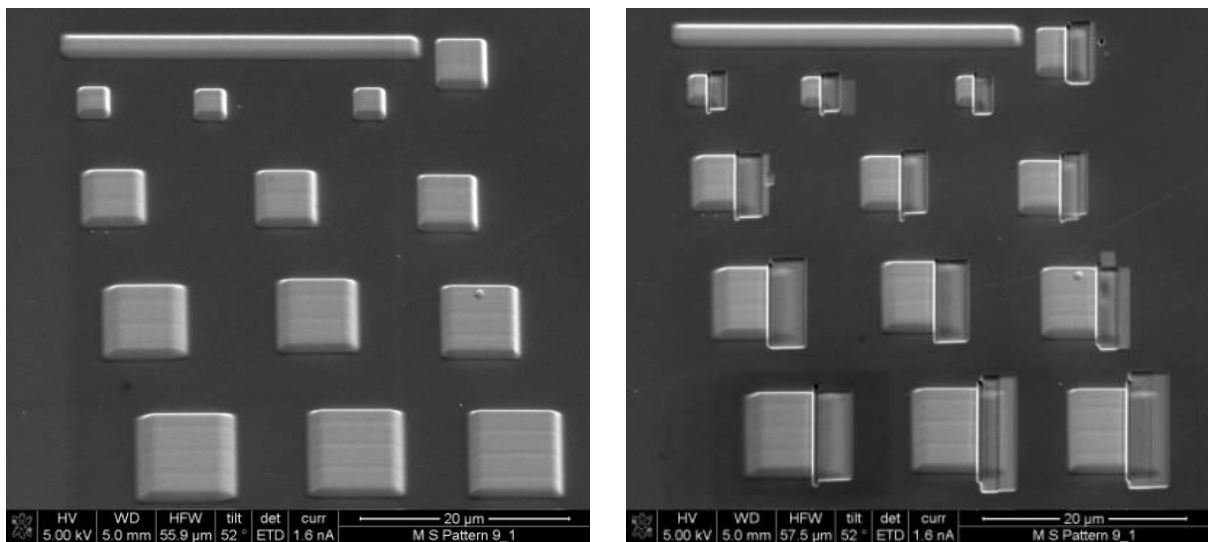


Figure 2-4: Left image shows the “M S Pattern 9_1” arrays fabricated for ion-milling, while the right image shows the structures after milling.

Table 2-3: Primary ion-milling parameters used for the corresponding experimental study.

category	parameter	value	note
general	application file	Si	Standard application file
	pitch		70,5 nm
	dwell time		1 μ s
Ion-milling (coarse milling)	voltage	30 kV	
	current	500 nA	high current to perform a fast and coarse milling
Ion-milling (fine milling)	voltage	30 kV	
	current	30 pA	low current to perform a precise milling for a good cut edge with adequate time cost

2.1.4 Data acquisition

The height measurements from the cross-sections of the deposited structures were performed at 52° stage tilt while dynamic focus and tilt correction options were activated. Dynamic focus feature in dual beam instruments is often used for the tilted surfaces, to have the correct focus at the top and the bottom at the same time. If dynamic focus is not active, the image is only focused at a small column of scan lines and the rest remains unfocused. The tilt correction stretches the picture in the way that the tilt for the electron beam is corrected. If this is not active, one would see a rectangle with different height and width instead of a square. Imaging adjustments are presented in Table 2-2 under “Electron beam imaging”. The depth measurements were carried out using the measurement tool at the FIB software. A typical image for that is shown in Figure 2-5. To minimize the measuring inaccuracy, five values for depths were obtained from each cross section. The measurements were done at a magnified cross-section like shown in Figure 2-6.

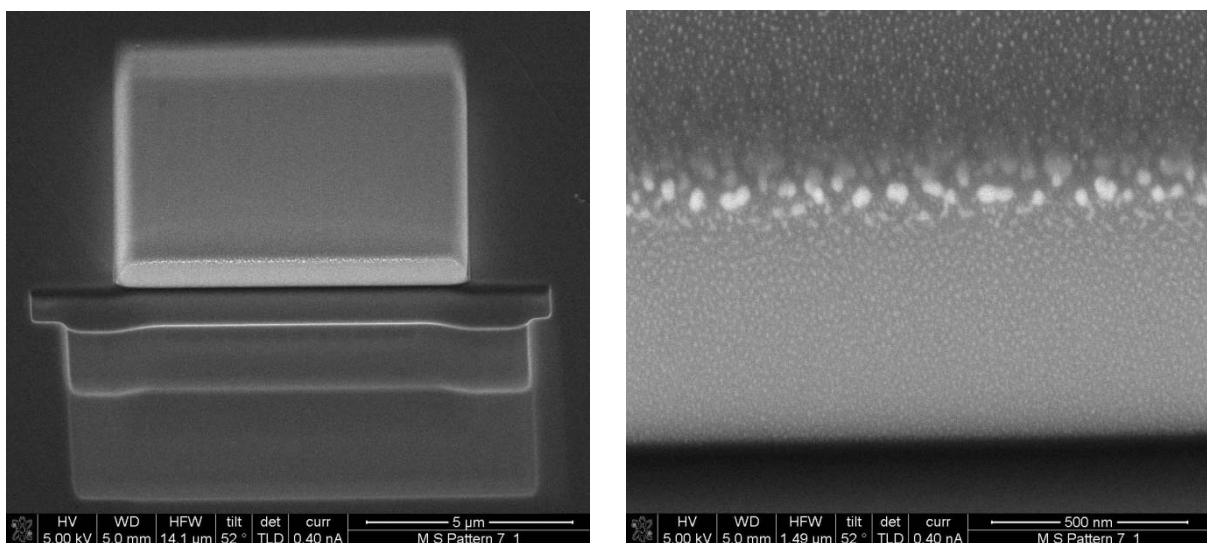


Figure 2-5: Left image showing M S Pattern 7_1 deposition 9. On the right image, a magnified section of the edge on which the measurements was done is shown.

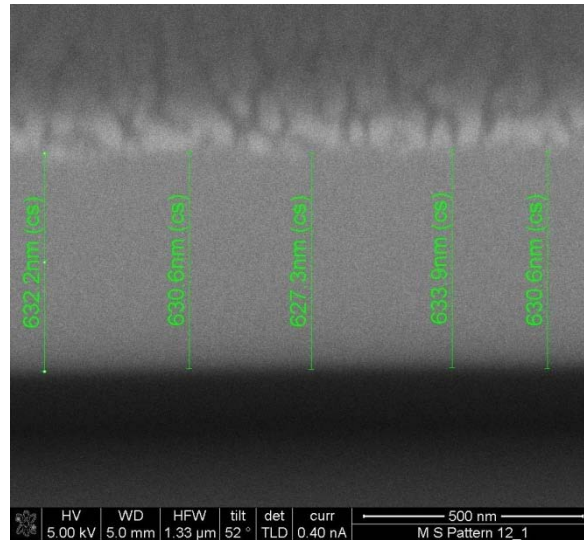


Figure 2-6: This magnified section from pattern 12_1 deposition 5, showing the height measurements.

2.2 Results and discussion

The results from height measurements obtained from the deposited structures which are presented in Table 2-1 can be evaluated as follows: the patterning position can be directly correlated to the effectivity of deposition rate (see chapter 2.2.1), and therefore the deposition growth rate in relation to the position of patterning can be optimized and recalculated. Furthermore, the deposition rate was investigated with “Investigation of the temporal height evolution via AFM” in the case of using different passes. The influence of different geometric forms like square or rectangles with the “Dependence on the geometric footprint” was also examined, while. At least the influence of small and large forms and the effects of their loop times were investigated.

2.2.1 Influence of the patterning position

The influence of the deposition position cannot be disregarded. Four different patterning series (“M S Pattern 10_1”, “M S Pattern 14_1”, “M S Pattern 15_1” and “M S Pattern 16_1”; two series with nine structures and two series with 25 structures) with identical deposition parameters used for each individual pattern were fabricated. The height analysis allowed for a 2D plot, revealing the relative deviation in dependence on the X-Y position. Furthermore, in order to exclude the influence of the patterning sequence, two patterns were deposited top-down, while two patterns bottom-up. Figure 2-7 demonstrates the corresponding images.

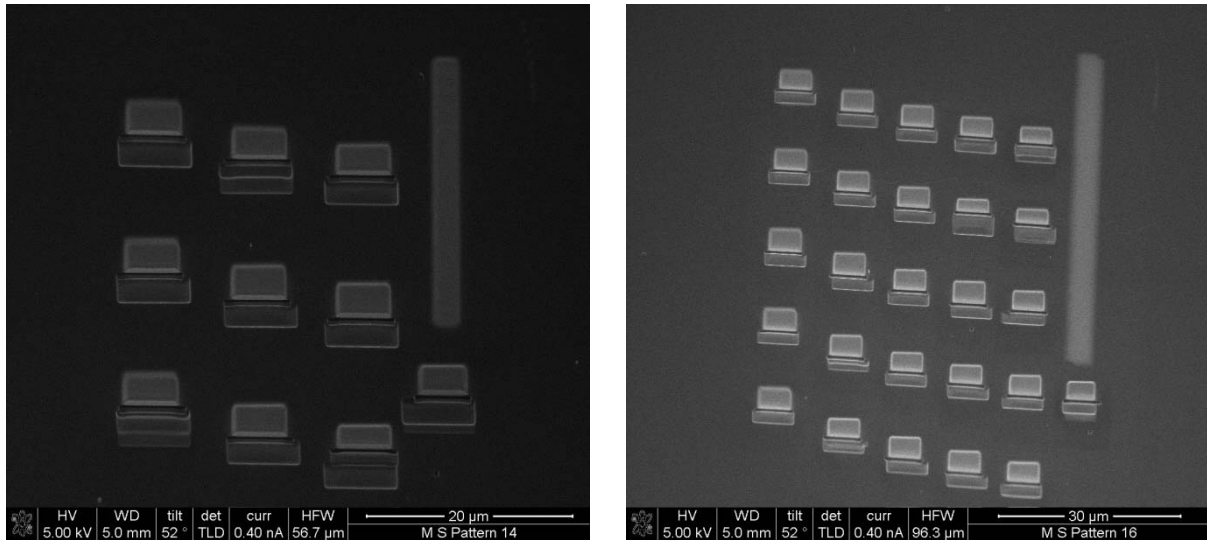


Figure 2-7: This two images plus two, which looks the same and are not mapped, showing the patterns which were used to gather the data to find the influence of the deposition position.

The data gathered were then normalized to values in percentage and averaged. Curve fitting was done using MATLAB.

In the first plot (shown in Figure 2-8) the non fitted points are shown with a linear interpolation. A trend is visible but this fit is only useful to see the original points.

With a polynomial fit of third order (shown in Figure 2-9) the tendency appears to be more obvious but the slightly wavy tendency is not very likely to be a real feature. The collected data have a variation and hence an exact fit is inaccurate. Furthermore the platinum nozzle is not likely to form such a plane.

A polynomial fit of first order forms a linear interpolation, bringing out a plausible plane for the corresponding data variations. This plane is shown in Figure 2-10.

In y-direction only a minimal deviation was observed, while in x-direction it was found to be around 0.2% per μm . Because of the small y-dependency, the plane was considered as one dimensional linear curve:

$$F = \text{const.} + 0.001919 * x \quad (2-1)$$

Where F is the percentile effectivity and x is the distance from the center-cross along x-axis in micrometers. An exact determination is due to the height variations (low data sets) and measurement errors not useful.

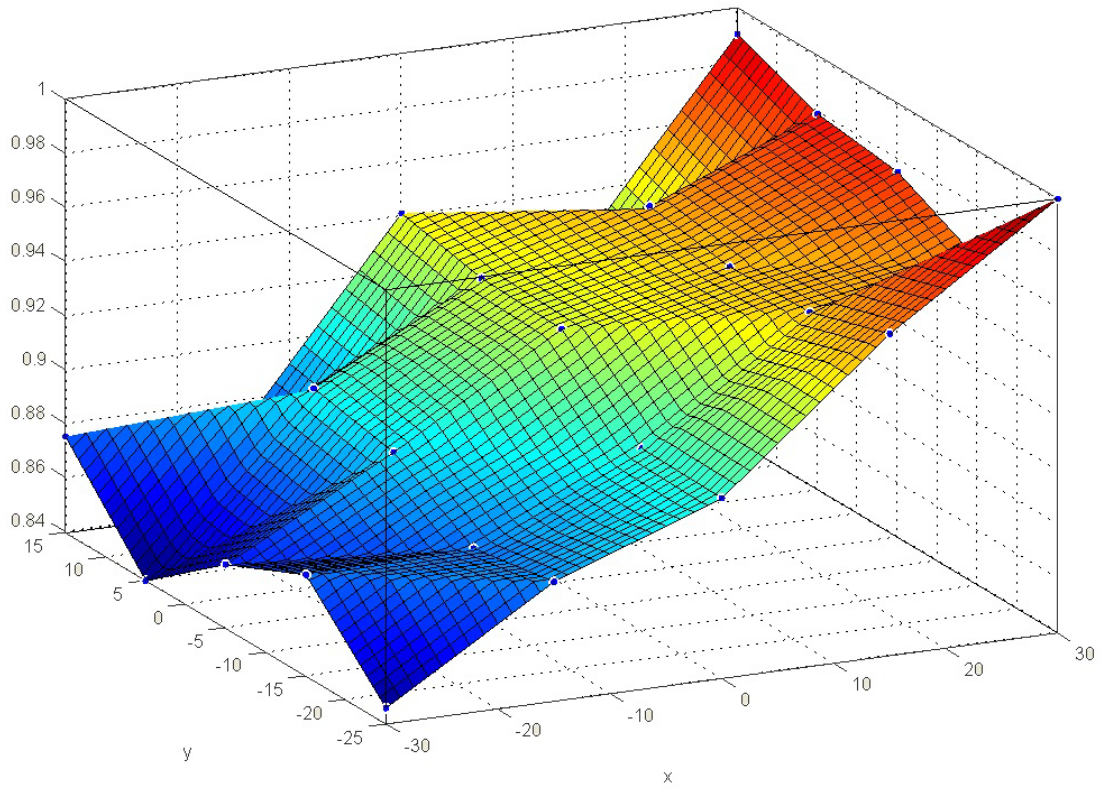


Figure 2-8: Linear interpolated Dataset. In x-direction the x-position and in y-direction the y position is shown. In Z- direction the normalized to a perceptual value is plotted.

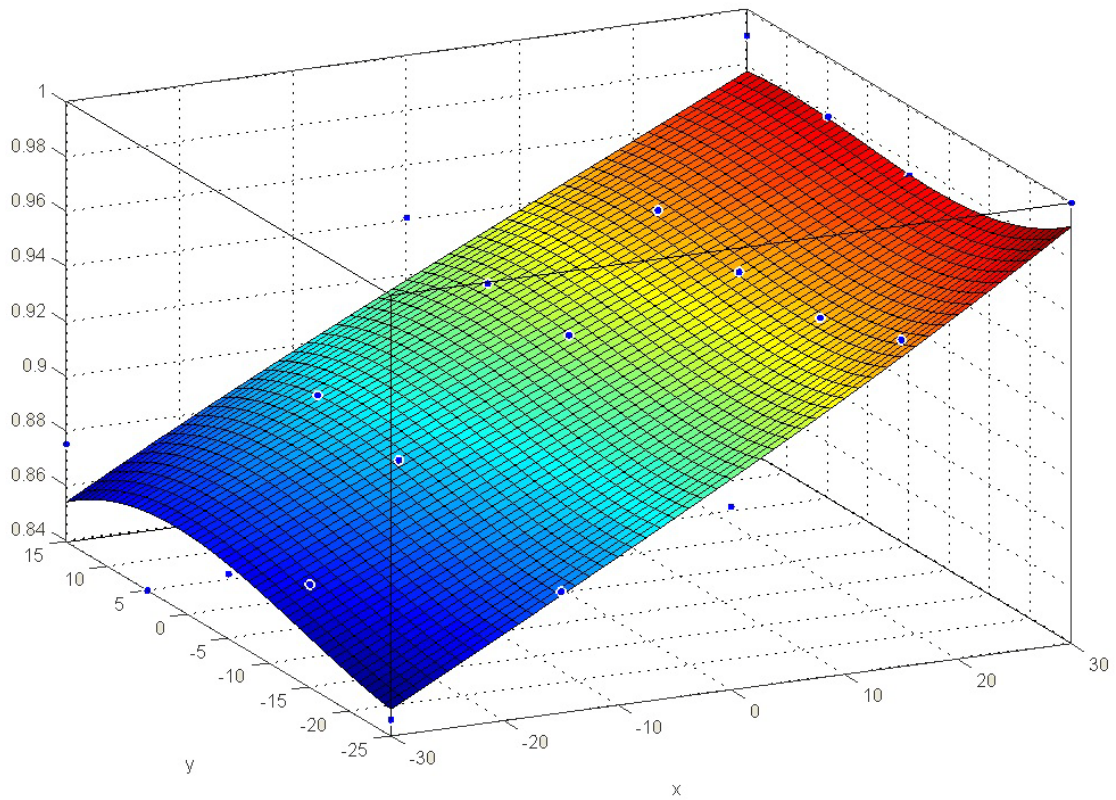


Figure 2-9: Polynomial fit of third order of the dataset.

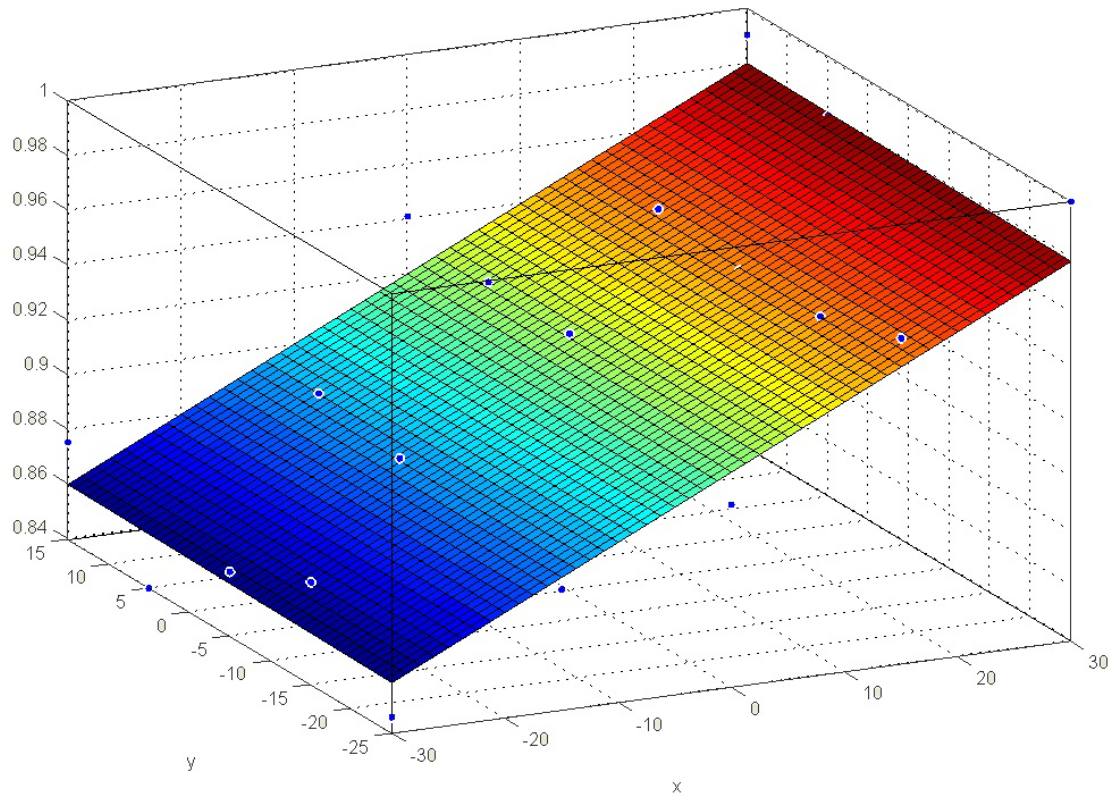


Figure 2-10: Polynomial fit of first order of the Dataset.

The reason for the deviation of 0.2% per μm in the patterning position is because the platinum gas flowing from the GIS needle has a certain angle and a differential distance to the sample surface. As a result, the Platinum gas covers the sample surface not homogenously (see chapter 1.2.2 and Figure 2-11).

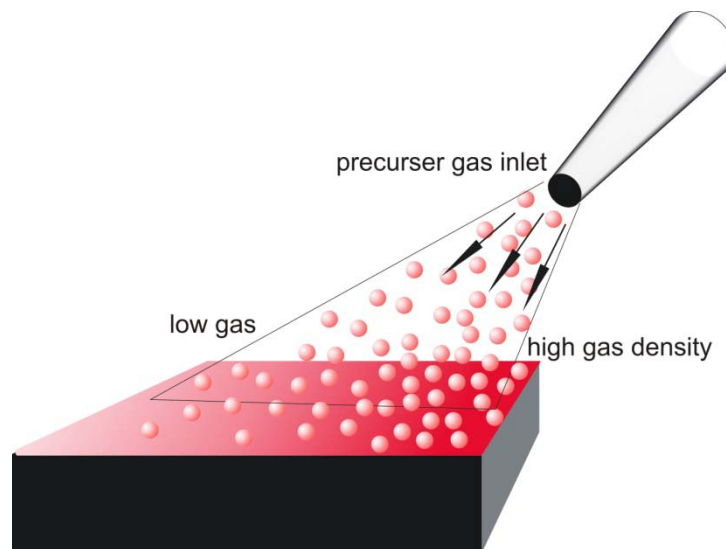


Figure 2-11: Flow of the platinum gas from GIS. Red spheres represent the platinum-gas. The right side on the specimen has a higher gas flow and therefore a higher deposition rate compared to the left side..

Table 2-4: Data for the temporal height measurements.

loops	pad height (corrected) [μm]	total time [s]	growth rate [$\mu\text{m}^3/\text{s}$]
16	1,4	0,0512	112,7
32	2,1	0,1024	83,7
64	3,4	0,2048	67,1
125	6,2	0,4	62,0
250	10,8	0,8	54,1
500	19,7	1,6	49,2
1000	36,1	3,2	45,1
2000	70,3	6,4	43,9
4000	140,1	12,8	43,8
8000	257,0	25,6	40,2
16000	480,8	51,2	37,6
32000	870,0	102,4	34,0

2.2.2 Investigation of the temporal height evolution via AFM

In order to gain further and deeper knowledge on the growth rate, an experimental analysis was carried out using the data from the layers, which were deposited by selecting twelve different loops of 16 to 32000. Each pattern had a size of 2x2 resulting in a loop time of 3.2 ms. Due to the high accuracy of AFM data, reliable results with less measurement errors were obtained. The corresponding results are given in Table 2-4. Figure 2-12 shows the growth rate, which is plotted by the red curve. It can be observed that the growth rate is very high for the initial loops, in particular after the first hundred loops getting more stable. However, it drops very fast with an increase of the loops, finally reaching to a constant value. As the higher number of the loops, the more deposition time needed, the drift would be a substantial problem for the long-time processing and therefore using very high number of loops for this experimental work was avoided. The reason for the varying volume growth rate has to sources: the main effect is caused by the fact that the interaction volume is much deeper inside the volume due to the chemical nature of the substrate. If the deposit grows the interaction volumes moves from the substrate into the Pt / C deposit. Different amount of potentially dissociating electron species influence the deposition behavior which is getting more constant after the entire interaction volume is within the deposit.

The second part of the variation is related to precursor diffusion dynamics on the surface: at initial states (no e^- beam) the surface has enough time to be covered with precursor gas. If the beam gets turned on, it will crack the platinum precursor gas and the first layers of platinum will be deposited. During further dissociation the precursor gas should diffuse over the deposited layers. A higher deposition is more complicated to replenish for the gas because it

must diffusion on top of the deposit. Hence, fewer gas can diffusion to the top of the deposition and so the platinum gas density is smaller as at the first loops. The black curve in Figure 2-12 shows the pad height.

As a conclusion, it can be suggested that the former layers of the deposited structure has a higher growth rate than the latter due to chemical differences between substrate and deposit as well as due to precursor diffusion dynamics. Once an equilibrium is reached the volume growth rate is widely constant and only geometry dependent (more complicated surface diffusion).

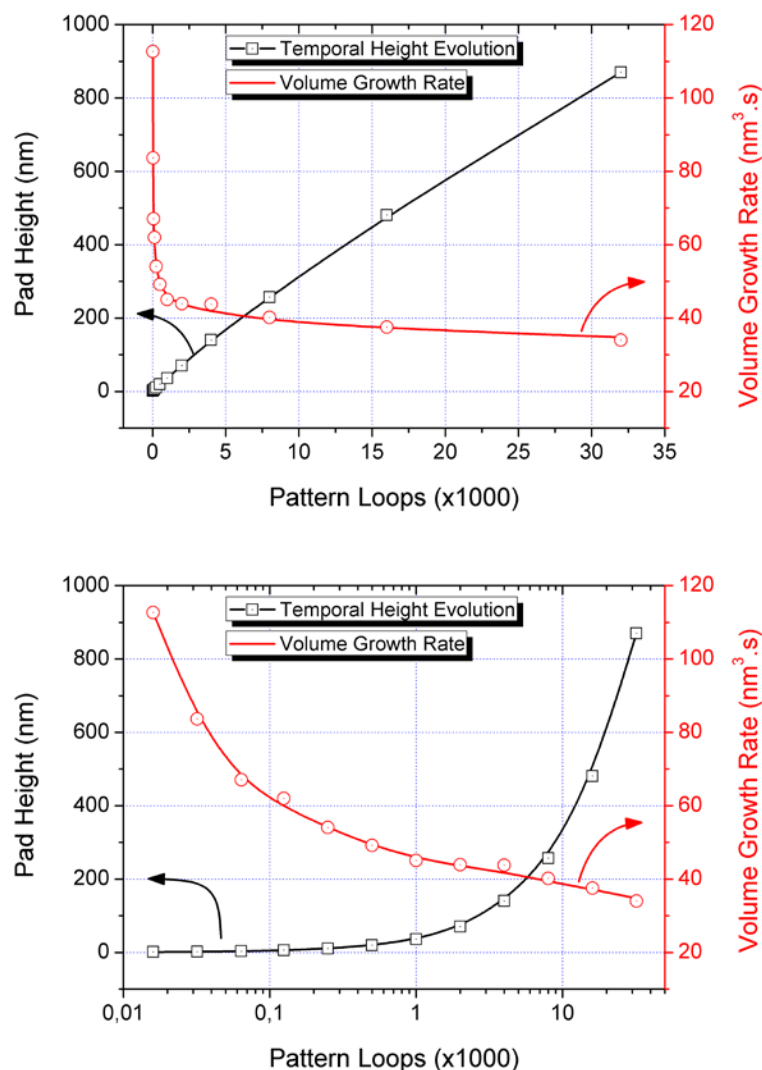


Figure 2-12: The diagrams show the temporal height evolution vs. the frame loops. The black curve indicates the height development (black curve and Y axis) while the red curve represents the volume growth rate (red curve and axis). While the bottom graph is shown with linear scales to show how fast a saturating tendency is achieved the bottom graph is shown with a linear time scale (loops) to allow for a more detailed insight in the temporal evolution.

2.2.3 Dependence on the geometric footprint

By using the patterning series “M S Pattern 4_1” (Figure 2-13), the dependency on the geometric footprint form was investigated by varying the X/Y ratios while the absolute area was kept identical at $10 \mu\text{m}^2$. The average of three sets is normalized by the normalization field and the result is shown Figure 2-14. As it can be seen an X/Y aspect ratio of 1 yield highest efficiency while ratios of 0.1 and 10 show lower rates. The basic reason for the difference is the ratio itself which complicates the diffusion on top of the structures due to a higher probability for the precursor molecules to go down again instead of staying on the topmost areas. The difference between ratios 0.1 and 10 is found to be around 3 % and originates most likely from the patterning sequences as shown in the next chapter.

As a result it can be concluded that there is a weak dependency of the geometric footprint in the range of about 5% for strong variations originating from changed diffusion conditions for the gas molecules. Considering the used variation and the total change in volume growth rates, however, it can be considered as a weak dependency.

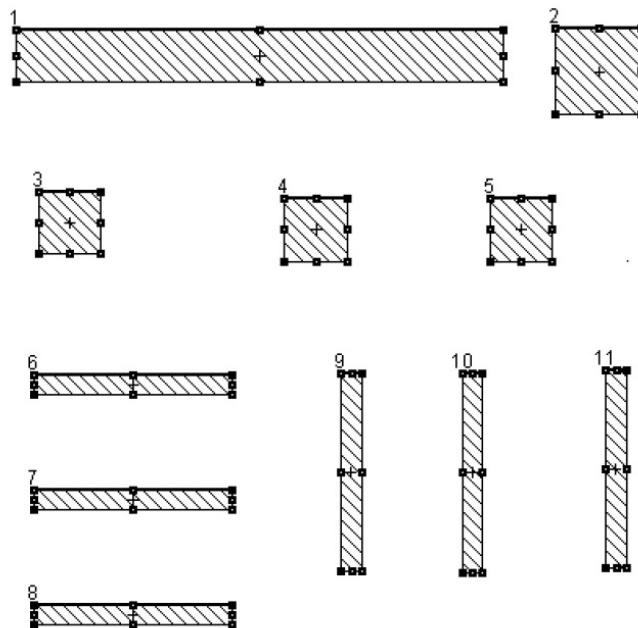


Figure 2-13: Depositions of "M S Pattern 4_1".

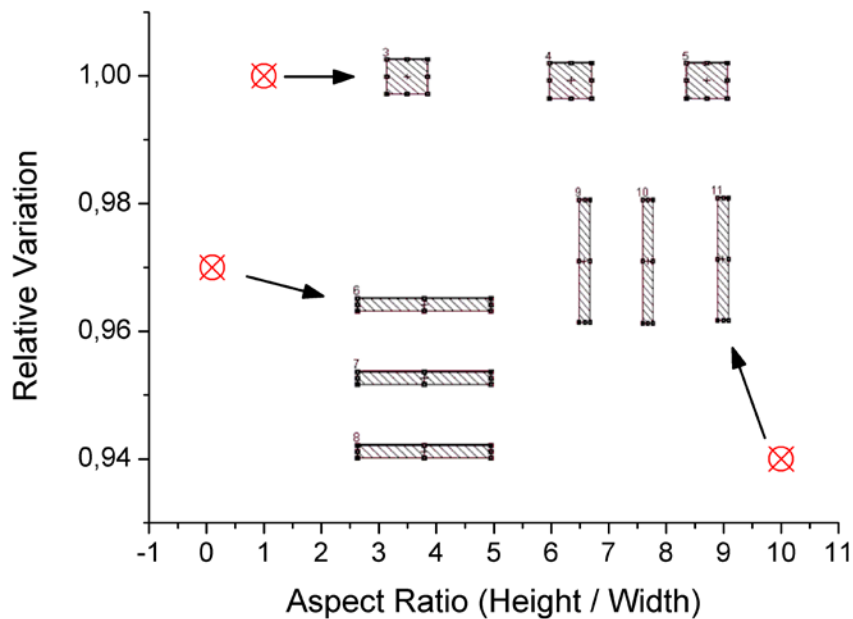


Figure 2-14: Diagram of the measurement result from „M S Pattern 4_1“.

2.2.4 Dependency on refresh times

To investigate the grow rate dependence on the refresh time (realized by loop time variation), a huge number of patterns has been grown and analyses. First patterning tests, however, revealed a strong variation since the experiments could not be performed in one single patch. Furthermore, it turned out that there is a dependency on the patterning sequence by means of short-to-long or long-to-short refresh times. Those first results are summarized in Figure 2-15 for the described variations.

To compensate for experimental variations another series was designed with less refresh time points (only 4 instead of 9). The first set was executed from short to long refresh times starting as shown by the red graph in Figure 2-16 revealing a clearly decreasing tendency of less than 3%. As a second step the patterning sequence was inverted and executed from long to short refresh times whose results are shown by the black graph in Figure 2-16 also revealing a variation of less than 3% but this time with an increasing character.

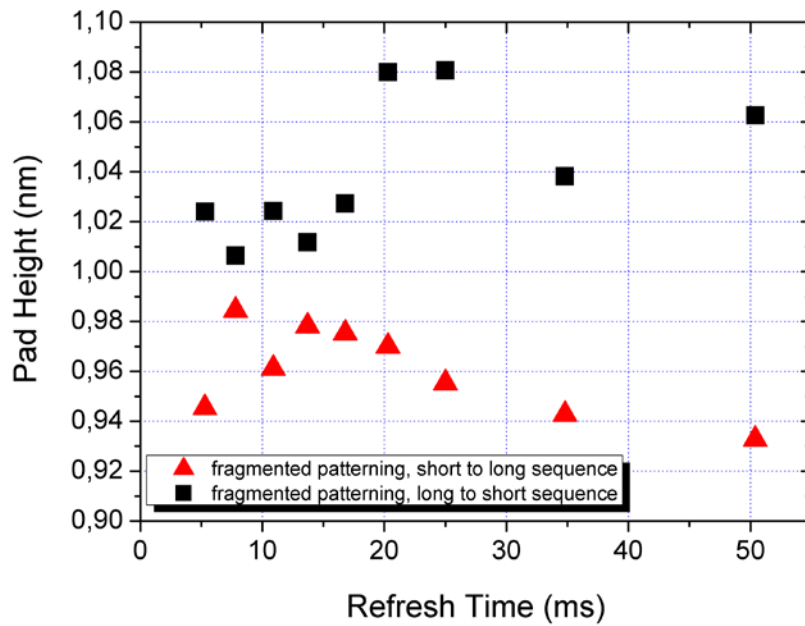


Figure 2-15: Data from MS pattern 12_1.

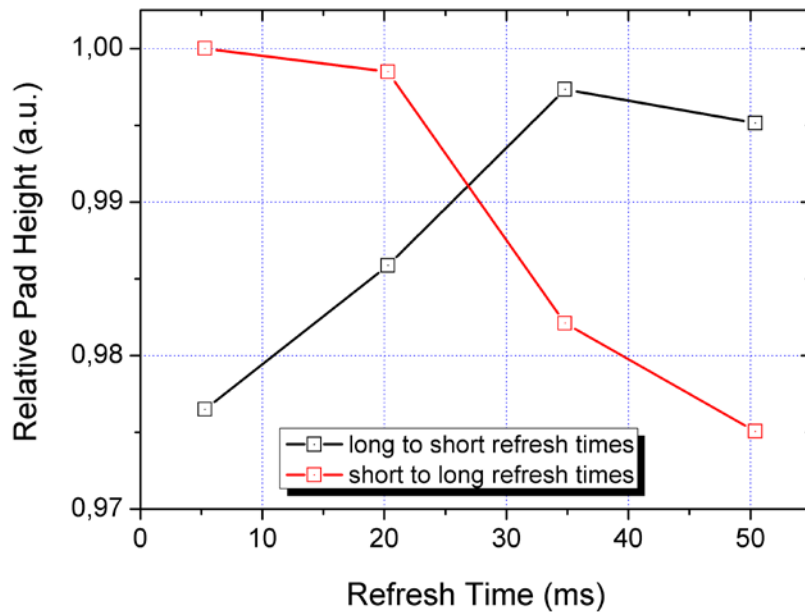


Figure 2-16: Data from MS pattern 8 and 9.

The estimated measurement error Figure 2-16 is approximately $\pm 1\%$ (meaning a real error of less than 7 nm) confirming that the observed variations cannot be neglected. A closer look, however, reveals the common link as the exposure time. While the black curve is executed from right to left, the red curve must be followed from left to right. In both cases a decreasing

tendency is observed after a first plateau. This leads to the conclusion that the overall coverage of precursor molecules gets depleted for such long patterns for such high currents.

The inverted character of the curves allows for another very important conclusion: the refresh time itself shows a very weak volume growth rate dependency of less than 3% for the huge range from 5 to more than 50 ms refresh time.

This indicates clearly that the local precursor coverage is barely influenced from the refresh time which suggests strongly a reaction rate limited regime for EBID max smooth.

This result can be seen as one of the major results in this thesis because it proves that the efficiency of the EBID max smooth pattern is extremely high due to the selective establishment of a reaction rate limited precursor regime.

2.3 Conclusion

In this part of the work, several experiments were carried out to check the growth rate of the platinum structures, which are deposited using EBID max smooth application. It has been found out that the geometry and the loop time have no significant influence on the growth rate. A relative growth rate comparison to the standard pattern is shown in Figure 2-17 where the red curve (triangles) is the standard pattern and the black (squares) one the investigated EBID max smooth pattern. The patterning position indeed had influence, although this was not dependent on the EBID max smooth application, but a general behavior. The temporal height evolution has an influence but will be also by each EBIDs, so this is a general case. The EBID max smooth is therefore widely independent on refresh times (loop times), size and footprint geometries. This suggests strongly that the EBID max smooth pattern is able to establish a reaction rate limited precursor regime due to adapted parameters which makes this pattern an universal patterning strategy for high efficiency depositions. The ultimate improvements are found around a factor 3 compared to default condition which is a significant step forward towards a more straightforward use for EBID processes.

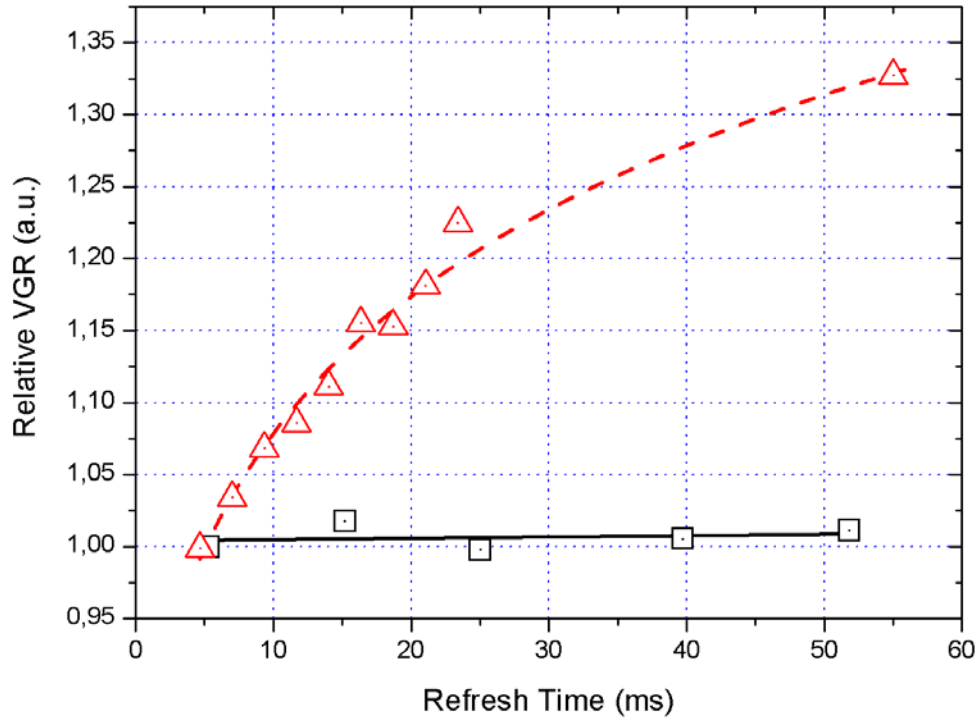


Figure 2-17: Relative growth rate comparison to the standard pattern and the EBID max smooth pattern.

3 Technical preparations

At an initial step of the current work, the data acquisition, including a current source was designed for the resistor measurements. More detailed information on the technical aspects will be given further in this chapter.

3.1 Four point resistor measurement

Electrical resistance can be measured with the two- or four-point method. A two point measurement drives a constant current through a resistor and with the measured voltage drop one can calculate the resistor. But the resistor is the sum of the real resistor plus transition resistor and lead resistors.

$$U = I \cdot R \quad (3-1)$$

U... **voltage drop [V]**

I... **current throw the resistor [A]**

R... **resistance throw resistor (including transition resistor and lead resistors) [Ω]**

Therefore only the four point is eligible for this problem because this method is more accurate through the independences of transition resistors and lead resistors. The principle is shown in Figure 3-1. The constant current source drives a constant current (I_T) through the current leads (R_{lead}). The current through the resistor (R_S) is:

$$I_S = I_T - I_{sense} \quad (3-2)$$

Where I_S is very small and with a good amplifier it will be in a range of some pA. If

$$I_{sense} \ll I_T \text{ and } I_{sense} \cdot R_{lead} \ll U_{R_S} \quad (3-3)$$

one could neglect it for the most cases.

The measured voltage is:

$$U_M = I_S \cdot R_S + I_{sense} \cdot 2 \cdot R_{lead} \quad (3-4)$$

With (7-3) one can simplify to:

$$U_M = U_S = I_S \cdot R_S \quad (3-5)$$

Hence the measurement is independent of the resistor in the voltage and current lead and also of transition resistors. If (7-3) is not satisfied the measured voltage U_M is smaller than the real voltage drop U_S . If this happens one has to calculate the real value by measuring the voltage over the constant current source, and under the assumption that all R_{leads} are the same and one has this also measured it is possible. But this will not take place in this master thesis.

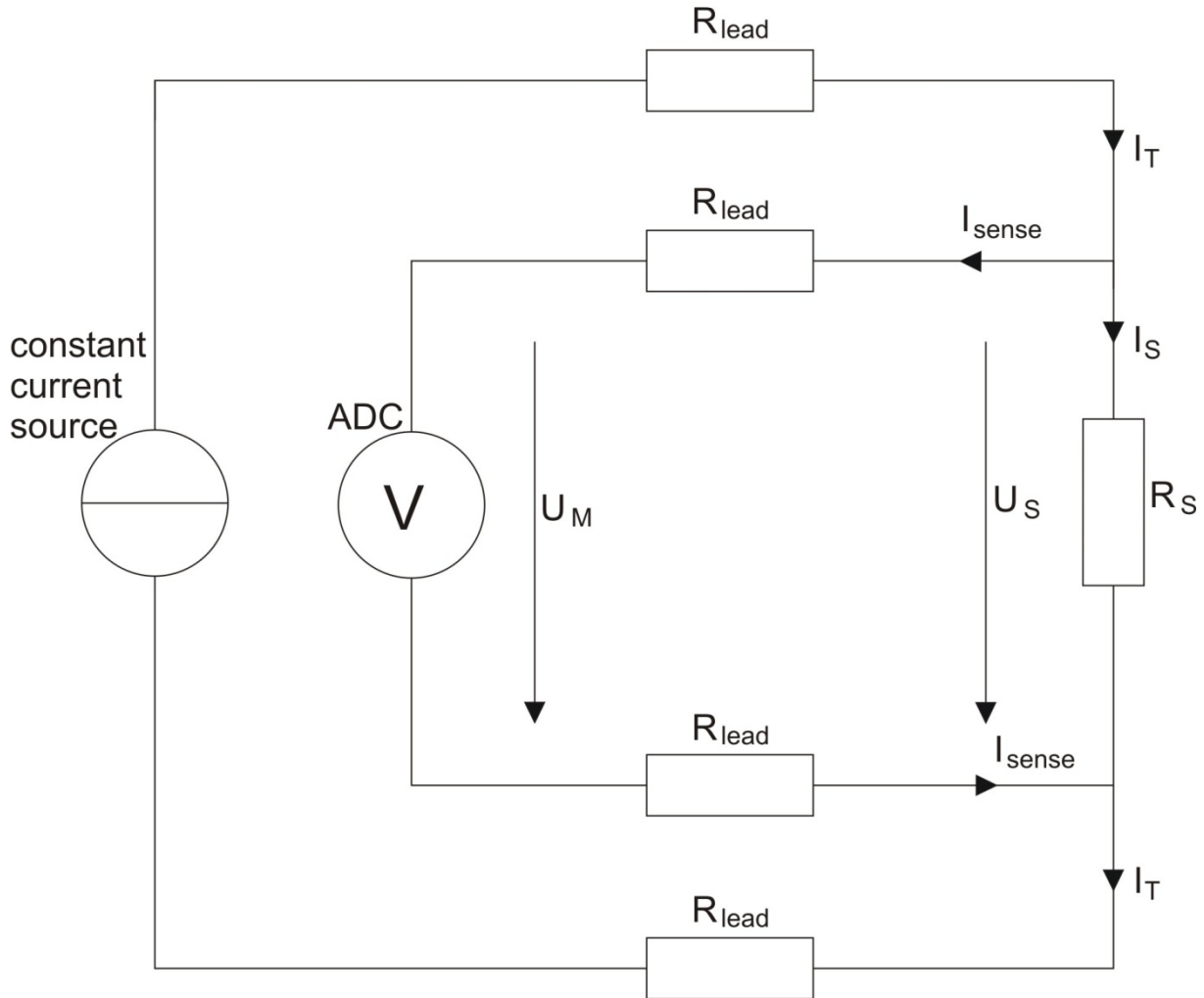


Figure 3-1: Schematic circuit of a four point resistor measurement. [10]

3.2 Four point structure

The specimens with the four point structures were externally developed at the Karl-Franzens-University Graz (KFU). In this master thesis three types of specimen were used, which will be introduced later within this chapter.

3.2.1 Layout design and Resistor deposition method

The four point structures have a special design enabling fast and simply resistor measurements and allowing the use at different instruments available at the institute. To provide comparability too the AFM the position of the macroscopic contact pads must be on the position shown in Figure 3-2. The inner part of the specimen is widely variable and includes the four point structure which is shown in Figure 3-3a. In the more zoomed part in Figure 3-3b and in Figure 3-3c the four parallel long lines which are about 2.5mm long and have a wide of only $0.5\ \mu\text{m}$ bzw. $1\ \mu\text{m}$ are shown.

The long lead allows it to often use the specimen structure for a resistor deposition. This principle is described in Figure 3-4.

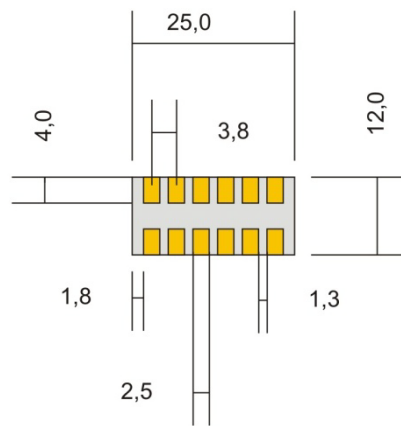


Figure 3-2: This image sketches the dimension for the compatibility too the AFM.

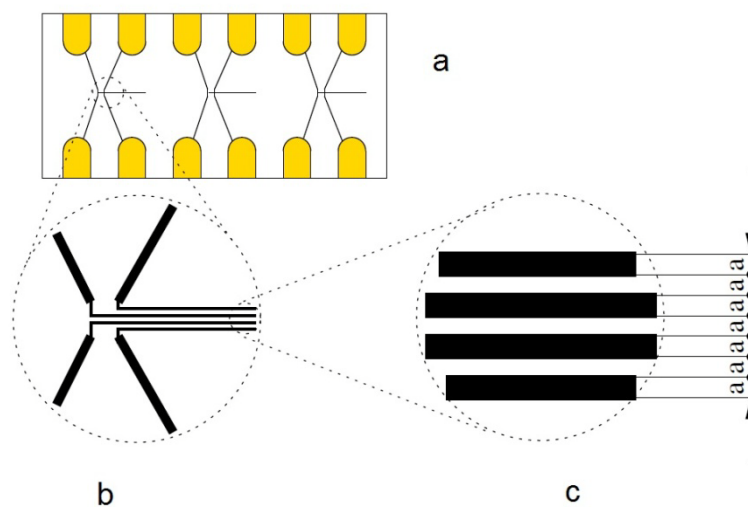


Figure 3-3: This image sketches the inner parts with the four point structure. Image a) is macroscopic and in image b) the inner part of the four point structure is sketched. The distances between the long lead are shown in image c) where the variable a has $0.5\ \mu\text{m}$ or $1\ \mu\text{m}$.

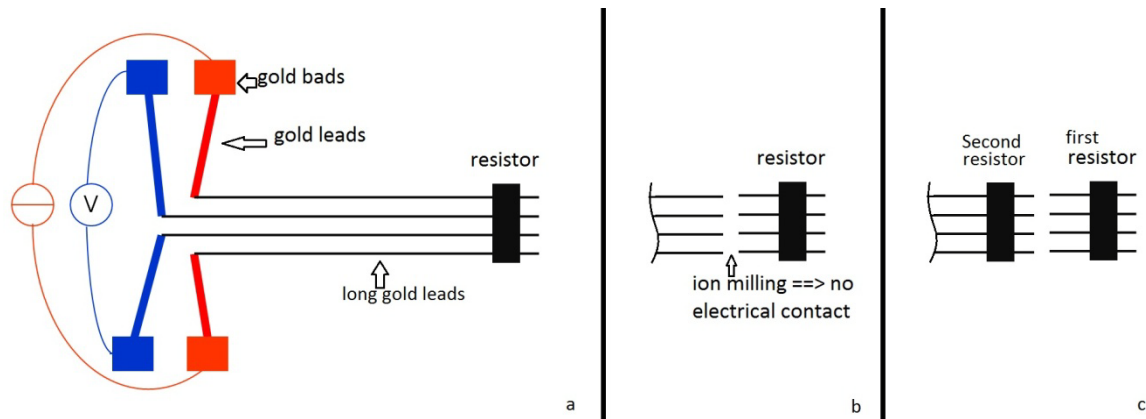


Figure 3-4: In a) the inner part of the specimen is shown. The red gold leads are connected with a constant current source which drives a current through the outer ones of the long gold leads over the resistor. The blue gold leads are connected to a voltage measurement (PC) which measures with the inner both long gold lead the voltage drop over the resistor. The resistor is deposited with EBID. In the middle image b) an ion milling cut of the resistor from the long leads. In the last image c) a new second resistor is deposited. This is repeated how long one would measure.

3.2.2 First prototype (glass sample)

First prototyping was carried out on a glass sample as shown in Figure 3-5. The thin leads will be connected with a platinum deposition in the FIB which is the resistor. This first specimen was a prototype for getting the first values, checking the possibility and finding problems.

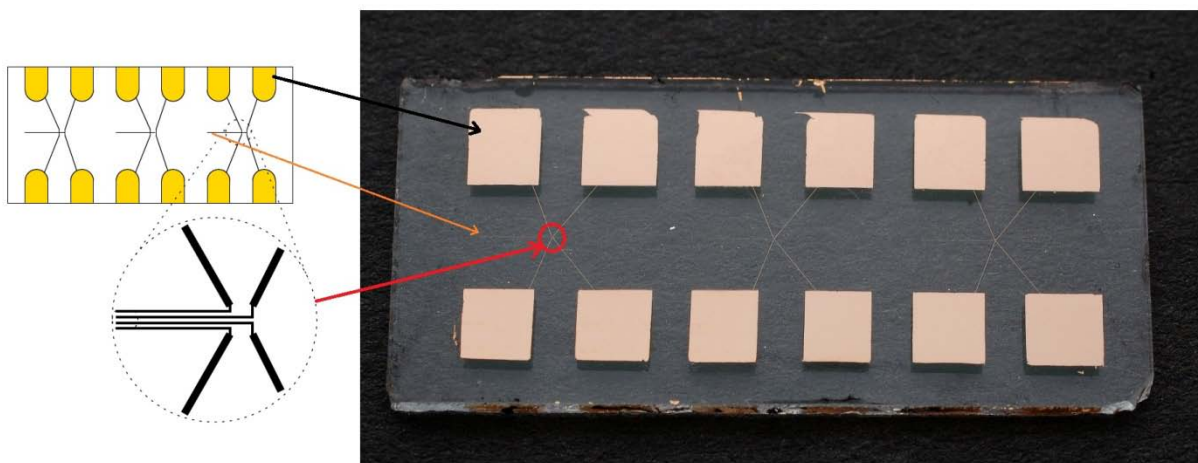


Figure 3-5: This macro shows the prototype called "glass sample". The small lead with the four point structure is visible.

The first prototype has many interruptions which were easy found, because the disconnected lead was charging. Interruptions were patched with a platinum deposition in the FIB to reconnect them. Sample pictures from the first prototype are shown in Figure 3-6 and Figure 3-7. In these pictures the disconnection in the cross of the four point structure and a stitching interruption is shown.

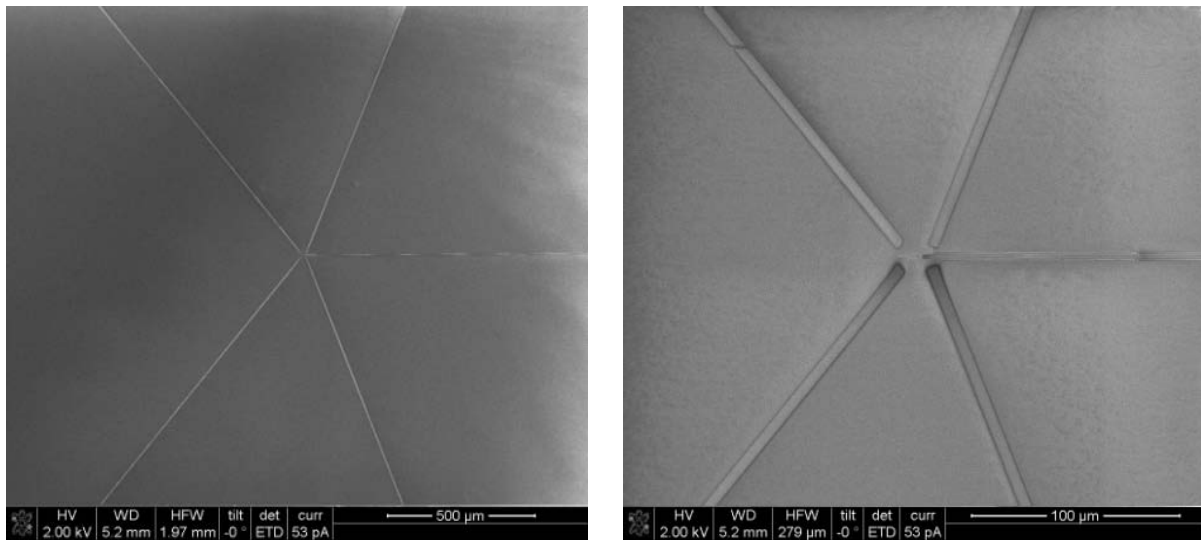


Figure 3-6: First prototype of the four point structure. In the left picture the interruption is not visible but in the right picture the magnification is high enough to see the interruption in the center and it also seems that the leads are interrupted. Higher magnified is shown in Figure 3-7.

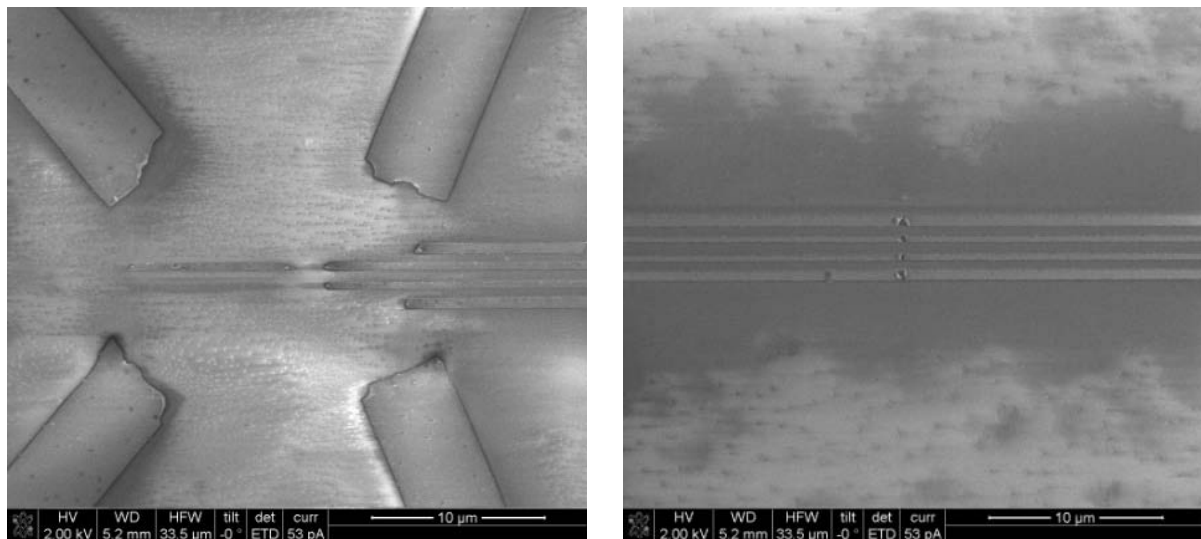


Figure 3-7: Higher magnifications of the first four point prototype allow seeing the disconnection problems in detail. The left image illustrate the damage of the four point cross and the right the stitching interruption.

The next problem is that the leads get damage over time because the gold leads are not stable because they are not in a sufficient thermodynamic equilibrium. Such damages are shown in Figure 3-8. The left image of them shows an interruption with a small connection but must be patched because the resistance is too high. The right image shows a big disconnection during repairing process. The first small lead between the broken ones, is deposited. This short and fast deposition lead provides only a small connectivity. A better big deposition was followed after two future more leads. Deposition on a non connectivity surface is hard and will only work slowly until a minimum of connective is reached. The reason of this is charging.

So it gives errors from the production which could be solved by Dipl.-Ing. Dr. Andreas Hohenau and interruptions which comes through the not stable gold leads and storage. This could be solved by storing in an exicator.

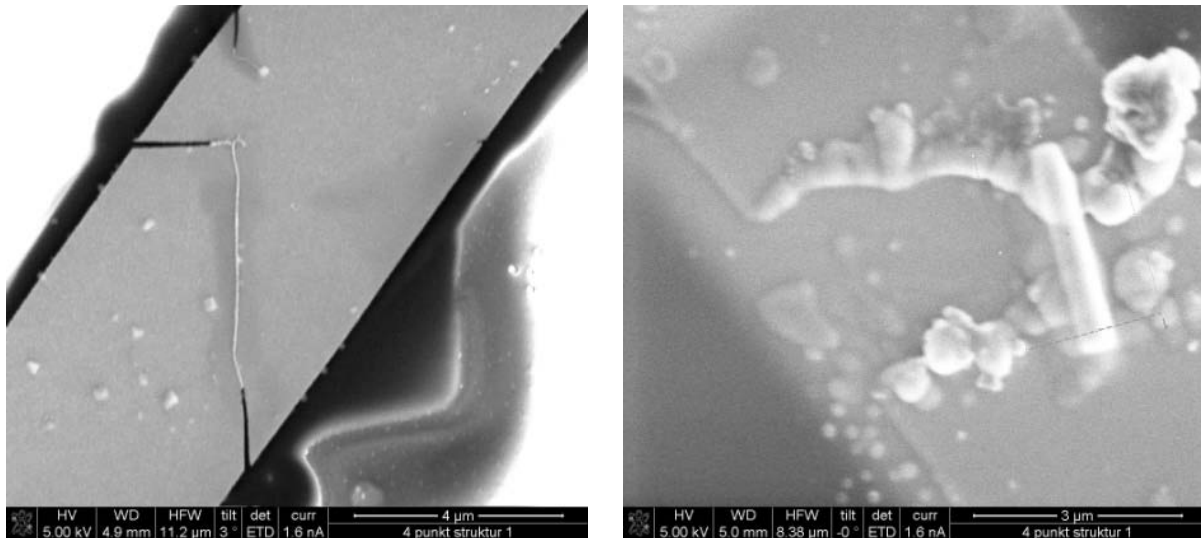


Figure 3-8: Left picture demonstrate an error. The left image shows a partial interruption which has a connection but with a high resistance. The other picture shows a big disconnection during repairing process.

3.2.3 Second prototype (two point structure)

This prototype was used for more general tests while improved 4-point structure was fabricated due to the problems described in the previous chapter. With this two point structure, basic *in situ* tests during deposition were performed in terms of “proof of concept”. The structures were fabricated on a silicon substrate having 50 nm siliconoxide top-layer with six gold pads with a gap of 25 μm across the entire contact pad. A macroimage of the prototype is shown in Figure 3-9 and a SEM image for a better observation of the gap in Figure 3-10.

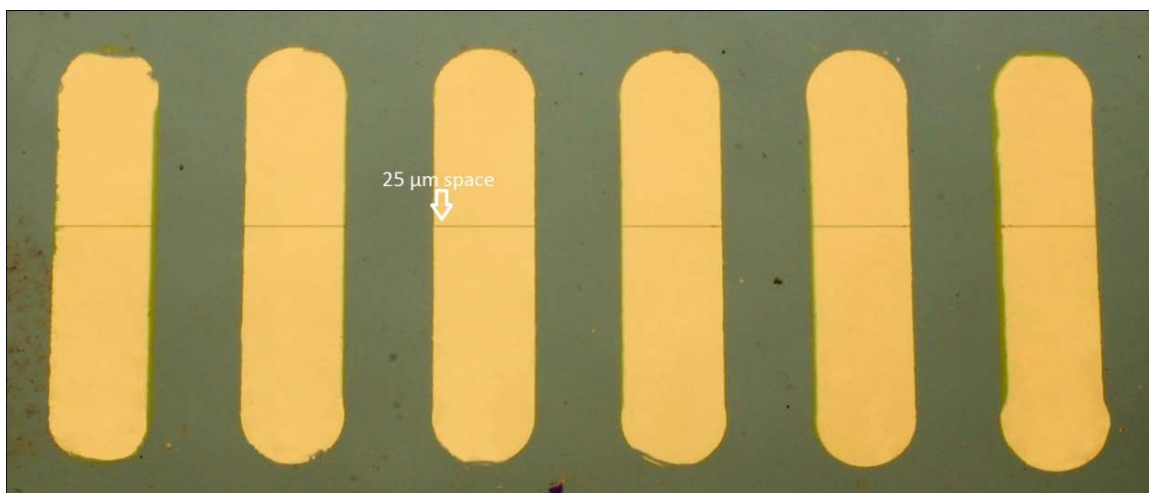


Figure 3-9: Image of the second prototype. The gap between the gold contacts has 25μm.

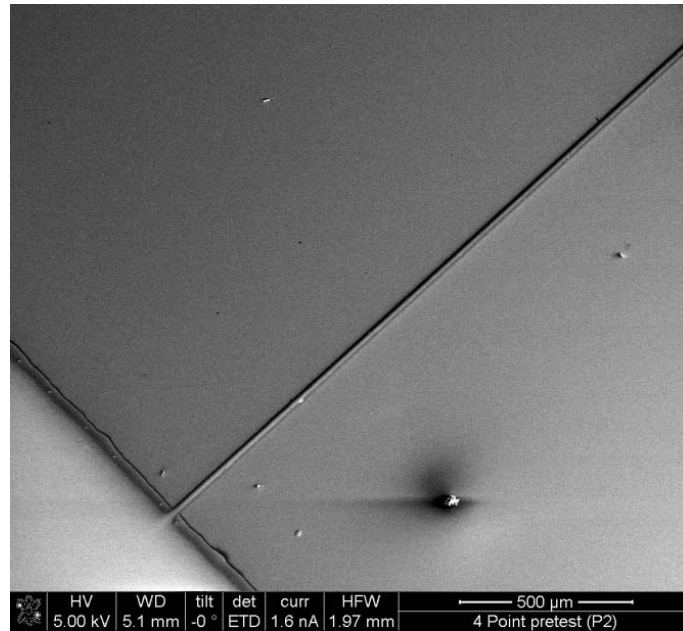


Figure 3-10: SEM image of the 25µm gap.

3.2.4 Final specimen

This is the final specimen in which the improvements which were found out in the last once are included and the interruption completely fixed. The ground material of the final specimen was chosen as silicon instead of glass, with a 500 nm siliconoxide layer on top of it. On this layer the gold pads and leads were formerly deposited by a method called mix and match. The leads were fabricated by using electron beam lithography [28] and after that the pads were placed by shadow mask CVD preparation. Figure 3-11 shows the macroimage of the specimen in which it can be seen that the structure is the same as the first prototype (see Figure 3-5), but instead of the glass sample one see the blue surface of the SiO_2 layer with the typical color of a 500 µm coating is visible. Figure 3-12 and Figure 3-13 presents the SEM images of the corresponding structures. Compared to Figure 3-6 and Figure 3-7, one can see the same structure but no interruption and stitching problems as the leads are fully connected.

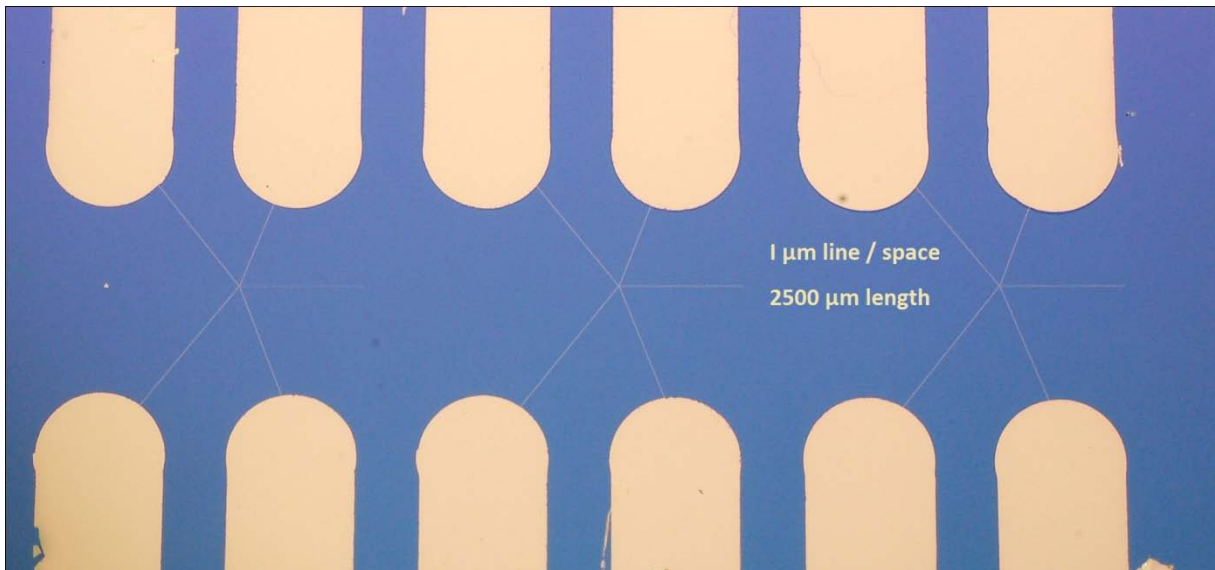


Figure 3-11: Macroimage of the final specimen.

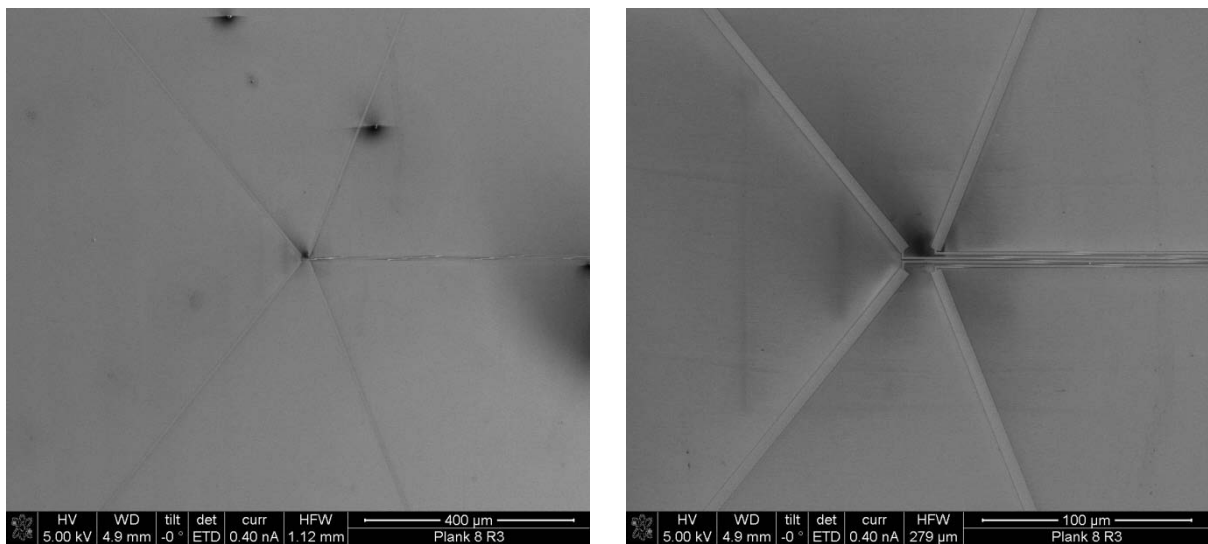


Figure 3-12: SEM image from the center of the four point structure, left with less magnification and right with moderate magnification.

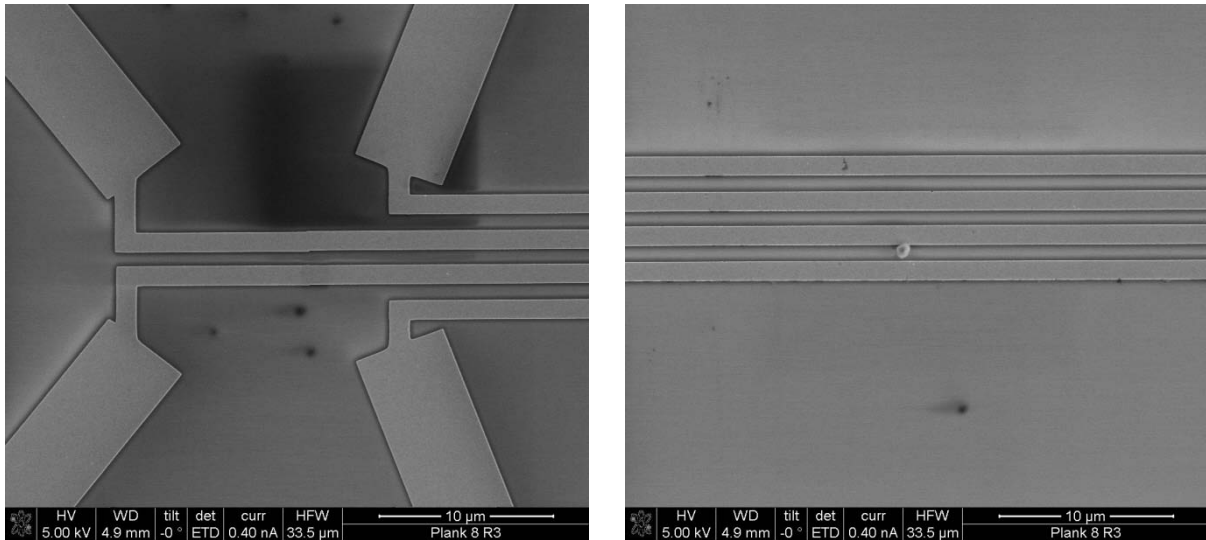


Figure 3-13: Left a zoomed area of the center of the four point structure and right with same magnification the long leads. No interruptions are visible.

3.3 Current source

To be used for the four point resistor measurements, a constant current source was required. The developments and considerations will be discussed in the following parts of this chapter.

3.3.1 Fundamental considerations

As an initial step of the work mentioned above, it was necessary to find out the maximal current value which can be driven over the resistor. Which resistance value has the current and the voltage lead and the resistor which is from interest. For the measurements of those values, the first prototype of the four point structure was used.

First of all, it was essential to estimate the resistance value. The dimensions of the resistor were about $1\mu\text{m}$ in length, wide and height. According to the literature [22] such a resistor should have about $10 - 20\ \Omega$ which is about 100 times higher than pure platinum.

The leads can be separated in two groups: thick and long ones and thin ones. Thick and thin leads could be viewed in Figure 3-13. With the normal gold resistance (electrical resistivity = $22.14\ \text{n}\Omega\text{m}$ at $20\ ^\circ\text{C}$) and dimensions of $2\ \text{mm} \times 5.5\ \mu\text{m} \times 40\ \text{nm}$ for the thick leads and $2,5\ \text{mm} \times 0.5\ \mu\text{m} \times 40\ \text{nm}$ for the thin leads, a resistance of approx $5.9\ \text{k}\Omega$ can be calculated. For smaller dimension the resistance is normally higher, and therefore a resistance in the range of $15 - 100\ \text{k}\Omega$ can be estimated. This estimation is for getting a theoretical approximation of the expected real values for dimension and planning. In a later pre-measurement a resistor of $30\ \text{k}\Omega$ in the thicker leads was measured.

The problem was that the measured resistance was quite low and the measured current should not be too high. It is well possible that the current heated the resistor and changed the chemistry permanently. Such current effects are described in [5]. The current through the resistor was assumed to be 1 – 10 μA . This results in a small voltage drop over the resistor and hence a low signal-to-noise ratio. The Analog-Digital-Converter (ADC) does not have sufficient resolution and the minimal input current for the ADC is higher than the current with will flow, so an instrumentation amplifier must be implemented.

3.4 Electrical circuit design

The electrical circuit incorporated the following units:

- Power input
- Constant current source
- Instrumentation amplifier
- Internal for point measurement
- Shielding

The power input was designed for an external power supply and was consisting of two high capacitive electrolytic capacitors, and two Schottky diodes for the reverse voltage protection and against a discharge of the power supply. At a later date the circuit was powered by internal batteries which make these diodes and capacitors needless. The batteries have the advantage that the use of an additional device is not needed which makes the handling easier. A further advantage was that no noise came from power supply cables and the power supply had a completely constant voltage signal.

The constant current source was designed with an LM 234 [26] and two cermet precision trimmers for coarse and fine adjustment of the deliberated current. Temperature compensation was not required because the FIB lab was regulated with an air conditioner at a constant temperature of about 18 °C.

For amplification, an instrumentation amplifier from type INA 121P [25] was used. This was a field effect input low power instrumentation amplifier. It needed a small input current from 4 pA so that the resistor measurement will not be influenced [25]. The amplification could be adjusted with external resistors. These resistors were two cermet precision trimmers, for coarse and fine, gaining a fine adjustment of the magnification.

With the internal four point measurement it was possible to check the adjustment of the used force current by measuring the voltage drop over a known resistor.

To minimize the noise, it was necessary to shield the whole case. For this, the plastic case was coated with a conductive copper spray. The cables from the specimen to the circuit and to the ADC were coaxial cable.

The circuit is shown in Figure 3-14 and a picture of the complete circuit is given in Figure 3-15 and Figure 3-16.

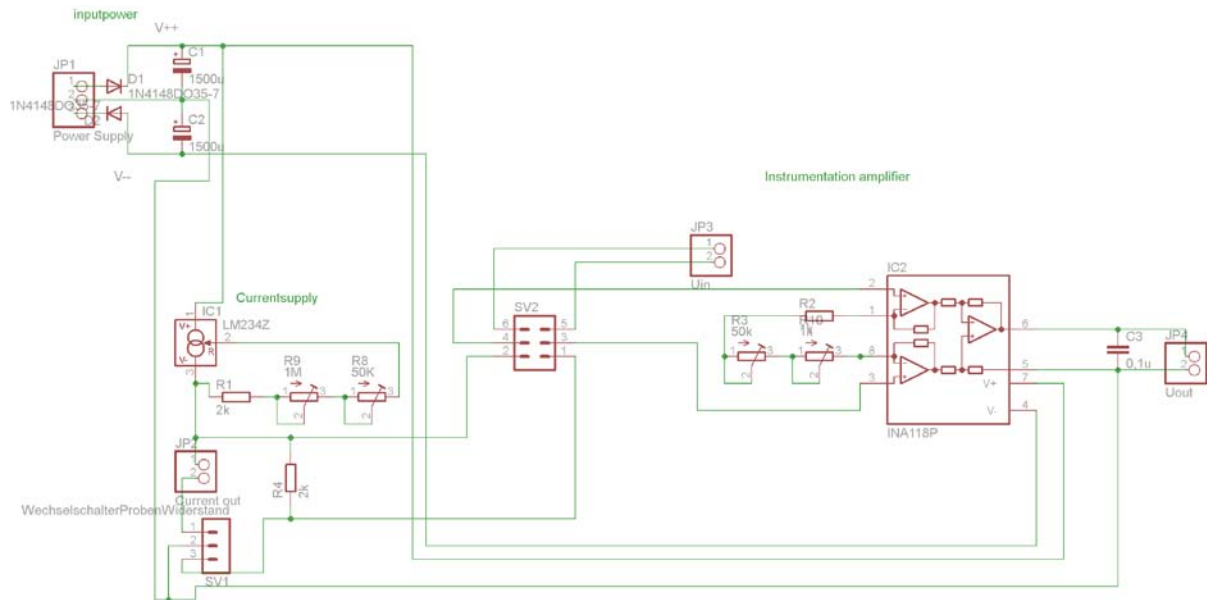


Figure 3-14: Circuit diagram of the circuit designed in EAGLE.



Figure 3-15: Box with the electric circuit.

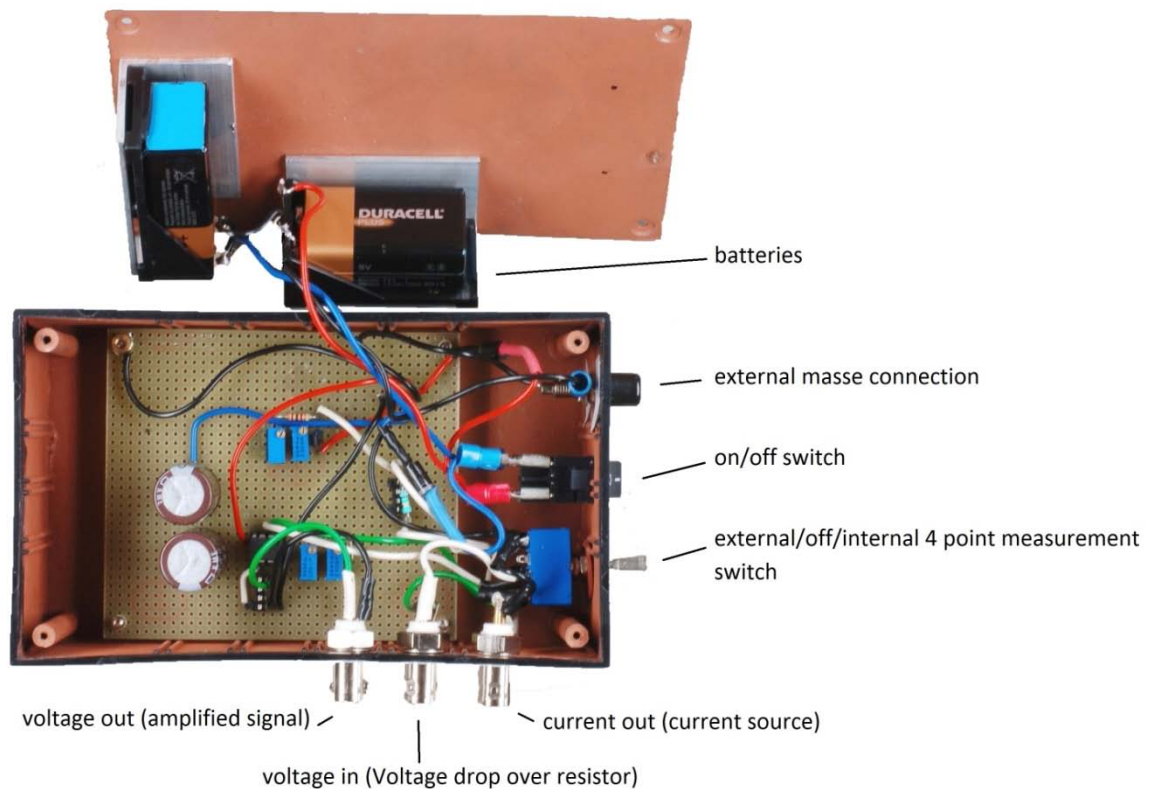


Figure 3-16: Opened box with the electric circuit.

3.5 Specimen holder

The built-in-house specimen holder is shown in Figure 3-17. The specimen was fixed with the clamps which also serve as the electrical connectors. The leads were shielded and connected to a flange with an RS 232 interface to get the leads out (see Figure 3-18). From the flange another cable was connected to the electrical circuit. The specimen holder is shown in Figure 3-19 .

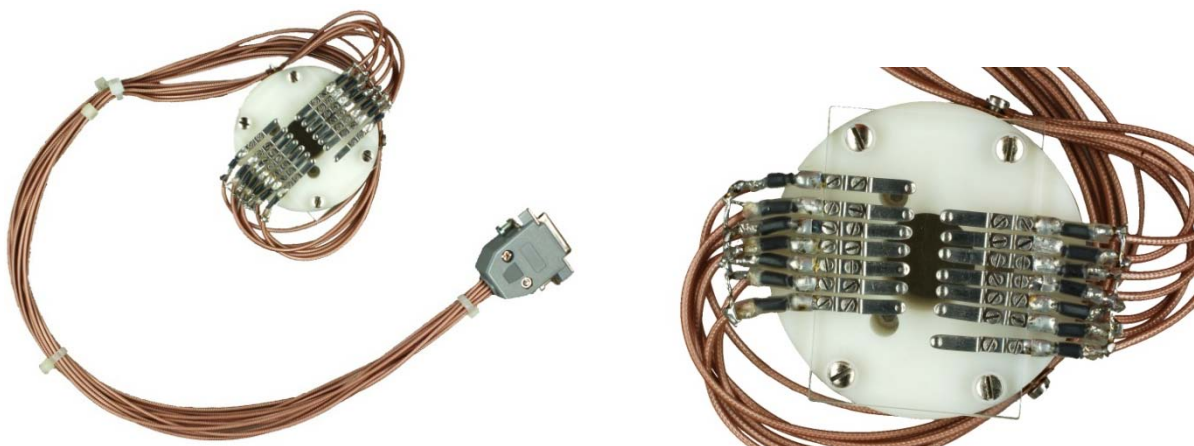


Figure 3-17: Left image shows the sample holder including the cables and the magnified image on the right side shows the detailed structure.



Figure 3-18: Shows the cable which gets through a RS232 flange out of the FIB.



Figure 3-19: The left image shows the specimen holder which is build in the FIB while the chamber is open whereas the right image shows it while the chamber is closed. In both cases the mounted specimen is the second prototype.

3.6 Pre testing

3.6.1.1 Functional testing of the power supply with resistors

The functional testing was performed to prove whether the electrical circuit was working correctly. The measured resistors were standard resistors in the range of 1 k Ω until 1 M Ω . The resistor and leads were not shielded. The range of noise was in the range of 10 mV to 50 mV. The most apparent frequency was the 50 Hz utility frequency. To estimate the stability of the current source, a long term test was started over one week where the current varied only about 1.5 %. The reason could be that, either the LM 234 had a great dependence on the ambient temperature or it was a drift of the electrical components. Nevertheless, the current

source is proven to be stable enough for the intended characterization which took maximum 12 hours (whereas only a few hours for normal measurements series).

3.6.1.2 *Ex-situ* four point structure testing

The aim of these experiments was the interaction of the full electrical circuit concerning cables, power supply, ADC and four point structure. For this, a huge resistor was deposited on a destroyed four point structure and measured in ambient air with $0.5 \mu\Omega$ until $10 \mu\Omega$. According to the measurements, the resistor had a value of about $30 \text{ k}\Omega$ while gold leads had approximately $15 \text{ k}\Omega$ (in sum $30 \text{ k}\Omega$) and the deposited platinum voltage connector had a value of $100 \text{ k}\Omega$ per piece.

On the next day the resistor was measured again but it was found out that either the resistor or leads were disconnected (values in $50 \text{ M}\Omega$ range, measured with a two point measurement with the aperture “Keithley 100 system DMM”). SEM inspection revealed the broken leads as shown in Figure 3-8, but more surprisingly the deposited resistor was completely destroyed as can be seen in Figure 3-20.

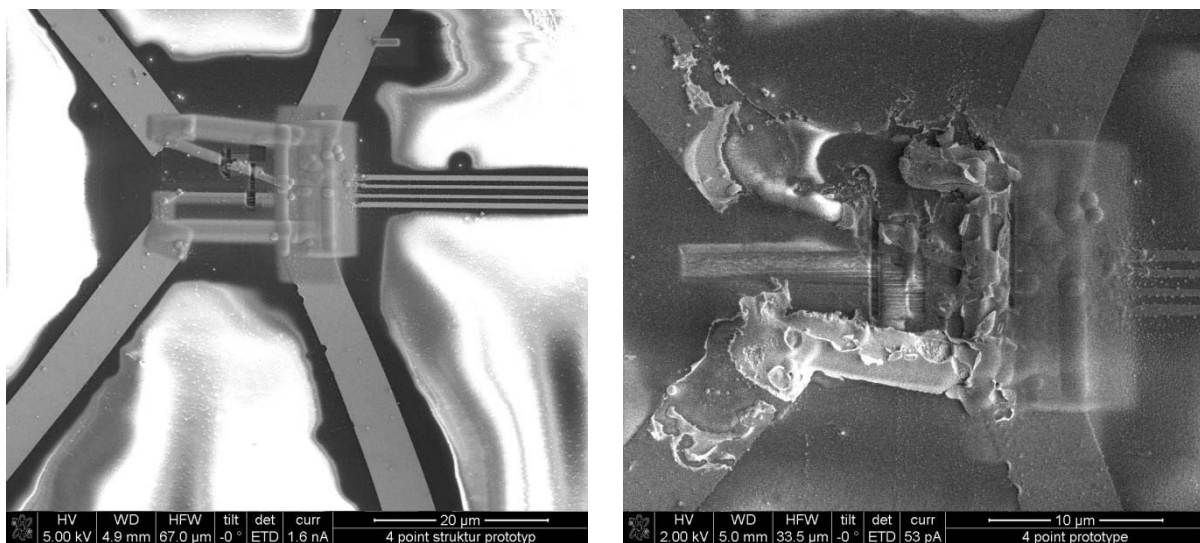


Figure 3-20: On the left side a deposited testing resistor after deposition is presented. On the right side the specimen is shown after measuring in ambient air and storing one day in a Petri dish.

3.7 Data acquisition

To measure the voltage drop over the resistor, a National Instrument Analog Digital Converter from type “NI DAQCARD 6036E Multifunction I/O F” was utilized. The used analyzing PC and the ADC card are shown in Figure 3-21. As the program language LabVIEW was used.



Figure 3-21: In the left image the analyzing PC with the ADC card is shown. The right image shows the used ADC card adapter.

3.7.1 LabVIEW program code

The core part of the program code is a tool from nation instruments which control the ADC.

Input parameters were:

- the acquiring time, which corresponds to the time for data acquisition until data writing and which was chosen as one or ten seconds.
- the sample rate, defining the number of measurements done per second. A default value was 1000 samples/second.
- signal channel.
- the measuring voltage, defining the voltage range.

The subprogram started the conversion automatically and wrote it on an output, from where the data were stored on hard disk. This was repeated until the stop button is pressed. The program code is shown in Figure 3-22 and the user panel in Figure 3-23.

an additional time during which no further data can be acquired. Hence, a “dead time” is introduced depending on measurement points and acquisition time. To access those dead times, systematic experiments were performed whose results are summarized in Table 3-1. For this, a sample rate from 100, 1000, 10000, 100000 was chosen and for each of them an acquisition time of 0.5, 1, 2, 4, 8, 16, 32 seconds. The left table in Table 3-1 shows only the measuring time. One can see that with less acquisition time and low sample rate the measuring time is short but in increase with more sample rate and acquisition time. In the right table the measurements time resolution is subtracted. Now, one has to find a balance between enough sample rate to see most effects and a acquisition time which is long but the “dead time” is small enough to too not have a long data loss in which important effects could happen. With 1000 sample rate, a frequency of 500 Hz is measurable and this should be enough for standard experiments. Lower sample rate would also not decrease the dead time dramatically. The acquisition time of ten seconds seems meaningful by having a good balance.

Table 3-1: Table showing the time lost between two acquisition times. The acquisition time is the time in with the ADC collects measure values. In the right table the measurements time resolution is subtracted. This time is the time interval between two measurements. At 100 points it is 10 ms because 1 second divided by 100 is 10 ms.

		measurement points []			
		100	1000	10000	100000
		measurement time [s]			
acquisition time [s]	0,5	0,03	0,02	0,14	1,32
	1	0,07	0,08	0,33	2,70
	2	0,08	0,09	0,57	4,82
	4	0,08	0,14	0,95	12,14
	8	0,04	0,19	1,89	29,53
	16	0,07	0,38	3,92	-
	32	-	0,76	-	-

		measurement points []			
		100	1000	10000	100000
		measurement time - measurement time resolution [s]			
acquisition time [s]	0,5	0,02	0,02	0,14	1,32
	1	0,06	0,08	0,33	2,70
	2	0,07	0,09	0,57	4,82
	4	0,07	0,13	0,95	12,14
	8	0,03	0,19	1,89	29,53
	16	0,06	0,37	3,92	-
	32	-	0,76	-	-

3.7.3 Filter and data

The measured data which are stored on the hard disk had a noise which is a summation of the converting error of the ADC, constant current noise and the electrical influences from outside which could not be properly shielded. To improve the signal-to-noise ratio, a digital filter was developed and two filter modes were programmed. The first had a lower noise reduction but a high time resolution, the second had a good noise reduction but a low time resolution. The first is used to see changes in ms range and the second filter mode for seeing a trend. This is also shown in Table 3-2.

Table 3-2: Comparison of the two filter modes.

filter mode 1	filter mode 2
low noise reduction	high noise reduction
high time resolution	low time resolution
seeing changes in ms range	seeing a trend

The diagrams were arranged as shown in Figure 3-24. Diagram (a) and diagram (d) are the raw signals which were directly measured. Diagram (a) shows the measured voltage over time and (d) the logarithms of the FFT-signal of the raw signal. The next two diagrams (b) and (e) are the ones with “filter mode 1”. The last two are with “filter mode 2” in diagram (c) and diagram (f) shows the gradient but not the frequency domain. In the diagrams (a), (b) and (c) in addition to the blue line, a red line is given. This red line is for seeing the trend when zoomed in detail, which is a middle of the both filter modes. In the gradient (diagram (f)) also a red line is added. This red line is a polynomial fit of third degree.

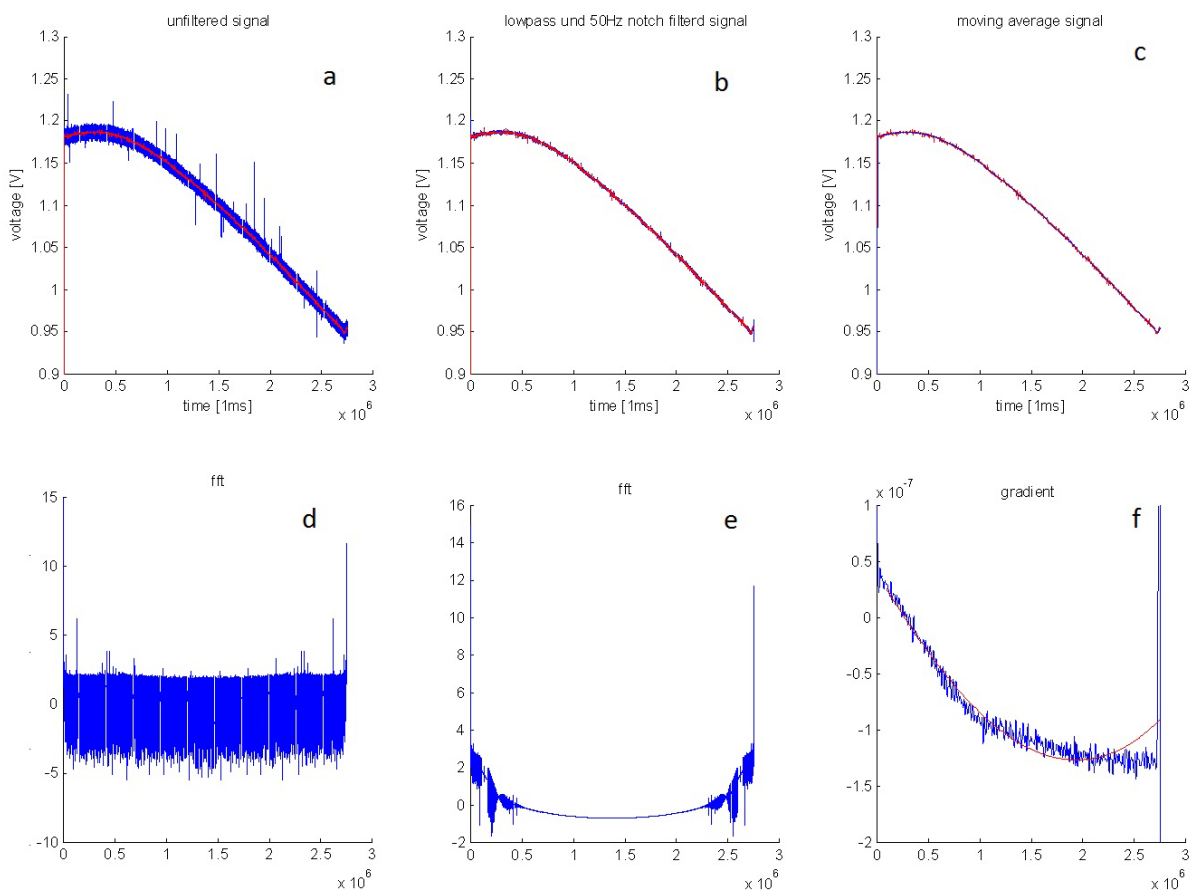


Figure 3-24: Measured dataset for describing the different diagrams.

The effect of the filter is shown in Figure 3-25 revealing the same time with the same voltage range. “Filter mode 1” is a low pass filter of one-fifth of the input-sample-frequency including a 50 Hz notch filter. “Filter mode 2” is the same as filter mode 1, but with an additional moving average which has a window length of ten seconds. The red line is similar to “filter mode 2” however having only a window length of 0.1 seconds, which gives a better time resolution, but a worse noise reduction. It can be clearly seen that “filter mode 1” reduces the noise dramatically by minimizing the 50 Hz frequency and the high frequencies. The “filter mode 2” reduces the noise much more and makes it smooth but the signal shows no rapid changes. For this reason this filter mode is only useful for seeing a trend.

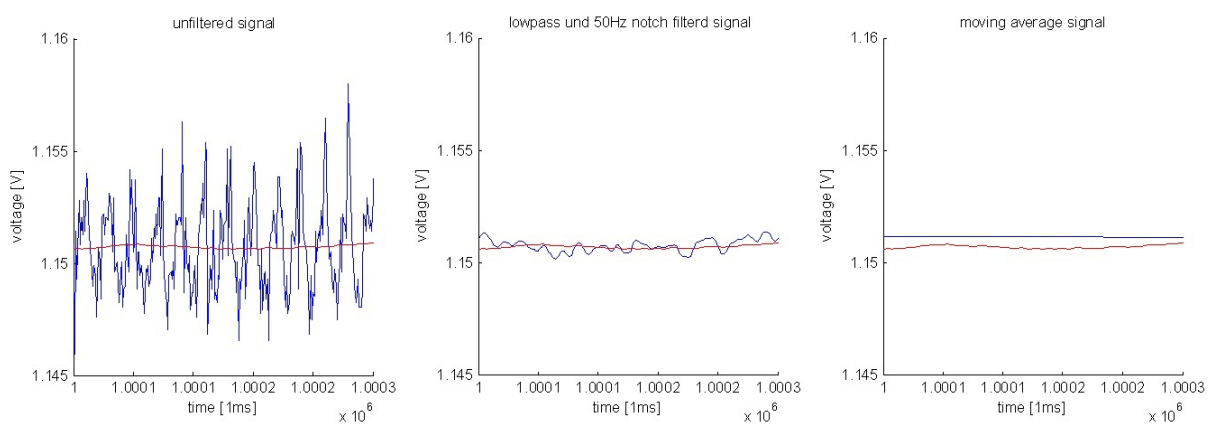


Figure 3-25: Illustration of the filter modes and the effect. “Filter mode 1” reduces the noise with a factor of ten. The “filter mode 2” smoothens the signal but with a loss of time resolution.

4 Chapter 2: Feasibility studies and first results

results

In this chapter, the measuring methods and gathered results of the resistance measurements will be given. The findings of the experiments will only be qualitative and the aim was testing the system, generating first results, encountering problems and providing essential information for future experiments.

4.1 Measuring methods

The deposition of the resistors was carried out using two measuring methods, which will be given in detail as follows:

Method one; parallel arrangement (PA):

For this application, a first resistor of platinum was deposited on the sample using EBID max smooth patterning (see chapter 1.2.4) which would act as base R value (see Figure 4-1). Then the second resistor of interest was fabricated near the first one and electrically measured *in situ* during deposition. This method is called “parallel arrangement” and it is applied for the reason that the current source drive a constant current over the resistor. If the resistor growth the first layer of the resistor would have a high current density due to the very small cross section which could eventually led to the material destruction and even make the measurements questionable or even impossible. If a other resistor is parallel, the current density will be lower, as the current will flow through the parallel resistor and not through the second. If the first resistor has a known resistance value, it is well possible to calculate the value for the second.

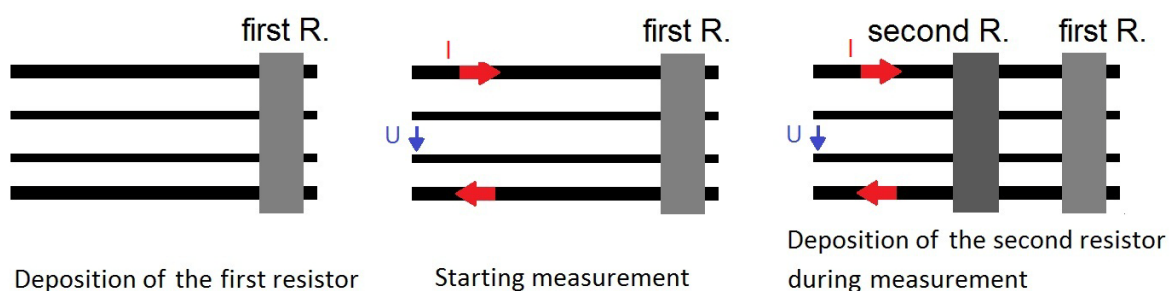


Figure 4-1: Demonstrate the principle of the parallel arrangement method.

Method two; single arrangement (SA):

This method is applied without using the first resistor as a base. The resistor of interest was build up, but it was not investigated how the first layers were influenced (see Figure 4-2).

The methods revealed two different curve progressions, which are demonstrated by a calculation as follows: The voltage U_{normal} is the voltage drop over R_{normal} and is the same for U_{parallel} , the voltage drop, over both resistors. In Figure 4-3 the curve shows the voltage drop of a resistor with the values ranging from 5095Ω to 100Ω with a current of 1 mA , One with a parallel resistor of 1000Ω and one without. It can be viewed that the parallel grown resistors in the beginning cause only a small change but later the voltage fall more. The second resistor has later more influence on the sum of these both resistors. The voltage drop of the resistor without a parallel resistor is linear. But if one considers that the resistors do not grow linearly, but in layers (height), a behavior which is plotted in Figure 4-4 is achieved. Here the deposited resistor is grown in 185 layers, of each layer having a resistance of $100\text{ k}\Omega$. So the resistance varies from $100\text{ k}\Omega$ to 550Ω . It can be seen that the voltage drop is caused in the beginning very fast by the second method. This behavior must be kept in mind for further interpretations of the results.

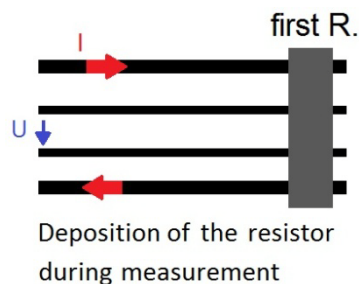


Figure 4-2: Demonstrate the principle of the single arrangement method.

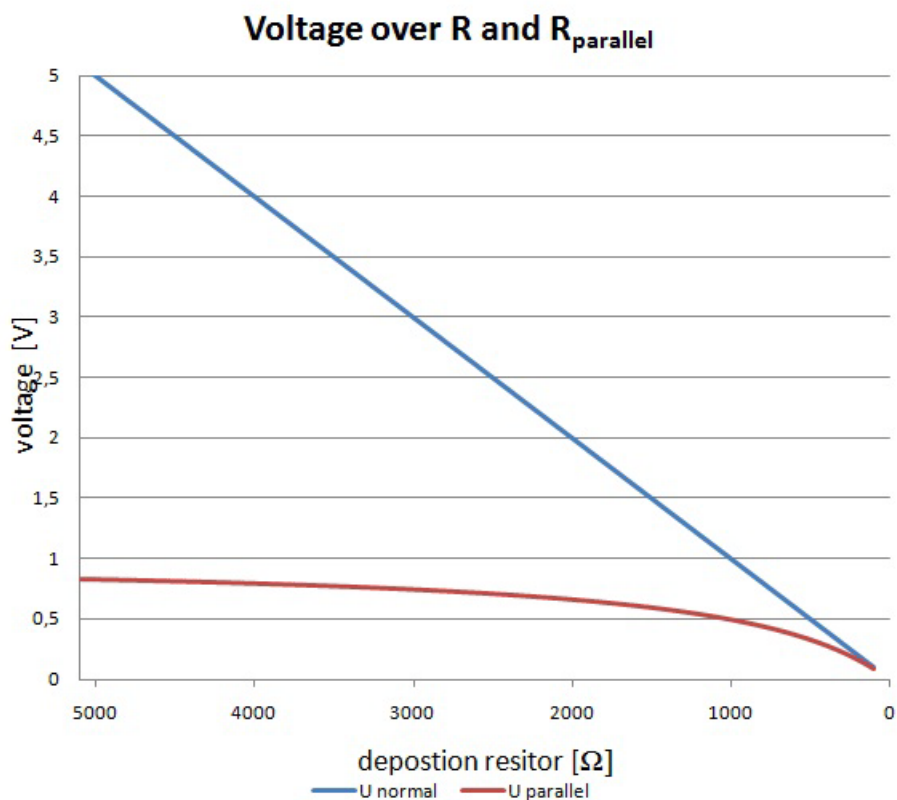


Figure 4-3: The measured voltage over two resistors having a range of 5095 Ω to 100 Ω . One of them is parallel to a 1000 Ω resistor.

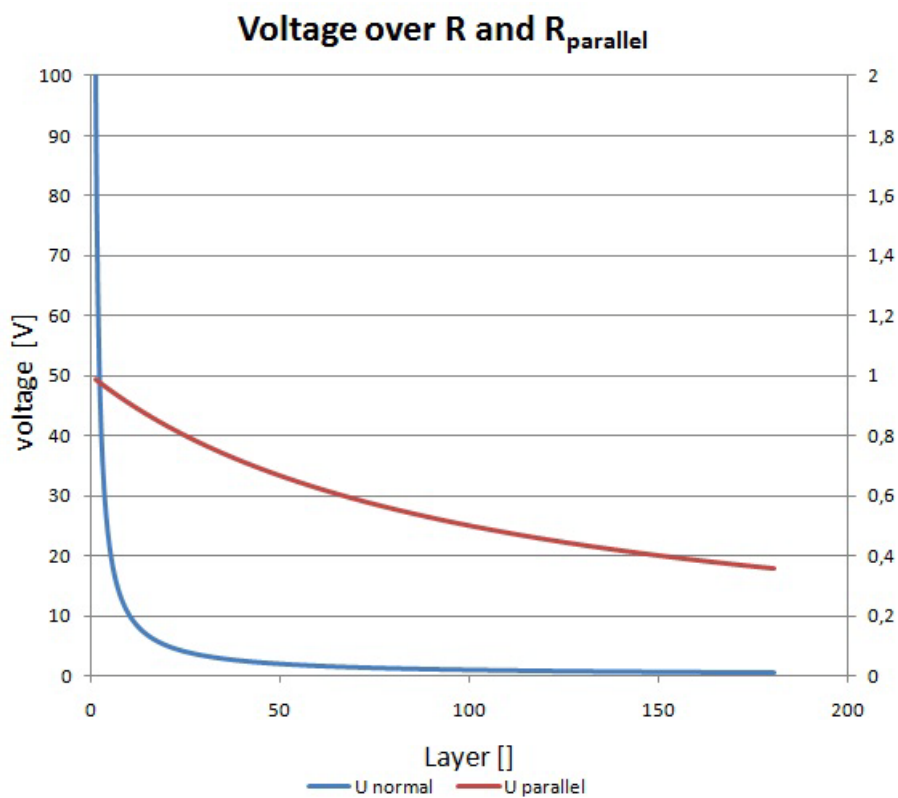


Figure 4-4: Shows the voltage over two resistors which have a range of 100 k Ω to 550 Ω and are growth in layer in which each layer has 100 k Ω . One of them is parallel to a 1000 Ω resistor.

Nevertheless, each method has advantages and disadvantages. For example with the SA method the first layer could never be observed because through the ohm law, the voltage drop of this thin layer would be very high due to a large resistance value . This would be always out of the voltage input range of the measurement tool. On the other side the PA method would theoretically allow the measurement of the first layers, but here the resistors have also in the beginning a high value. This value is parallel to the first resistor which has in relation to the new resistor a very small value. So the change in the amplitude of the measured signal is too weak to detect it with the measurement tool. With first method, the variance in signal gets higher if the second resistance in relation to the first is small. This could be seen in Figure 4-7 where the steps gets higher the smaller the second resistors is.

4.2 Data convolution

The results gathered via the electrical *in situ* measurements are not interpretable straight forward. The values and the temporal behavior are “convoluted” by several factors:

- Measurement method (SA or PA) and their influence which is described see 4.1
- During the growth, the resistor changes from a quasi-2D to a real 3D structure caused by the percolation conditions due to the small Pt crystals embedded in the (less conductive) hydrocarbon matrix
- Temporal growth rate of the deposition which is not linear and hence changes the curvature of the real temporal behavior (see 2.2.2).
- Beam influence since an additional current is brought into the system which is the described in 4.3.3

4.3 First *in situ* measurements

The first *in situ* tests were done on the second prototype, which is introduced in chapter 3.2.3. The following experiments were carried out as fundamental measurements to check the reliability of the system.

4.3.1 Applying a voltage

First it was of interest to check if the system including the sample holder, cable and flange works. For this, the second prototype (Figure 3-9 and Figure 3-10) which has a 25 μm gap between gold contacts was placed inside the FIB-chamber and a voltage of + 100V was applied to one of the six gold pads. This voltage reduced the brightness by attracting the beam electrons to the gold pads, as a negative potential would work it the other way around. This is shown in Figure 4-5. This test confirmed that the flange system, the cables and connectors as well as the sample holder itself had been working inside the dual beam system as intended.

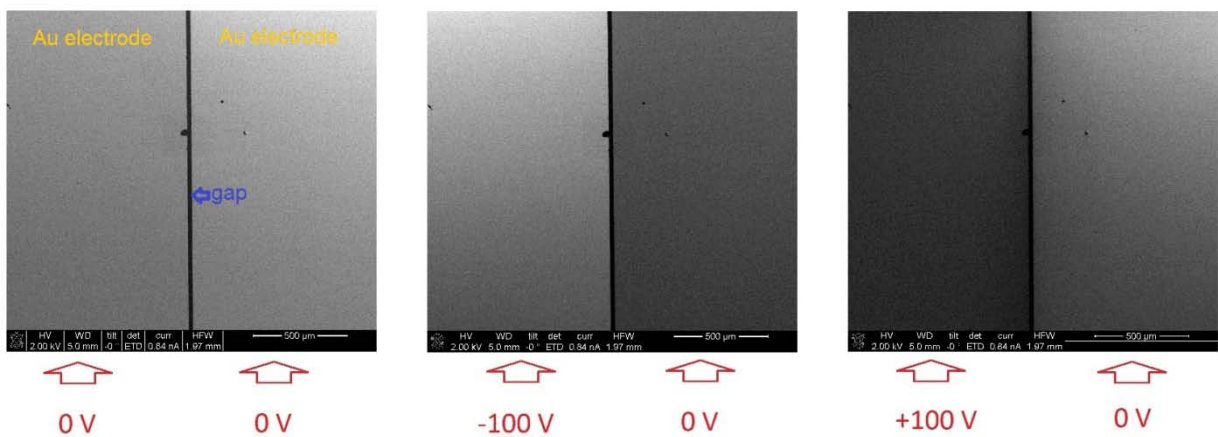


Figure 4-5: These images show the measurements by applying a voltage from an outside voltage source. In the left image no voltage is applied. In the middle image the left gold pad has - 100V and in the right image this gold pad has a potential of +100 V against ground potential.

4.3.2 The first resistor (R1_U0)

The first platinum resistor was deposited on the second test structure (Figure 3.2.3) using EBID in the dual beam instrument, and was measured by two point technique. This measurement was performed using the circuit shown in chapter 3.4 but here the measurement signal “voltage in” was taken over the signal “current out”. This is then a two point measurement. The goal of this experiment was to track the resistance decay during the deposition process. For this experiment, the patterning parameters which are given in Table 4-1 were used:

Table 4-1: Deposition data from the measurement R1_U0.

Name	R1_U0
current	qualitative
pattern length	35 μm
pattern height	1 μm
pattern width	3 μm
resistor length	25 μm
resistor height	not measured
loop time	85 ms
total patterning time	~ 45 min
parallel measured	yes
sample rate	1000
aq. time	10 s
Amplifier	5x
special	

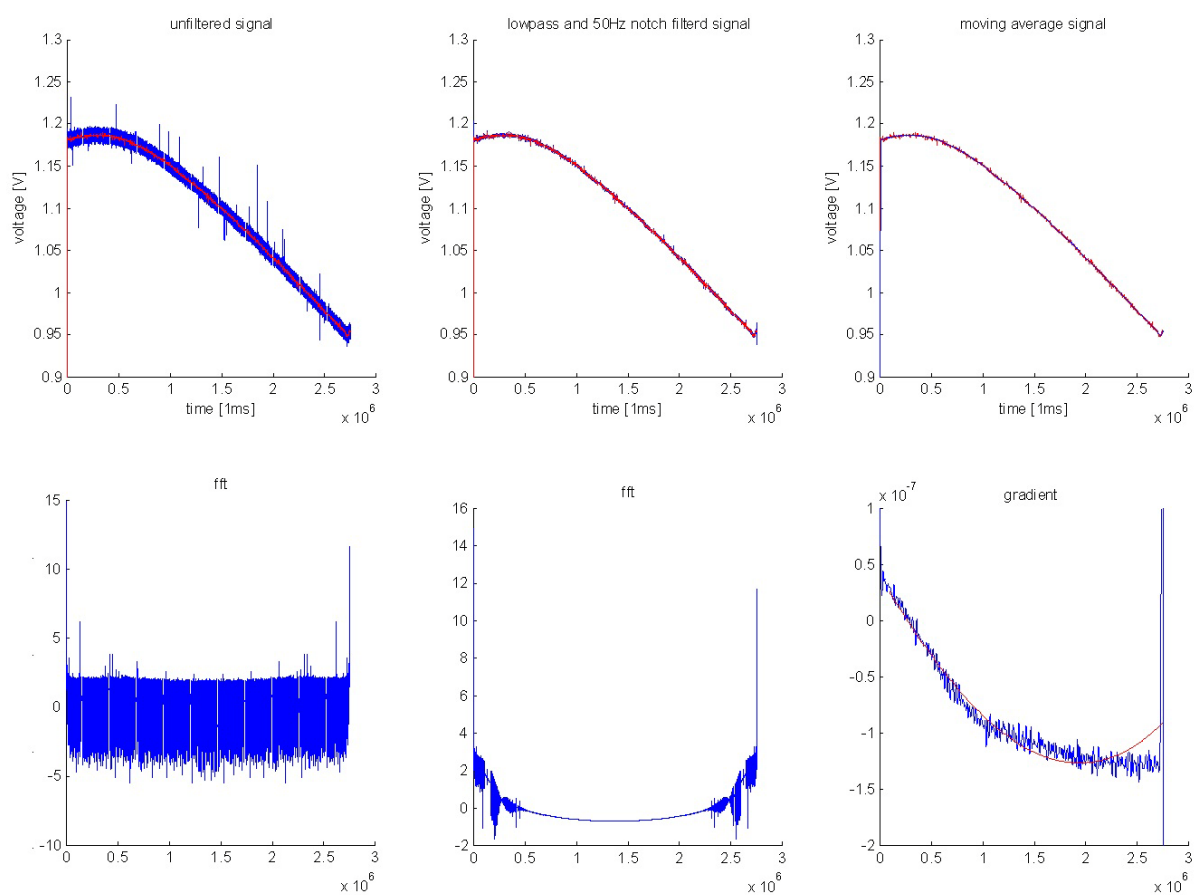


Figure 4-6: Resistor R1_U0.

All graphs of the measured signals are given in Figure 4-6 , while the SEM image of the examined structure is presented in Figure 4-8. It was, as expected, found that the voltage over the resistor which is proportional to the resistance value ($U = I \times R$, with a constant I) decreases. It was at this point not possible to comment about how the resistance in relation to the layers drops, because the first measuring method was used and the parallel resistors with unknown values distorted the curve progression.

In particular, the resistance in the beginning increases as directly seen in the Figure 4-6, but also via the positive deviation at the right upper image. Hereby, it is not very easy to intrinsically explain why the resistance should increase and therefore the eventual convolution due to the electron beam based “charging” effect (which will be mentioned in the next part) should be considered.

This resistor was one of the impotents experiments because it was the first completely *in situ* measured resistor in our lab and shows that this master thesis with the *in situ* measurement works.

4.3.3 Electrical charging (chopper, resistor R1_U2)

In order to examine the charging effect, an experiment similar to the one in the previous part (chapter 4.3.2) was done with the difference that the electron beam was switched ON and OFF for a time delay of one minute which should lead to a charge/discharge effect, if present. For the patterning, the parameters which were given in Table 4-1 were used. Figure 4-8 shows the SEM image of the first resistor mentioned in chapter 4.3.2 and the chopped resistor.

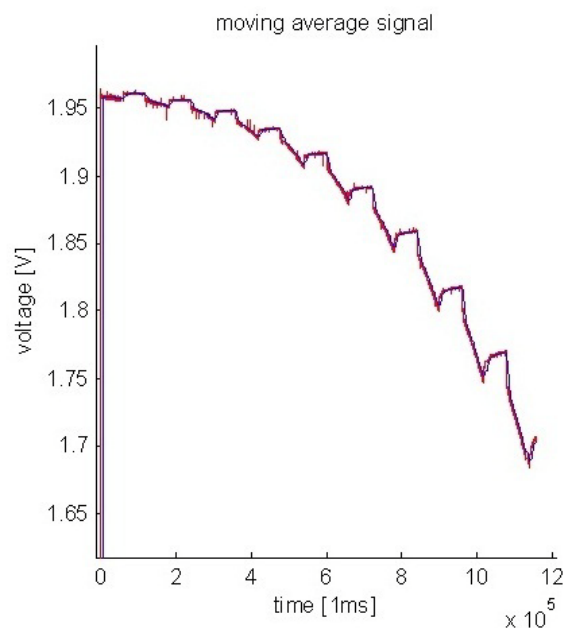


Figure 4-7: Resistor R1_U2 which demonstrate the influence of charging by chopping the electron beam.

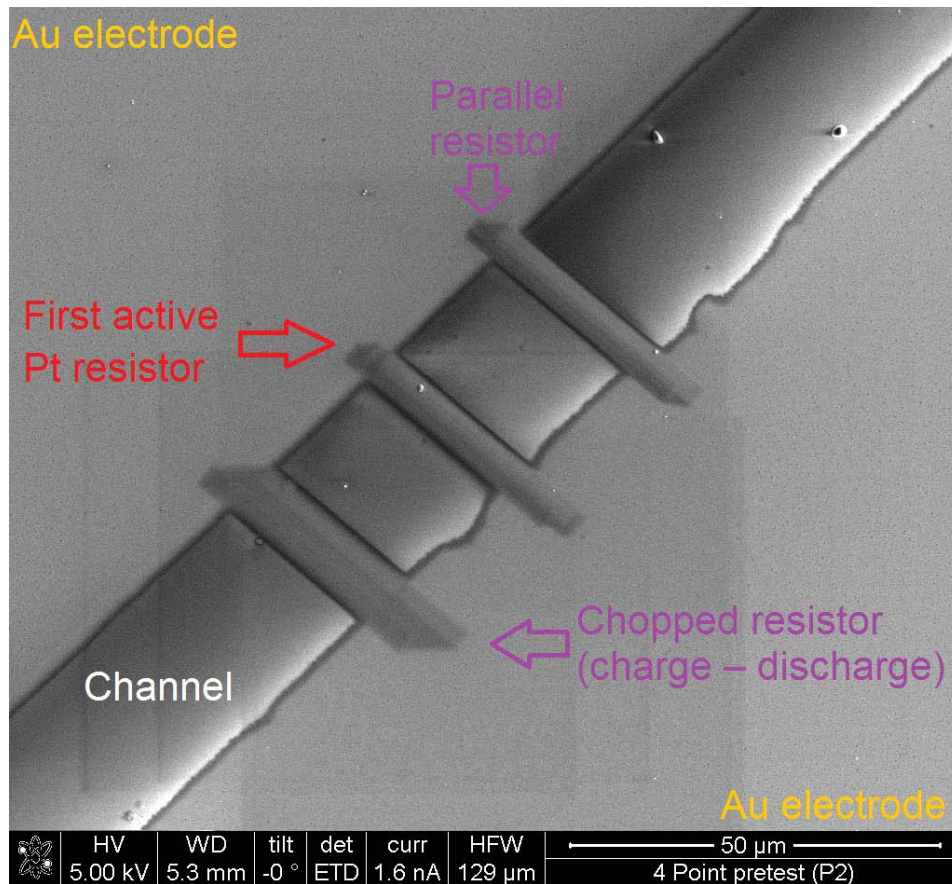


Figure 4-8: The two two-point-measured resistors on specimen “Second prototype” (3.2.3).

In Figure 4-7, the electrical measurements are shown which reveal the formation of the small steps according to the ON / OFF times of the electron beam. The first obvious detail considering the curve in Figure 4-7 is the stronger influence for decreasing resistances which is, however, an artifact since the measurement sensitivity increases because the deposited resistor gets smaller and by this more influences the parallel measurement. This is already described in 4.1. A close look on an electron beam ON–OFF–ON cycle is shown in the left image of Figure 4-9.

The first phase in Figure 4-9 left (zone 1) shows the resistor growth, which seem linear in each part for this short time of one minute. After this, the beam was switched off. The voltage increase first very fast part (Figure 4-9 (left) zone 2) and then slower part (Figure 4-9 (left) zone 3). The fast increase could be explained with the e-beam exposure which adds an additional current to the resistor and when the current is removed a change is observed. The last phase (zone 4) is for when the beam is switched on, where the voltage decreases and falls linear because of the resistor growth.

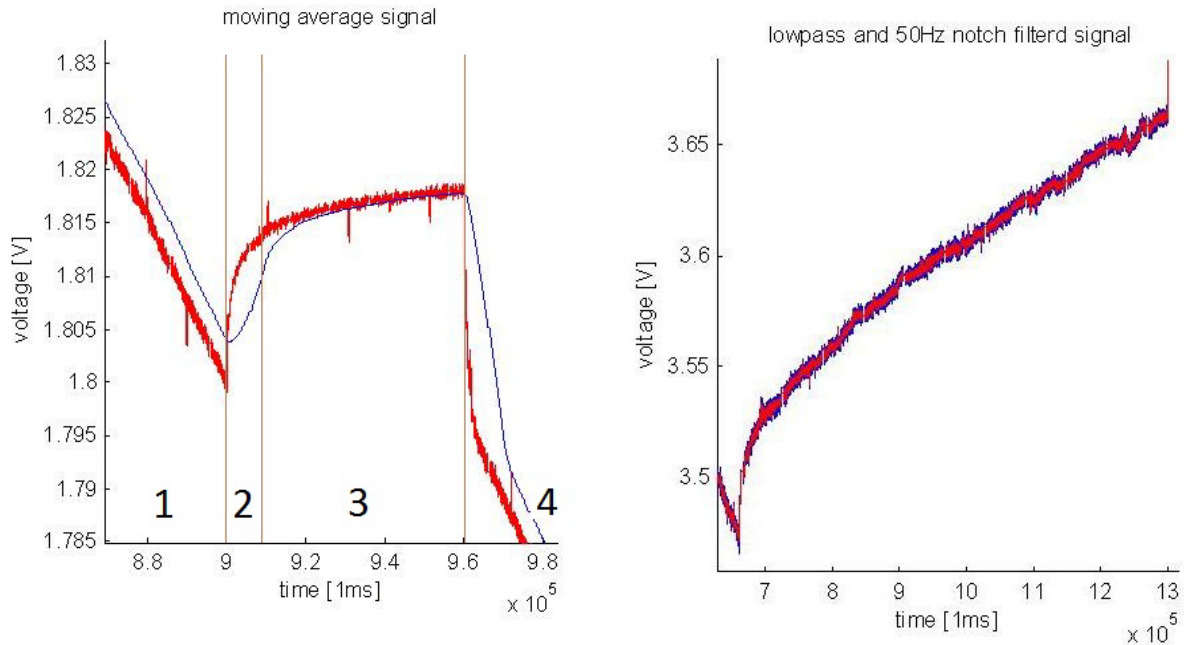


Figure 4-9: On the left side a zoomed step of the chopper experiment is presented. The four phases show four different curve progressions. The first one is the resistor growth, second and thirteen the discharging which could be separate in two parts with a high gradient and one small linear gradient. The last one is the charging and resistor growing. As a comparison, the right image shows a long discharge effect of the resistor P8_R3_R4_U2.

Figure 4-9 (right) shows a discharge of ten minutes. The behavior here is almost the same, and it looks that the slow increase could be linear with an increase of 0.2 mV/min or in percentages only 0.0056%/min. This effect however was not analyzed in this master thesis, but some speculations will be discussed in chapter 4.6

A further analysis was done forming two curves out of this data, one with the voltage level of the end of the first phase and one with the end of the third. The graph and a gradient for this are given in Figure 4-10. The voltage curve shows two staggered curves; red curve for beam-off and blue for beam-on. The curves in the beginning are very close to each other as they get separated for increased time values. This is explained with the high influence of the deposited resistor because the measurement was done in PA (see 4.1). The distance between the curves increases linearly. With the gradient curve it is better observed that they have the same gradient. This leads to the conclusion that the electron beam influence is reversible. That means that the electron beam exposure during the measurement makes the signal weaker, however this will not make a measurement implausible. The resistor growth therefore during deposition is *in situ* measurable and interpretable.

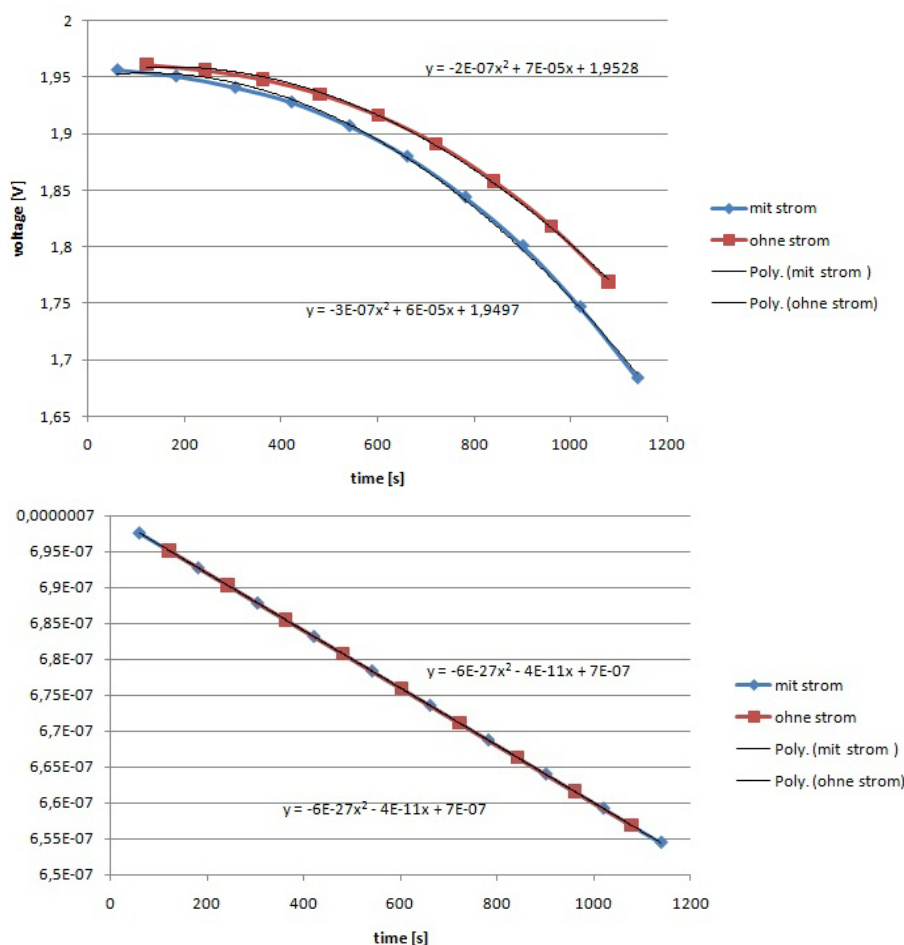


Figure 4-10: The top image shows the voltages with beam on and off. The bottom image is the gradient.

4.3.4 High time resolution

The data from the experiment which was given in 4.3.3 (resistor R1_U2) was also used to check on a high time resolution. For a comparative analysis, two curves with beam on and beam off were used (Figure 4-11).

The two parts of the resistor data show a big difference. As clearly seen in the diagrams, when the beam is off the variation in the signal is small, while this variation increases by the factor of ten when the beam is on. The signal during deposition has a periodic time of 80 to 90 ms. The loop time of this resistor is found to be 85ms, due to its large size. It seems that the noise is not real, but a signal correlated to each single layer of the Pt deposition. Although the resistor R1_U0 was identical, this effect was not observed. For the other measurements this was also not visible because here the loop times were too short. A furthermore investigation was not done in this master thesis because it was out of working range but it will be done in a further work do eventually learn more over the growth of a single layer.

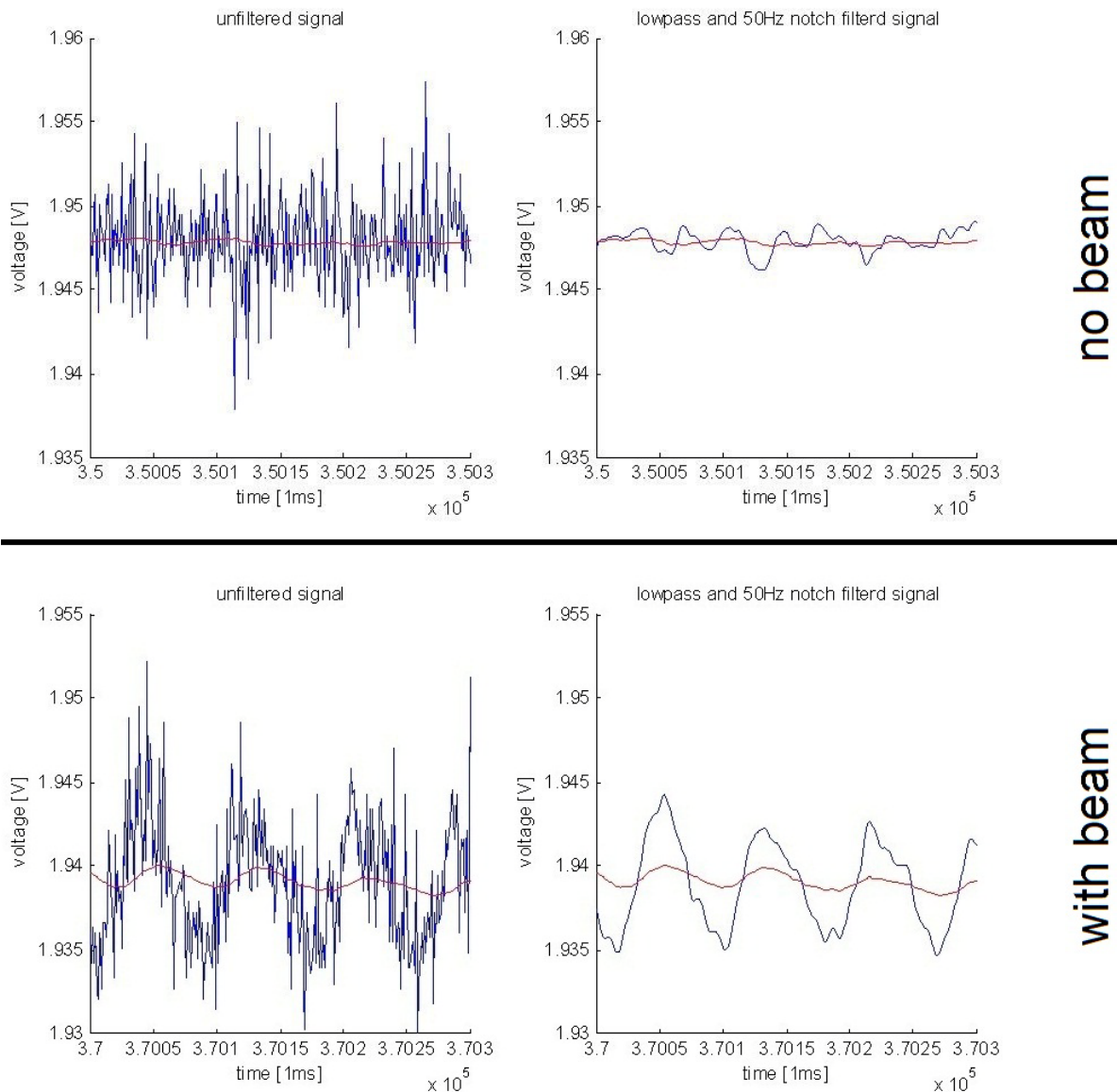


Figure 4-11: The top two diagrams show a 300ms section of the curve for when the beam was not on. The raw signal could be good filtered as the noise is weak. The bottom diagrams have the same time windows, but now the data are measured during depotion (beam on). The noise is stronger (voltage range ist not the same) and it looks diffent to the upper twos.

4.4 First real four point measurement (P8_R3_R3_U1)

With the final specimen (3.2.4) the first real four point measurement was done. The resistor was deposited using the SA method (see 4.1) and according to the parameters shown in Table 4-2. The SEM image in Figure 4-12 shows the resistor and the milling method to disconnect the new from the old resistor. The method with depositing a resistor and after that milling the leads works perfect. A wide cut of 500nm, which needs only a few seconds, was milled using the ion beam parameters of 30 kV and 30 pA. With the online *in situ* measurement the progress could easily controlled. The voltage increased to the maximal measurable value in less than one second and then takes an unsteady value within the measurable voltage range

which indicate that an open circuit was being measured. For being safe that the resistor is completely disconnected, the milling was continued for about three to five seconds and then repeated in about 1-3 μm far away from this region (see Figure 4-12). The electrical measurement data are shown in Figure 4-13.

Table 4-2: Deposition data from the measurement P8_R3_R3_U1.

Name	P8_R3_R2_U1
current	1 μA
pattern length	10 μm
pattern height	3 μm
pattern width	0.5 μm
resistor length	1 μm
resistor height	not measured
loop time	-
total patterning time	~00:03:40
parallel measured	no
sample rate	10000
aq. time	10 s
Amplifier	5x
special	

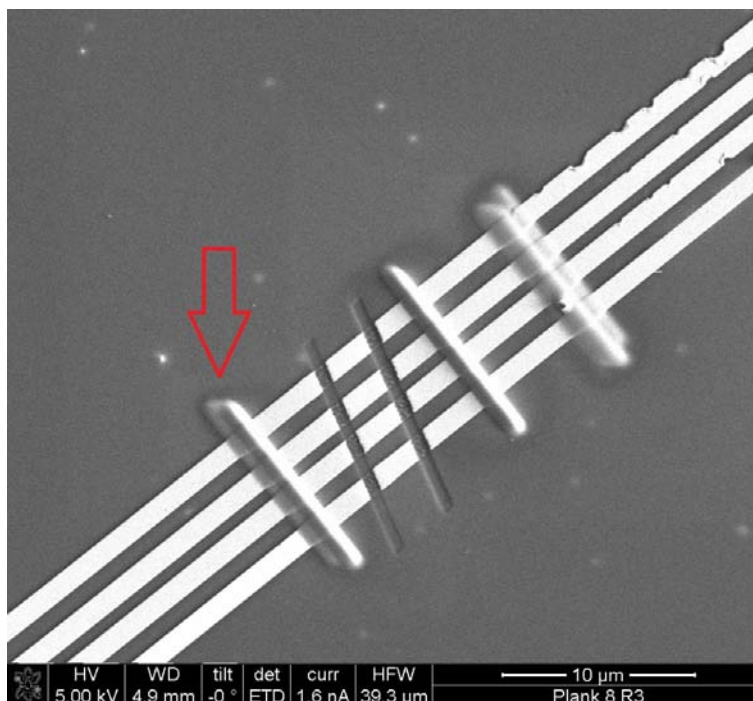


Figure 4-12: The first both resistors (from the right side) were for testing if the measuring in this session works. The first of these two resistors (the right one) was deposited without measuring and the second was measured with the PA method. The two cuts in the middle of the three resistors are milled to disconnect those resistors. This red arrow points out to the resistor P8_R3_R3_U1 which will be discussed in this chapter.

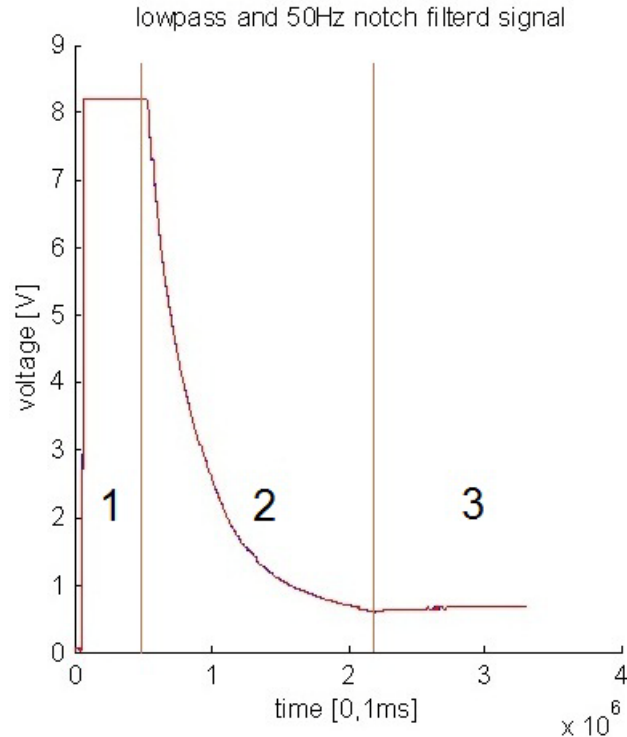


Figure 4-13: Measured data from P8_R3_R3_U1, giving three phases. Phase 1 is with the gas on but the beam off, while phase 2 is the deposition. The last phase is with the beam off and gas off to observe discharging.

The deposition started after about one minute after the gas flow was started (phase 1). After that the deposition was initiated (phase 2) and then after a time of about two minutes, the beam and the gas were switched off (phase 3). During this the measuring continues run.

The diagram (Figure 4-13) shows this curve progress. The maximum measurable voltage is at 8.3 V, which is the first phase and the first part of the second phase. At this time the resistor grows but it is so high that the voltage drop is out of measuring range. The resistor grows in phase two until phase three is reached and this is measurable because the voltage drop over the resistor decreases. In this phase three, when beam and gas are off, a discharging effect, which is described in detail in chapter 4.3.3, is observed.

The resistance was measured with about $7 \cdot 10^2 \Omega\text{m}$. This value is not very precisely because the exact dimensions of the deposited resistor were not identified by the AFM. Therefore this value was only an approximation to gain information about the range of the deposited resistor. The resistance is five orders of magnitude higher than that of platinum and only few better than that of carbon. This is because the deposition of this “EBID max smooth” has a lot of carbon and less platinum (1.2.1 and 1.2.4.)

4.5 Dependence on the current flux during deposition

The electrical current due to *in situ* measurements during deposition could eventually influence the entire deposition process. Especially, measurement method two could strongly influence the first Pt layers due to high current densities and turn out to be a considerable problem as described in chapter 4.1. To reveal such influences a resistor was deposited without *in situ* measurements with the following deposition parameters:

Table 4-3 : Deposition data from the measurement P8_R2_R4_UX.

Name	P8_R2_R4_UX
current	0.2 μ A
pattern length	10 μ m
pattern height	3 μ m
pattern width	0.5 μ m
resistor length	1 μ m
resistor height	not measured
loop time	-
total patterning time	~00:03:40
parallel measured	no
sample rate	10000
aq. time	10 s
Amplifier	5x
special	no current

The resistor value was electrically measured about 30 seconds after the deposition was finished which is sufficient to compensate for the big charging effect. A voltage value of 0.61 V was measured which means a resistance of 610 k Ω as shown in Figure 4-14. The value is in the range of the other resistor during measurement which has a value of 210 k Ω , 850 k Ω and 930 k Ω . So the resistors with and without electrically measurement during deposition has same resistor values.

In these 20 seconds, one can see that the resistor also has the discharge. Here the question arises, if this phenomenon is due to the current change in the resistor or is it a thermodynamic effect so that the value will rise to a specific chemical endpoint. This could be through radicals due to partly dissociated organic fragments which might be trapped inside the resistor. For this, one must make a long time experiment of a few hours, with current in different strengths and without.

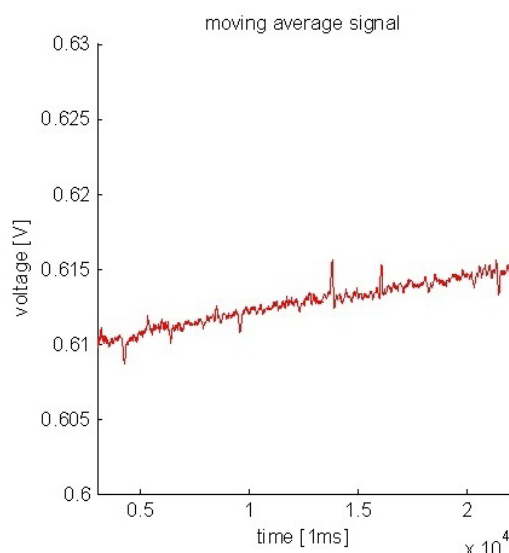


Figure 4-14: The voltage of the resistor P8_R2_R4_U4 about 30 seconds after finishing the deposition.

4.6 Influence of water vapor on the electrical performance

In this experimental study, a resistor was deposited (P8_R2_R1_U1) as described before. Afterwards, water vapor with a partial pressure of $1.58 \cdot 10^{-5}$ mbar was injected to the chamber via the second gas inlet at the TEOS GIS. After about 4 minutes constant exposure the water vapor was switched off. During the entire procedure electrical in situ measurements were running to track the resistance changes directly. A complete sketch of the data is shown in Figure 4-16 by the blue curve, whereas detailed experimental findings are presented in Figure 4-15, Figure 4-17 and Figure 4-18. The deposition parameters were identical to those previously given in Table 4-3.

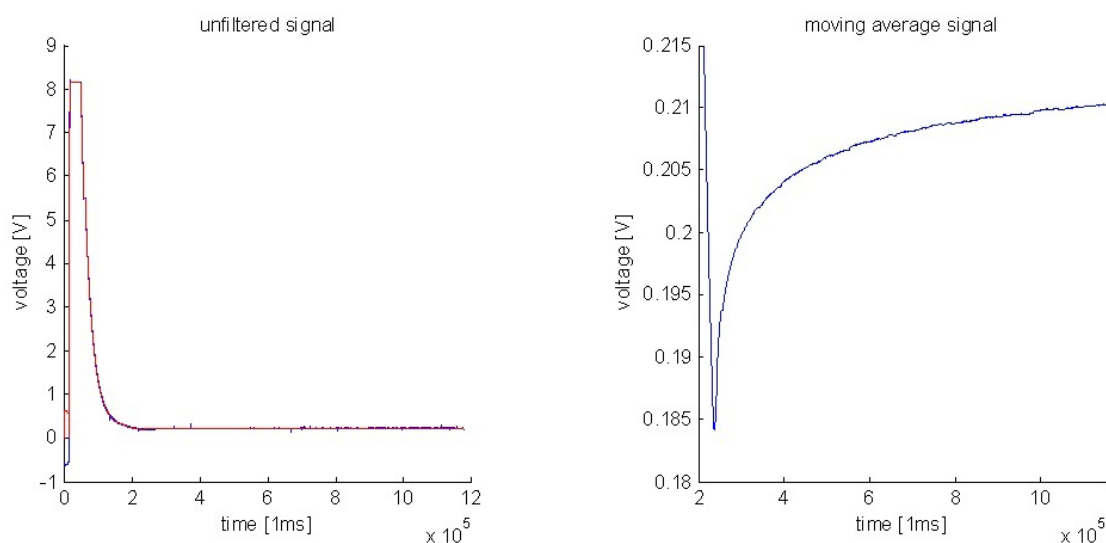


Figure 4-15: Voltage over the resistor P8_R2_R1_U1. It shows the deposition process (left image) and the discharging effect on the right image.

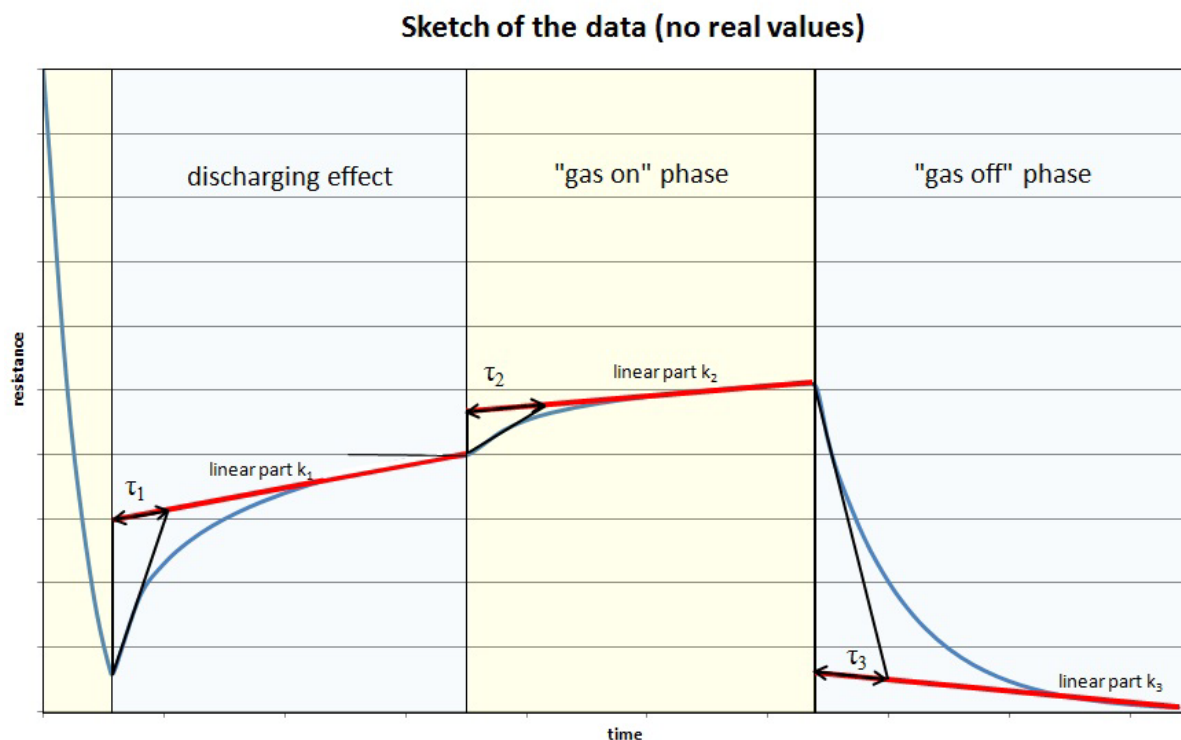


Figure 4-16: Sketch of the treatment which shows basically the curve process and the parameters.

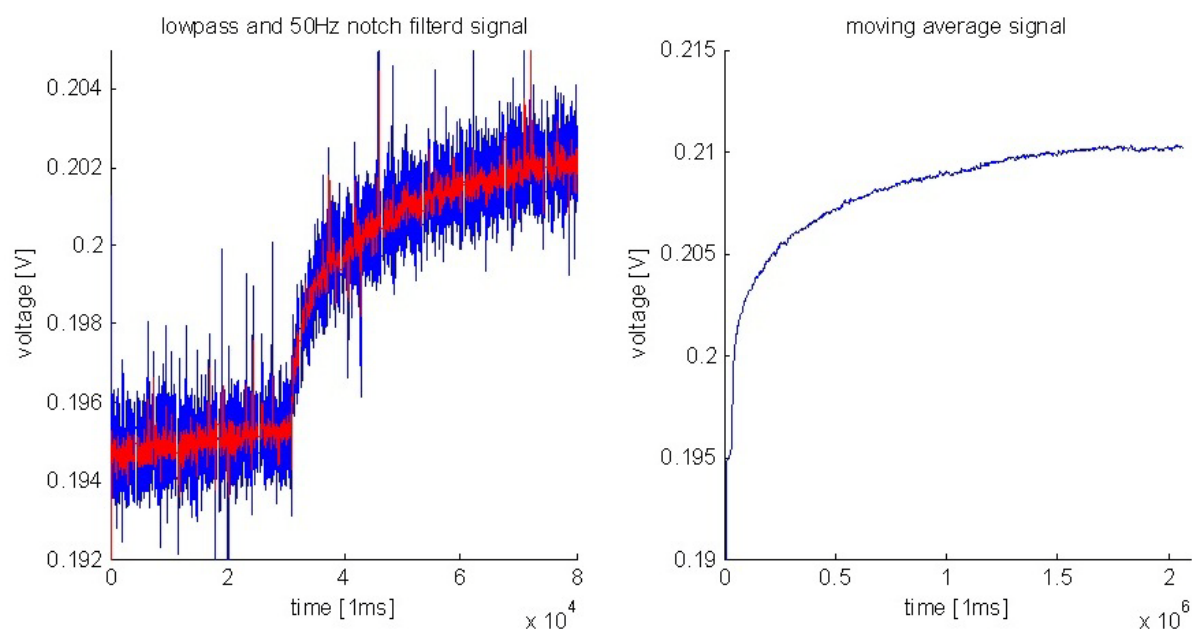


Figure 4-17: The influence of the water vapor. The left image shows the beginning of the "gas on" phase and the sudden increase of the resistance. The right image shows the entire "gas on" phase.

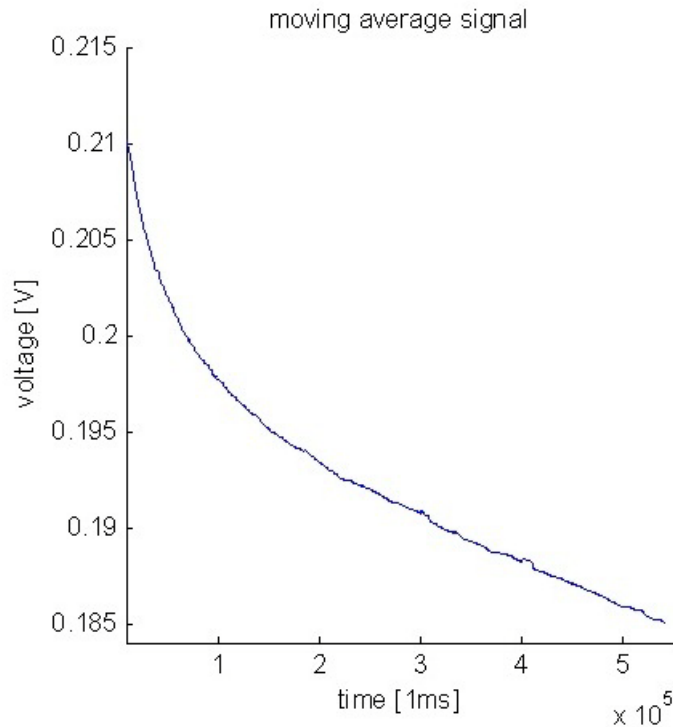


Figure 4-18: The “gas off” phase right after gas exposure. The voltage drop over the resistor decreases to a lower level as water vapor was previously on. The decrease seems to be linear in the end.

The diagrams show that the measured voltage increases during water vapor exposure and decreases again if the water vapor is switched off. The resistance after this water vapor treatment decreases instead of increase how one would conclude of the increase with is described in 4.3.3 which was also observed in Figure 4-14 and Figure 4-15. It is very likely that the water vapor changes the chemistry of the resistor permanently which is reflected by the different tendency before and after curing (increasing / decreasing) as well as by the different starting value for k_1 and k_3 . These results suggest also that the increasing tendency for k_1 is predominantly caused by electrical charging / discharging effects but more likely due to chemical reasons which could be explained by incomplete dissociation during deposition. This has to be investigated in a future study in more detail and will be of high importance.

The parameters which are used for the experiment in Figure 4-16 are shown in Table 4-4. One should notice that the parameters are not exact values but good estimations to reveal the order of magnitude for the different processes. The behavior can be described very well by a combination of exponential and linear functions. A more accurate determination of the values would require much longer acquisition times which will be done in the future. Nevertheless, the given values give a brief insight on time scales and temporal resistivity trends which is essential for an improved understanding of chemical / physical processes during and after deposition.

Table 4-4: Parameter of the curve analysis from P8_R2_R1_U1.

Resistor	P8_R2_R1_U1	
R	185000	[Ω]
τ_1	41	[s]
$k\tau_1$	329	[Ω/s]
$k\tau_1$	0.179	[%/s]
k_1	3.3	[Ω/s]
k_1	0.0016	[%/s]
τ_2	50	[s]
$k\tau_2$	366	[Ω/s]
$k\tau_2$	0.188	[%/s]
k_2	0.55	[Ω/s]
k_2	0.00026	[%/s]
τ_3	60	[s]
$k\tau_3$	-216.67	[Ω/s]
$k\tau_3$	-0.1099	[%/s]
k_3	-24.52	[Ω/s]
k_3	-0.0133	[%/s]

The parameters τ_2 and τ_3 as well as associated gradients k_1 and k_3 show similar orders of magnitude but slight variations. This raises the questions whether the effect could be reversible if the deposits show a stable chemistry before the water vapor exposure. If so, the deposits could eventually be used as sensor devices which could open a new field of application for electron assisted Pt deposition processes.

Further experiments as listed in Table 4-5 and reveal moreover, that higher resistances (flatter deposits) lead to a stronger relative linear increase k_1 (%/s) which might indicate that water molecules penetrate a higher fraction of the deposit, hence, showing a stronger influence on the resistance for flatter deposits. Such a behavior should also be kept in mind since it might allow for further performance tuning via geometrical variations.

Table 4-5: Parameters for the curve analysis from P8_R3_R4_U2.

Resistor	P8_R3_R4_U2	
R	694000	[Ω]
τ_1	15	[s]
$k\tau_1$	666	[Ω/s]
$k\tau_1$	0.095	[%/s]
k_1	43.3	[Ω/s]
k_1	0.00612	[%/s]

Table 4-6: Parameters for the curve analysis from P8_R2_R4_U1.

Resistor	P8_R2_R4_U1	
R	850000	[Ω]
τ_1	20	[s]
$k\tau_1$	3500	[$\Delta\Omega/s$]
$k\tau_1$	0.38	[%/s]
k_1	75	[$\Delta\Omega/s$]
k_1	0.00798	[%/s]

4.7 Resistance variation due to ambient exposure (chamber venting)

To investigate the influence of ambient conditions on the resistance of the Pt deposits the chamber was vented while measuring the electrical resistance. The electrical behavior is given in Figure 4-19 according to the different procedures as listed in the following:

- Phase 1 (not shown in the graph): platinum gas on, electron beam off, covering period to provide high coverage degree of precursor molecules.
- Phase 2: deposition of the resistor with same parameters as shown in Table 4-3.
- Phase 3: five minutes clearance time for discharging effect.
- Phase 4: about five minutes chamber venting with nitrogen while the chamber lock is strongly closed with pressure from outside to prevent an uncontrolled massive ambient exposure.
 - Phase 5: about fifteen minutes ambient exposure at opened chamber lock.
 - Phase 6: about ten minutes for evacuation the chamber and establishing the vacuum again.

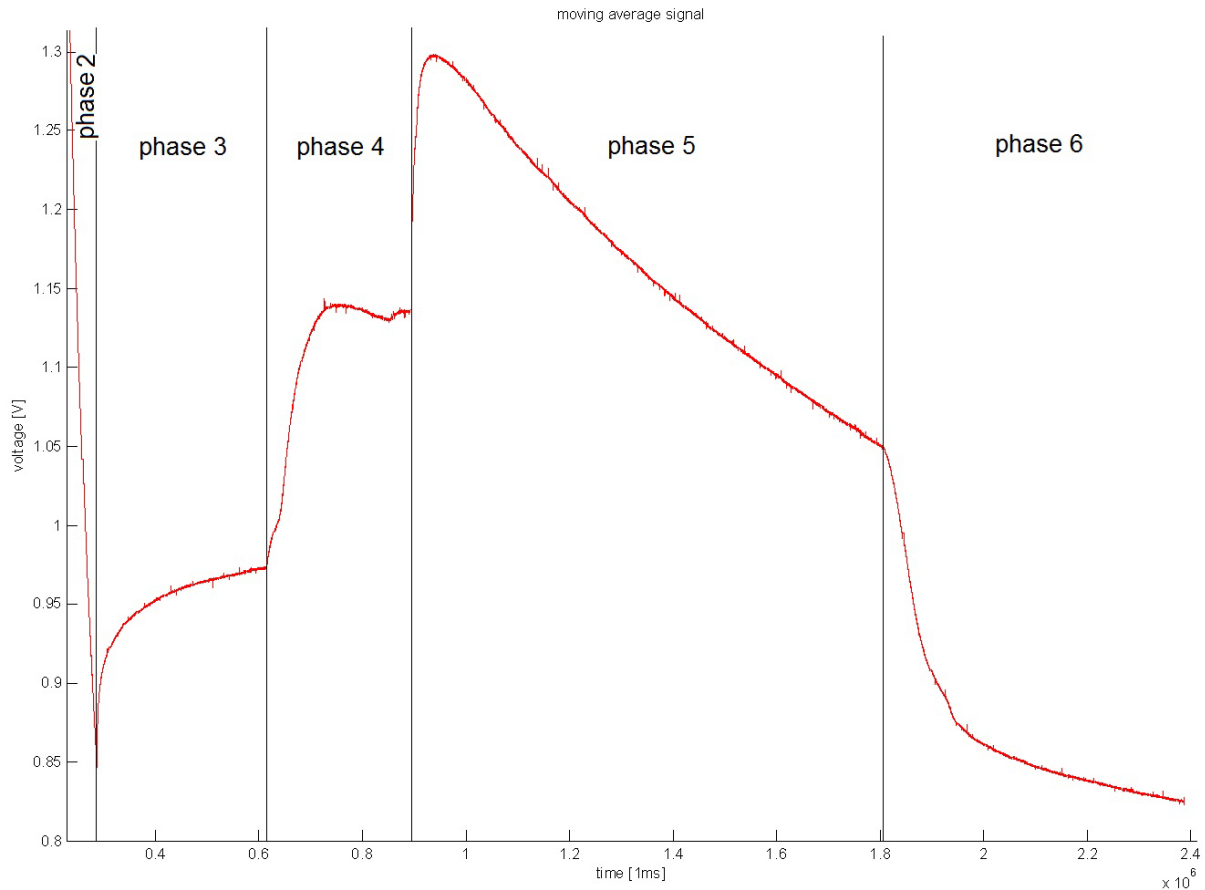


Figure 4-19: Voltage over the resistor P8_R2_R4_U1.

In phase 3, the normal discharge (see 4.3.3) is observed, whose data is previously given in Table 4-7. In phase 4, the resistor increases about 14.9% as the chamber is filled with nitrogen (N_2 exposure). Please note that the venting procedure takes 3 – 4 minutes with a varying chamber pressure which expands τ_4 (about 100 s). Hence, this value is intrinsically lower but convoluted due to technical restrictions. The k_4 value is negative, as the resistance gets smaller after this event. There are two possible reasons for this effect: 1) the presence of nitrogen alters the chemistry; or 2) the pressure is mechanically influencing the resistor. The latter case, however, is kind of contradictory because a higher pressure would mean closer packed Pt crystals which should then increase the conductivity. However, the opposite effect is observed which might indicate that a chemical effect is predominating the resistance variation. Furthermore, there is small increasing feature at the end of phase 4 which is most likely caused by some increase of ambient atmosphere since the chamber cannot be sealed completely.

In phase 5 the chamber lock was completely opened which means an exposure to ambient atmosphere. Please note, at the end of phase 4 the chamber pressure is equivalent to ambient conditions which means that first moments of phase 5 are exclusively driven by the change of

the gas type and not by a pressure variation! Hence, t_5 and k_5 are of real relevance which show again a decreasing character caused by chemical variations due to the main presence of water, nitrogen, oxygen and carbon dioxide.

In phase 6 the chamber was evacuated again, where decreasing resistances are observed as seen before for pure N_2 exposure. The ΔR_6 value is -19% which is less than ΔR_4 and ΔR_4 but ΔR_6 is more than ΔR_5 . In phase 6, the ΔR_6 value was measured from the beginning to the end but one has to notice that the resistor decreases further, so if one takes a longer time the value of ΔR_6 will get higher. Interestingly, the absolute increase (ΔR_{3-4}) of R during N_2 exposure (phase 4) is very similar to the absolute increase (ΔR_{4-5}) of R during ambient gas exposure in phase 5 (+ H_2O , + O_2 , + CO_2) as well as to the absolute decrease (ΔR_{5-6}) during evacuation (phase 6). This suggests several things:

ΔR_{3-4} is driven by the presence of N_2 → most likely due to physical / chemical processes eventually in combination with a higher pressure (general gas presence?)

ΔR_{4-5} is driven by the presence of H_2O , O_2 or CO_2 but definitely NOT due to a higher pressure

ΔR_{5-6} is caused by the complete removal of gases from the chamber / resistor

A closer look reveals that the pure R increase upon water exposure (previous chapter) is about 8 % while the R increase due to the ambient mix is with 13 % slightly higher. This could indicate that the increase ΔR_{4-5} is also influenced by other gases than H_2O . Hence, further and more defined experiments are needed to determine the selective sensitivity of Pt resistors. However, a major problem are the linear increasing / decreasing parts which complicates the measurements and are disturbing a final device.

Table 4-7: Parameters for the curve analysis from P8_R2_R4_U1.

		Resistor	P8_R2_R4_U1	
		R	850000	[Ω]
phase 3	τ_3	20	[s]	
	$k\tau_3$	3500	[Ω/s]	
	$k\tau_3$	0.38	[%/s]	
	k_3	75	[Ω/s]	
	k_3	0.00798	[%/s]	
phase 4	ΔR_4	170000	[Ω]	
	ΔR_4	14.91	[%]	
	τ_4	100	[s]	
	$k\tau_4$	1550	[Ω/s]	
	$k\tau_4$	0.1378	[%/s]	
	k_4	-15.15	[Ω/s]	
	k_4	-0.0013	[%/s]	
phase 5	ΔR_5	150000	[Ω]	
	ΔR_5	11.628	[%]	
	τ_5	10	[s]	
	$k\tau_5$	11000	[Ω/s]	
	$k\tau_5$	0.88	[%/s]	
	k_5	-233	[Ω/s]	
	k_5	-0.022	[%/s]	
phase 6	ΔR_6	-200000	[Ω]	
	ΔR_6	-19.048	[%]	
	τ_6	150	[s]	
	$k\tau_6$	-1066	[Ω/s]	
	$k\tau_6$	-0.1016	[%/s]	
	k_6	-83.33	[Ω/s]	
	k_6	-0.0096	[%/s]	

4.8 Influence of electrical *in situ* characterization on the resistor measurements during gas exposure

As already discussed in 4.5, it is conceivable that the observed effects are influenced or even exclusively dependent on the electrical current due to the *in situ* characterization. To clarify this point, the same experiment as shown in chapter 4.7 were repeated without permanent measurements but only single measurements at significant points. The OFF mode was realized by opening all contacts to the resistor due to switching to the internal reference resistor (see chapter 3.4). An on/off switching with the “on/off”-button would not be possible

because then the ADC would measure an open signal, which gives undefined voltage values. The result of these “point” measurements is given in Figure 4-20 by the red parts.

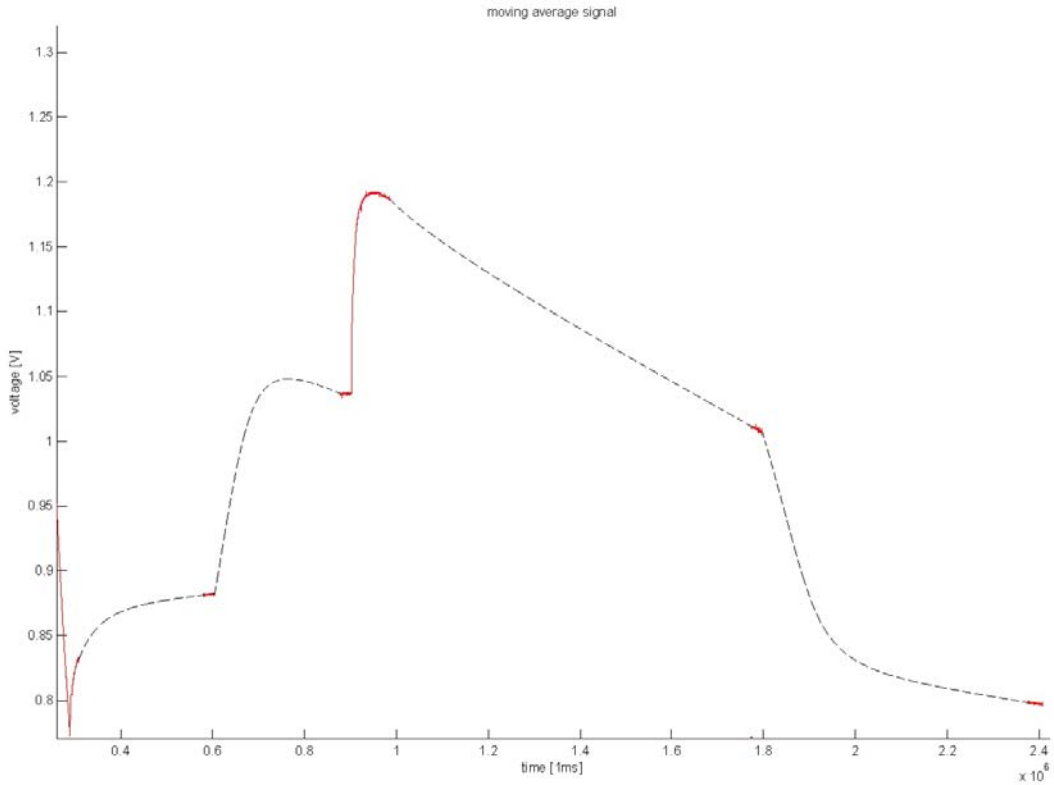


Figure 4-20: Curve process of the data from P8_R2_R4_U2. The red line represents the measured value, while the black line is the fitted curve which links the non-measured data.

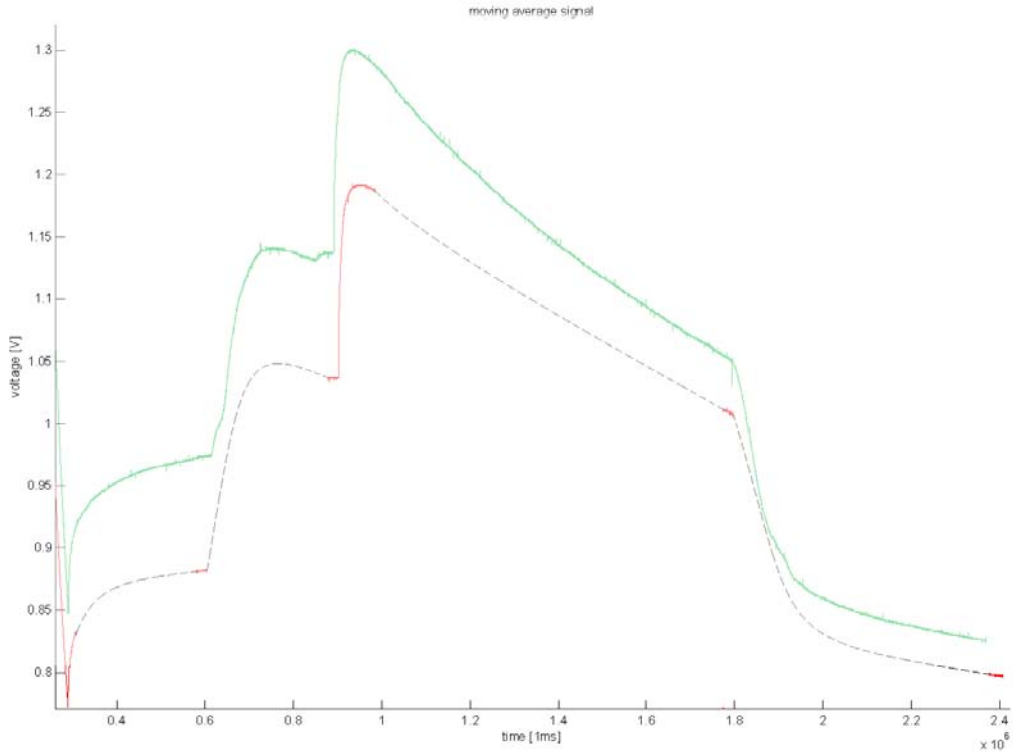


Figure 4-21: Comparison for the vacuum test: with (green line) and without (read/black line) measurement current.

To compare the “point” and “permanent” data to each other the results are displayed together in Figure 4-21, revealing a very similar behavior! Therefore, the influence of electrical *in situ* measurements can be neglected for gas exposure experiments which prove the suitability of the characterization method even in ambient conditions!

4.9 Electrostatic discharge

The four point structure is susceptible to electrostatic discharge (ESD) effects when a conductive resistor is deposited and the device is short-cut from outside; e.g. touching with (electrostatically charged) hands. The sudden potential discharge happens then in a fraction of a second leading to extremely high current densities due to the small dimensions of the gold structures finally melting down the paths. Such a destroyed four point structure is shown in Figure 4-22. Therefore, it is extremely important that the device is completely opened via the ion beam before it is removed from the active stage holder for a safe handling. To reduce ESD shock risks even further, special ESD gloves are highly advised to be used.

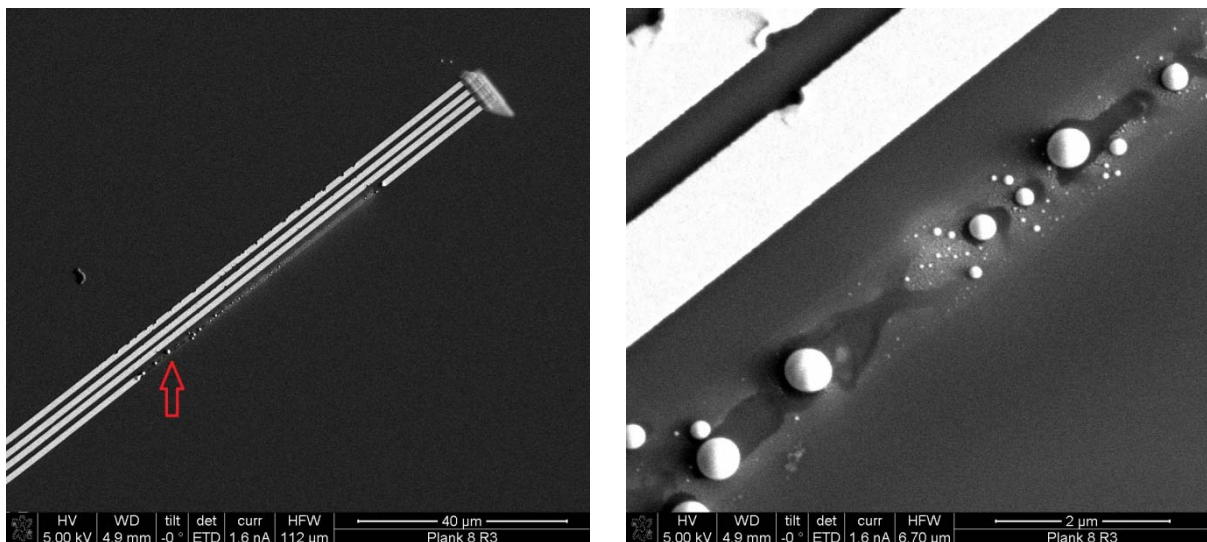


Figure 4-22: The effect of electrostatic discharge. The left image shows one lead which is melted. The right image is a close-up where small gold spheres are viewed.

5 Summary

The scope of this thesis was the design, fabrication and feasibility testing of an active sample holder for a SEM / FIB dual beam microscope, enabling electrical *in situ* measurements of electron beam induced Pt deposition from the gas phase.

As a first task, an appropriate hardware was designed and fabricated. The setup consisted of a sample holder (see chapter 3.5) and the electric circuit (see chapter 3.4) including a constant current source (see chapter 3.3). The sample holder which allowed for further analysis was such designed to be compatible to the available AFM and to the homemade FIB cryo-stage, available at the Institute for Electron Microscopy (FELMI). The active sample stage as well as constant current source and measurement circuit was found to meet all requirements and allowed for *in situ* data acquisition (see chapter 3.7) realized via the software LabVIEW for accessing / controlling the analog digital converter PC card while measuring an amplified signal of the voltage drop across conductive Pt deposits during or after deposition. The measured signals which are further processed and visualized by MATLAB allowing for quantitative analyses in a temporally resolved manner.

The investigation with the in house-developed EBID max smooth patterning (see chapter 1.2.4) revealed that the related growth rate is widely independent on geometric footprints and, more important, on refresh times which suggest strongly a reaction rate limited precursor regime during deposition in which an excess of precursor molecules is available with respect to the number of potentially dissociating electrons. Secondly, it is found that the relative position of the patterning areas with respect to the gas nozzle cannot be completely neglected. However, it has to be remarked that the latter is a general rule and independent of the patterning parameters (see chapter 2).

After feasibility testing of hard- and software in the dual beam environment; first resistors have successfully been deposited and characterized with *in situ* character. In the following the main achievements are briefly described and referenced to the individual chapters for a more detailed look.

First, it is found that the current due to the measurement equipment, usually between 0.2 and 1 μA , seemed to have no influence (see chapter 4.5 and 4.8) on the performance of the Pt deposit. This was, for comparison, tested by detecting the resistance value of a resistor with and without applying measurement current during deposition.

The chopper experiment (see chapter 4.3.3) revealed that *in situ* measurements are possible in principle. However, the measured voltage has always a negative offset due to the contribution of the electron beam through the structure. Hence, absolute measurements must be corrected by the relative influence which can be done by a simple chopper experiment. The influence of electron beam could also be observed throughout a high time resolution measurement where the single layers of the deposited platinum could be observed (see chapter 4.3.4). However, it was clearly shown that the relative resistance variation is completely independent on the electron beam which allows therefore a fast and very accurate temporal investigation of Pt deposits.

As a first new result, it was found that Pt deposits can reveal sensor characteristics upon gas exposure. For example, water vapor (see chapter 4.6) induced increasing resistances with a generally reversible character after the gas flux was turned off again. A closer look to the resistance behavior before (slightly increasing) and after H₂O exposure (slightly decreasing as described in chapter 4.3.3), it can be concluded that the Pt deposit does not consist of a 100% stable chemistry. After the first exposure to water vapor the characteristics change slightly while the overall sensing characteristics are very similar and still reversible. Further experiments in which the deposit was exposed to a nitrogen atmosphere with ambient pressure (see chapter 4.7) revealed an resistance increase of about 15 % in a few seconds. Subsequent exposure to ambient air without further pressure variations revealed further increase of resistances of about 11% followed by slightly decreasing tendencies. By these experiments an exclusive influence by the environmental pressure can be excluded proving the gas type sensing capabilities of electron beam induced Pt deposits. Furthermore, the oxidation of the Pt crystals upon ambient air exposure can also be excluded due to the reversible character. This leads to the result that the Pt deposition could be used as a sensor, regarding to its promising non-optimized characteristics in response time (ranging from 10 to 60 seconds), sensitivity (> 10%) and reversibility.

Finally, it can be suggested that the use of platinum deposition could open a new way for novel sensor applications owing to their advantageous properties such as being low cost and can be designed and fabricated on small scales without any masks.

6 Outlook

As described before this master thesis enables new ways for manifold investigations with real *in situ* character to gain more fundamental knowledge but also in a manner for optimization. By using different exposure gases like oxygen, carbondioxide, nitrogen, sulfur, helium or argon, selectivity and sensitivity on resistances can be accessed in defined environmental conditions. Fundamental chemical changes can also be indirectly observed which should improve the fundamental understanding of such deposits. Furthermore, the dependency on gas pressure can also be tested which allows for further testing towards a selective leaking gas sensor application.

Further attention should be put on deposit geometries since flatter structures should provide higher responses due to a higher fraction of gas penetrated cross sections. Different layouts (e.g. interdigital structures) could further expand the sensitivity with the aim of rapid sensing capabilities with improved reversibility characteristics. Finally, the structures can also be exposed in liquid environments to test their suitability of fluid, ion, or specific component sensing.

A further important effect, first observed during this master thesis, concerns the e-beam curing processes which improve the conductivity considerably for special deposition conditions.

All experimental work carried out in the outline of this thesis is to be examined in the future by TEM. This could lead to possible invention of novel devices, such as very small sensors with high resistivity alteration and better deposition quality. Also, other precursor gases, such as gold, tungsten or aluminum could bring out more useful information and applications.

7 References

- [1] Akhmadaliev C., Bischoff L., Mair G.L.R., Aidinis C.J., Ganetsos Th., 2004. Investigation of emission instabilities of liquid metal ion sources, *Microelectronic Engineering*, 73–74, 120–125
- [2] Botman A., Mulders J J L, Hagen C W, 2009. Creating pure nanostructures from electron-beam-induced deposition using purification techniques: a technology perspective, *Nanotechnology* 20, 372001 (17pp)
- [3] Drouin D., Coutre A. R., et. al., 2007. CASINO V2.42—A Fast and Easy-to-use Modeling Tool for Scanning Electron Microscopy and Microanalysis Users, *SCANNING VOL. 29*, 92–101
- [4] Eugenio U. Donev, Hastings J., 2009. Electron-Beam-Induced Deposition of Platinum from a Liquid Precursor, *Nano Letters*, Vol. 9, No.7 2715-2718
- [5] Gazzadi G. C., Frabboni S., 2009. Structural evolution and graphitization of metallorganic-Pt suspended nanowires under high-current-density electrical test, *APPLIED PHYSICS LETTERS* 94, 173112
- [6] Giannuzzi, L.A.; Stevie, F.A.; “Introduction to Focused Ion Beams”, Springer, 2004
- [7] Goldstein J. I., Newbury D.E., et. al., 1992. *Scanning Electron Microscopy and X-Ray Microanalysis*, Plenum Press, New York, London
- [8] Goldstein J.I., Newbury D.E., Echlin P., Joy D.C., Romig A.D., Lyman C.E., Fiori C., Lifshin E., 2003. *Scanning Electron Microscopy and X-ray Analysis*. Third Edition, Plenum Press, New York, London
- [9] Grogger W., 2004. *Rasterelektronenmikroskopie*, teaching script
- [10] Keithley J. E., *Low Level Measurements*, Keithley Instruments, Inc, 5th Edition
- [11] Plank H., et.al., 2008. *Nanotechnology*, 19, 485302
- [12] Internal communication, presentation, and lectures
- [13] L. Reimer, 1998. *Scanning Electron Microscopy, Physics of Image Formation and Microanalysis*, Volume 45, Springer Verlag, Berlin Heidelberg

-
- [14] Rattenberger J. PhD Thesis, Institute for Electron Microscopy, Graz University of Technology, 2011
- [15] Silvis-Cividjian N., Hagen C. W., 2006. Electron-Beam-Induced Nanometer-Scale Deposition Advances, Imaging and Electron Physics vol. 143, Elsevier Academic, San Diego
- [16] Sezen M., 2009. Nanostructuring and Modification of Conjugated Polymer Based Optoelectronic Device Structures by Focused Ion Beam
- [17] Uchic M.D., Holzer L., Inkson B.J., Principe E.L., Munroe P., 2007. Three-dimensional microstructural characterization using Focused Ion Beam tomography, MRS Bulletin, Vol. 32, 408-416
- [18] Utke I., Hoffman P., Meingattis J., Jul/Aug 2008. Gas-assisted focused electron beam and ion beam processing and fabrication, J. Vac. Sci. Technol. B 264
- [19] Utke I. et al., 2006. Microelectron, Eng. 83, 1499,
- [20] Volkert C.A., Minor A.M., 2007. Focused Ion Beam microscopy and micromachining, MRS Bulletin, 2007, Vol. 32, 389-395
- [21] Mayer J., Giannuzzi L. A., Kamino T., Michael J., 2007. TEM Sample Preparation and FIB-Induced Damage, MRS Bulletin, 2007, Vol. 32, 400- 407
- [22] Fei Company, 2007. Platinum deposition technical
- [23] http://www.sigmaaldrich.com/thumb/structureimages/49/a_____514349.gif (19.7.2010)
- [24] <http://www.strem.com/catalog/v/78-1350/53/> (19.7.2010)
- [25] <http://www.burr-brown.com>
- [26] <http://www.st.com>
- [27] <http://www.ni.com/>
- [28] Inhouse modified RAITH ebeam lithography at the Institute of Physics, University of Graz